SKB TECHNICAL REPORT

97-24

Characterization of the excavation disturbance caused by boring of the experimental full scale deposition holes in the Research Tunnel at Olkiluoto

Jorma Autio

Saanio & Riekkola Oy, Helsinki, Finland

September 1997

CHARACTERIZATION OF THE EXCAVATION DISTURBANCE CAUSED BY BORING OF THE EXPERIMENTAL FULL SCALE DEPOSITION HOLES IN THE RESEARCH TUNNEL AT OLKILUOTO

Jorma Autio

Saanio & Riekkola Oy, Helsinki, Finland

September 1997

CHARACTERIZATION OF THE EXCAVATION DISTURBANCE CAUSED BY BORING OF THE EXPERIMENTAL FULL SCALE DEPOSITION HOLES IN THE RESEARCH TUNNEL AT OLKILUOTO

Jorma Autio

Saanio & Riekkola Oy
Laulukuja 4
00420 Helsinki
Finland

PREFACE

ABSTRACT

Three holes the size of deposition holes were bored in the Research Tunnel using a novel full-face boring technique. During the boring test procedures were carried out in order to determine the effect of changes in operating parameters on the performance of the boring machine and the quality of the hole. Evaluation of the quality of the hole included studies of the geometry of the holes, measurements of surface roughness using a laser profilometer, rock mechanical determinations and study of excavation disturbances in the zone adjacent to the surface of the holes using two novel methods, the He-gas method and the ^{14}C-polymethylmethacrylate (^{14}C-PMMA) method. It was found that there is a distinct disturbed zone adjacent to the surface of the full scale deposition holes which can be divided into three different zones. The zones are as follows: a crushed zone penetrating to a depth of about 3 mm from the surface, a fractured zone extending to a depth of 6 - 10 mm from the crushed zone and a microfractured zone extending to a depth of 15 - 31 mm from the fractured zone. The porosity of the rock in the disturbed zone measured using the ^{14}C-PMMA method was clearly greater than the porosity of undisturbed rock to a depth of about 11 mm. The values of permeability and effective diffusion coefficient in the disturbed zone measured in a direction perpendicular to the disturbed surface were found to be approximately one order of magnitude larger than those of undisturbed rock. The degree of disturbance was found to be greater where higher levels of thrust had been employed during the boring process. The results obtained also suggest that the disturbance caused by using 4- and 5-row cutters in the cutter head is more pronounced than the disturbance caused when using 5- and 6-row cutters.

SAMMANFATTNING

Tre hål med ungefär samma storlek som fullstora deponeringshål har borrats i Forskningstunneln i Olkiluoto med en ny fullborrningsteknik. Under borrningen genomfördes tester i syfte att bestämma vilken betydelse förändringar i borrmaskinens driftparametrarna har på hålets kvalitet. Utvärdering av hålens kvalitet inkluderade studie av hålens geometri, mätning av bergväggens ytråhet, bergmekaniska bestämningar och studie av borrinducerade förändringar i zonen närmast borrhålets bergvägg med två nya metoder - Heliumgas metoden och kol-14-polymetylmetakrylatmetoden (^{14}C-PMMA). Resultatet visar att det finns ett tydligt, stört område närmast hålets vägg, som kan delas upp i tre olika zoner; en krosszon som sträcker sig ungefär 3 mm in i bergväggen, en uppspräckt zon som sträcker sig ytterligare 6-10 mm in i bergväggen samt en zon med fina sprickor som når ytterligare 15-35 mm in i berget. Porositeten i den störda zonen, som mättes med ^{14}C-PMMA metoden, är större än porositeten i det ostörda berget intill ett djup av 11 mm. Permeabilitet och effektiv diffusionskoefficient i den störda zonen vinkelrätt mot den störda ytans plan uppmättes till omkring tio gånger större värden än i ostört berg. Graden av störning befanns vara större där ett högt matningstryck hade använts under borrningen. Resultaten indikerar också att störningen som orsakats av kuttrar med 4 och 5 rader är mer tydlig, än den som orsakats av kuttrar med 5 och 6 rader.

TABLE OF CONTENTS

1 INTRODUCTION

According to the preliminary design for the final repository for spent fuel made by Swedish Nuclear Fuel and Waste Management Co (SKB) and Posiva Oy the repository is to be excavated at sufficient depth in the crystalline bedrock and the encapsulated spent fuel emplaced in holes in the tunnel floor, see Figure 1-1. In the design proposed by SKB the total number of deposition holes is 4500 and the depth of the final repository for spent fuel ranges from 400 to 700 m. In the corresponding design proposed by Posiva Oy the depth of the repository is from 300 to 700 m and the total number of deposition holes is 1530.
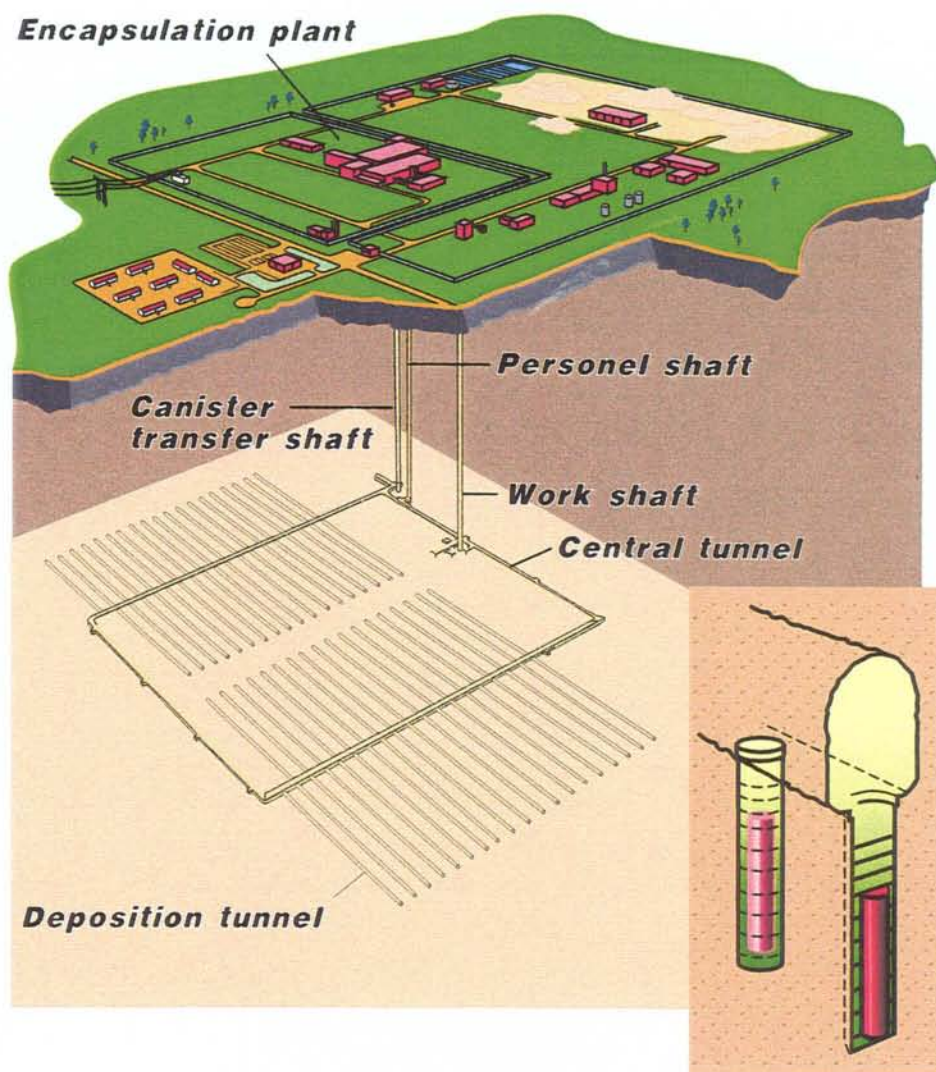
Figure 1-1. Basic concept of the final repository for spent fuel. The spent fuel canisters will be emplaced in deposition holes in the tunnel floor (TVO 1992).

The excavation of deposition holes is a topic that features in the development of repository technology for two main reasons: the quality of the excavated hole has an impact on the long-term safety of the disposal, and the excavation of a large number of holes in small tunnels at considerable depths is a challenging technical task.

Three experimental full-scale deposition holes were bored in the Research Tunnel at Olkiluoto to demonstrate the feasibility of the full-face boring with vacuum suction technique with particular regard to the quality of the excavated hole and the performance of the boring equipment. The exact diameter of the experimental holes was a function of the size of the available cutter head, this being 1524 mm. The depth of the excavated holes was 7.5 m.

The Research Tunnel is located at a depth of 60 m in the VLJ-repository which is an underground disposal facility for the low- and medium-level waste generated by the Olkiluoto nuclear power plant, see Figure 1-2. The repository is located 1 km from the Olkiluoto 1 and Olkiluoto 2 power plants on Olkiluoto island on the southwest coast of Finland. The repository began operating in 1992. The Research Tunnel is 47 m long and from 4 to 7 m high. It was excavated using conventional drill and blast techniques. A charge density of approximately 1.1 kg-dyn/m (weight of charge per unit length of the stem section of the hole, equivalent to the charge density of dynamite) was used when blasting the floor section. The corresponding spacing between the perimeter holes was about 0.86 m.

Boring of the experimental full-scale deposition holes was accompanied by comprehensive pre-boring and post-boring characterization of the rock in areas close to the holes using a range of geophysical, geological, hydraulic and mechanical tests.

One of the main objectives when boring the experimental full-scale deposition holes was to generate empirical data relating to the excavation disturbance caused by boring and the factors affecting this disturbance. Evaluation of the quality of the hole included studies of the hole geometry, surface roughness and excavation disturbance in the zone adjacent to the surface of the holes. The quality of the hole was a subject of interest because in spite of the fact that it may have an impact on the design of the disposal facility and the extent of this impact has not been specified, existing information on the subject is very limited.

The excavation disturbance caused by boring is influenced by machine-related factors such as the shape of the cutters and levels of thrust used, and rock-related factors such as uniaxial compressive strength and drillability index. Current estimates of the extent of the disturbed zone are in the main based on laboratory-based indentation experiments with single cutters. A recent review of the studies related to this subject and the latest achievements are reported by Tan et al. 1994, Lindqvist et al. 1994, Shao-Quan et al. 1994.
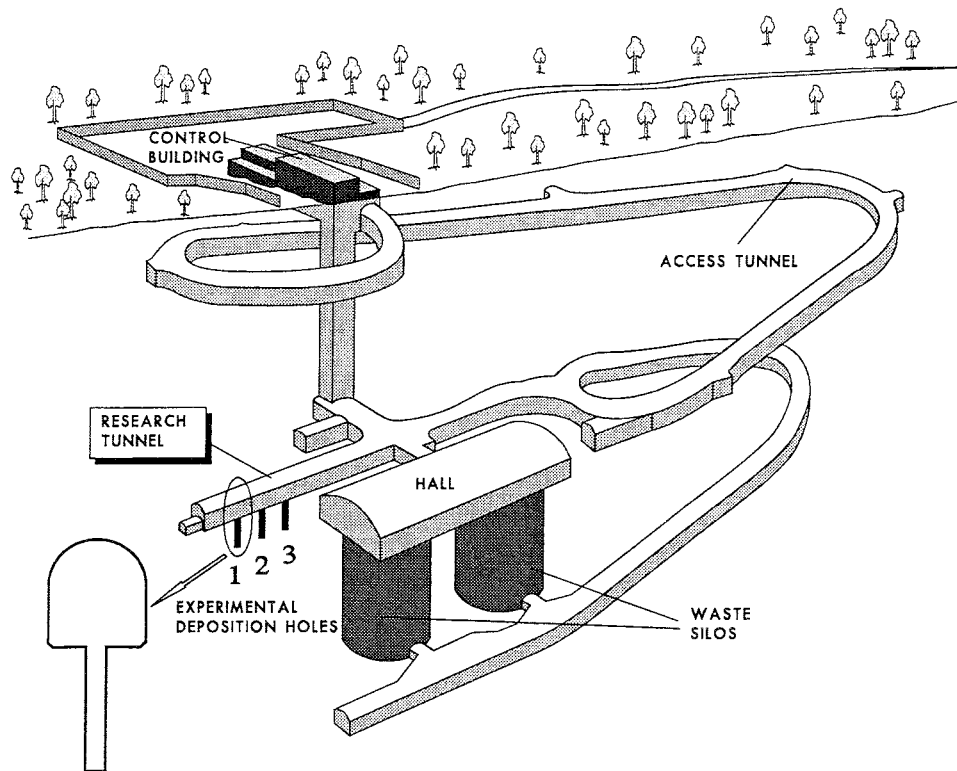
Figure 1-2. VLJ-repository and the Research Tunnel.

During boring, tests were carried out to determine how changes in the operating parameters of the boring equipment affected the quality of the hole. The main focus of interest when assessing the quality of the excavated holes was surface roughness and mechanical disturbance, the latter being specified as the increase in microfracturing and porosity in a zone adjacent to the hole surface.

The safety of the final disposal of spent fuel is based on a multi-barrier system, see Figure 1-3. One of the barriers is the bedrock, the part closest to the canister of spent fuel being the wall of the deposition hole. One function of the bedrock surrounding the deposition holes is to retard and/or prevent the migration of radionuclides. Large diameter holes bored using the full-face technique employed during the boring experiments results in a zone of increased microfracturing and porosity in the walls of the holes known as the 'excavation-disturbed' zone. The physical properties of this zone, for example the diffusion and permeability, have an influence on the migration of radionuclides. Another function of the surface zone of the walls of the disposal holes is to support the performance of the near by bentonite sealing of the holes. Deflections of the excavated holes and any surface unevenness affect the width of the gap between the bentonite seal and the rock during the emplacement of the canister and bentonite. The properties of the rock and the excavation-disturbed zone also have an influence on the conduction of water around the bentonite seal and therefore affect the process by which the bentonite becomes saturated.
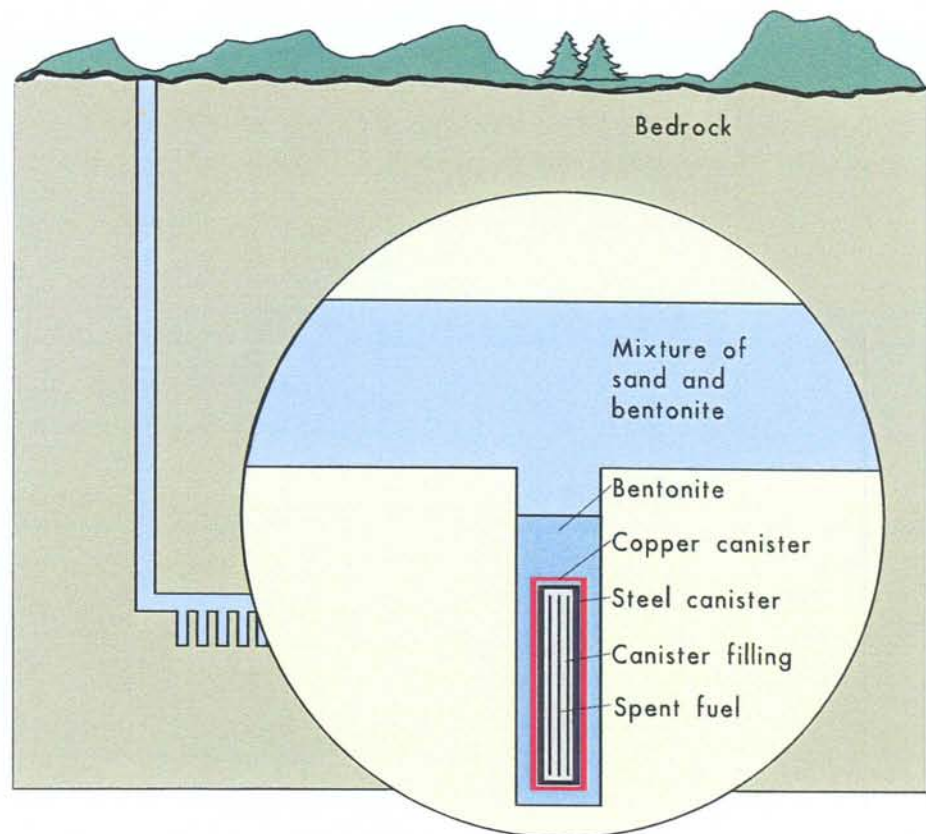
Figure 1.3. *General principle of the final disposal of spent fuel (TVO 1992).*

Characterization of the physical properties of the holes included detailed geological mapping of the surfaces, photography of the walls, measurement of the hole geometry, measurement of surface roughness and laboratory studies of the properties of the rock in the excavation-disturbed zone.

The geometry and physical properties of the rock in the disturbed zone was studied by using two novel methods, the ^{14}C-PMMA method and the He-gas method. The ^{14}C-PMMA method was used to determine the total porosity and spatial distribution of porosity in both the disturbed and undisturbed zones. The He-gas method was used to determine the diffusion coefficient and permeability of the rock in the disturbed zone as well as to evaluate the actual thickness of the zone.

2   THE BORING TECHNIQUE

2.1   GENERAL

Boring was based on the rotary crushing of rock, removal of the crushed rock taking place by vacuum flushing through the drill string. In principle, the process of crushing the rock is the same as that used in conventional raiseboring. The main difference between the methods is the technique used to remove crushed rock from the bottom of the hole, see Figure 2.1-1. Vacuum cleaning was employed for this purpose.

The boring equipment comprised a raiseboring machine, frame, drillstring, cutter head and vacuum suction system, see Figures 2.1-2 and 2.1-4.

A separate pilot hole was bored before boring of the large hole began. The pilot bit used for the boring of the pilot hole was then used in front of the large diameter cutter head as a guide and stabilizer.

After crushing, the rock waste was sucked through the cutter head and drillstring to the suction line which consisted of the flow channels in the boring machine, external transport pipes, a tank for crushed rock and a vacuum unit (see Figure 2.1-3).

| 1. Boring | 2. Stop | 3. Extension of drillpipe | 4. Start |
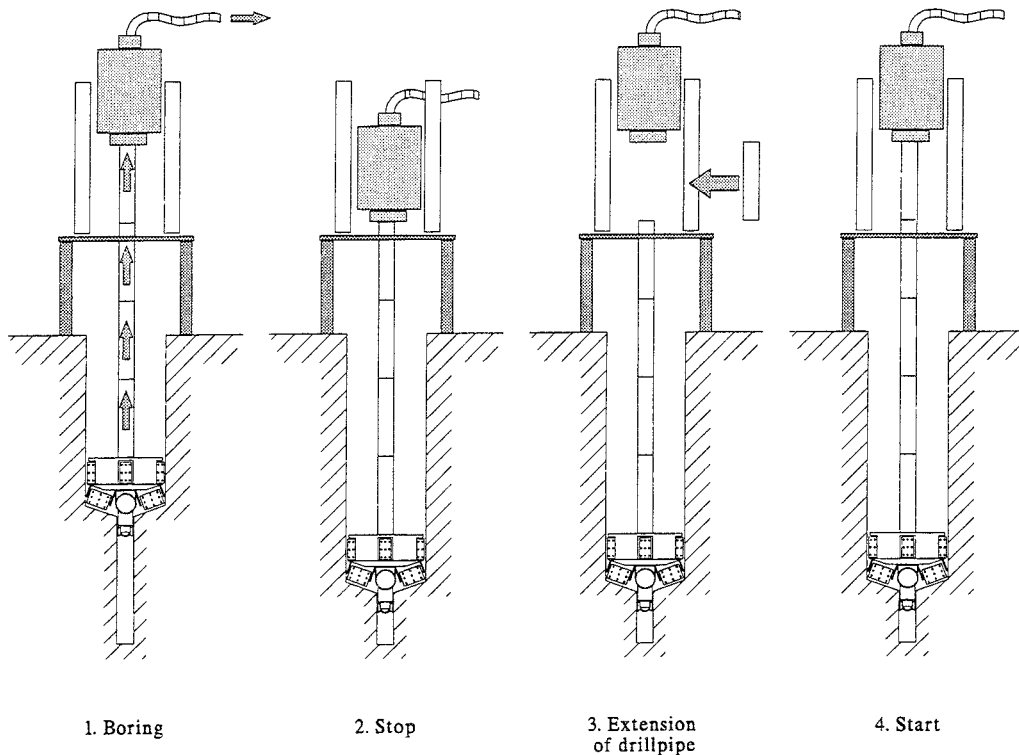
Figure 2.1-1. Operating principle of the boring method.
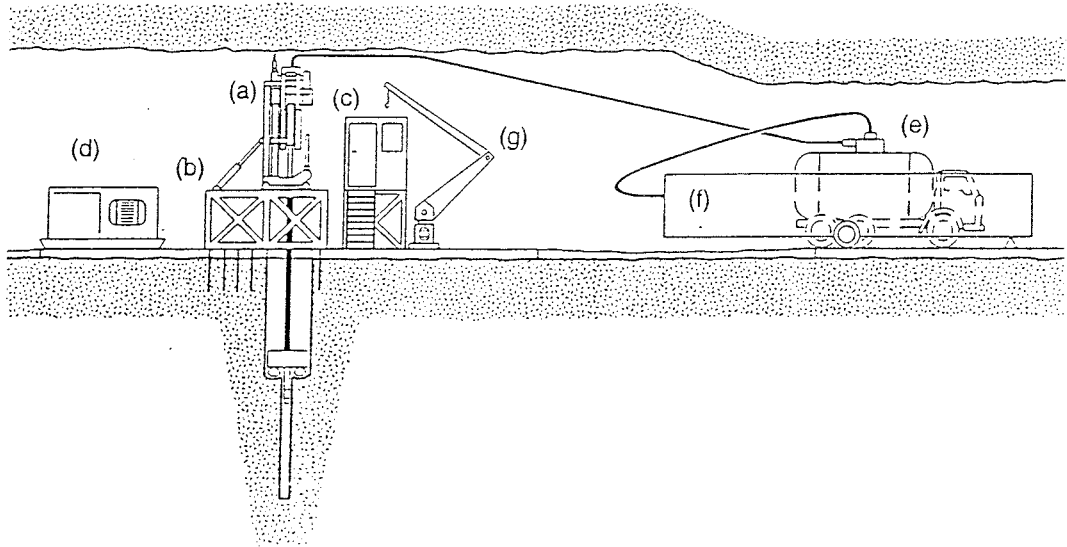
Figure 2.1-2. Drawing of the boring equipment showing the main components: a) boring machine, b) frame, c) control container, d) electro-hydraulic power unit, e) cyclone and tank for crushed rock, f) vacuum unit, g) crane.
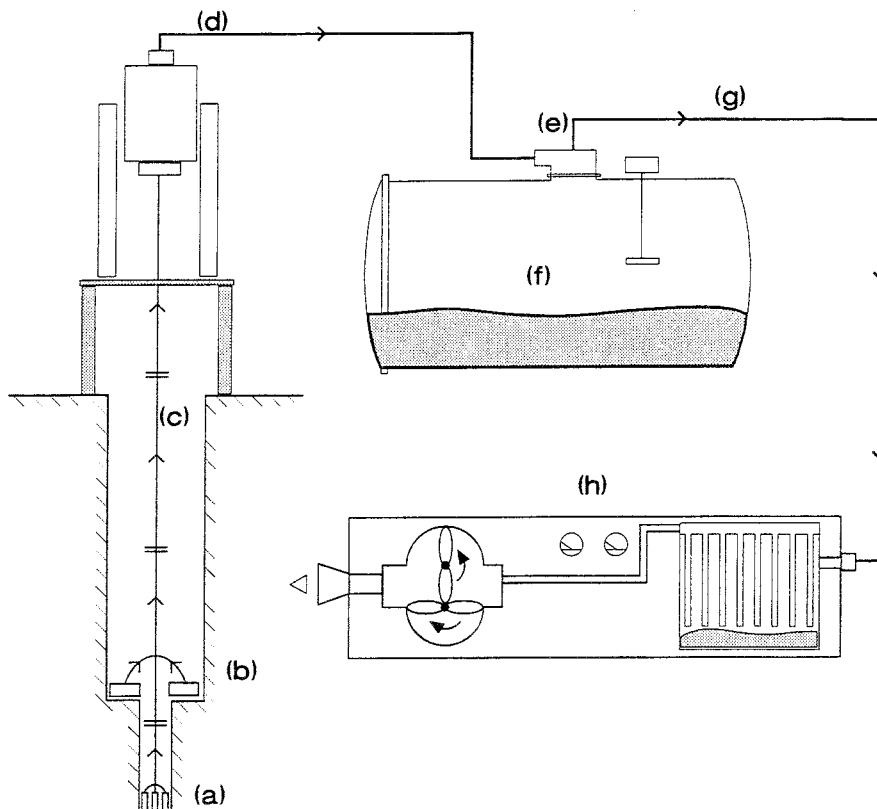
Figure 2.1-3. Flow chart for the vacuum flushing system: a) nozzles in the pilot bit, b) nozzles in the cutter head, c) drill pipes, d) pipe from the boring machine to the tank for crushed rock, e) cyclone, f) tank for crushed rock, g) pipe to the vacuum unit, h) vacuum unit.
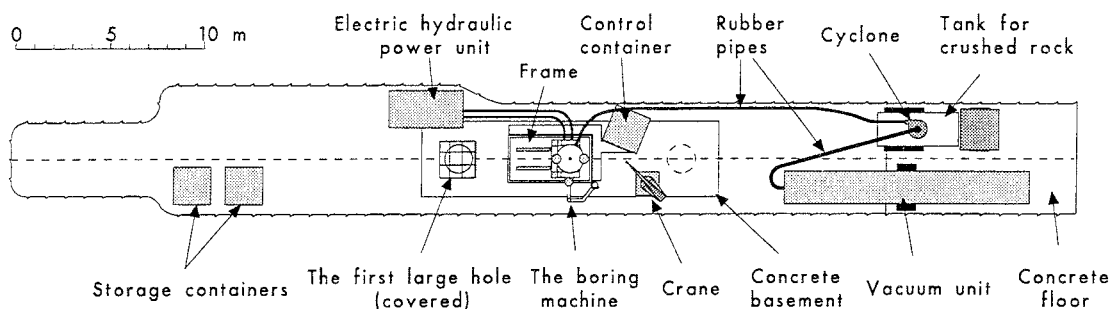
Figure 2.1-4. *Arrangement of the boring equipment in the Research Tunnel.*

2.2 THE BORING MACHINE

The raiseboring machine used to create the torque and thrust necessary for the rotary crushing was of type Subterranean-005L-137. The machine was electro-hydraulic and equipped with a power pack. The main components of the boring machine are shown in Figure 2.2-1.
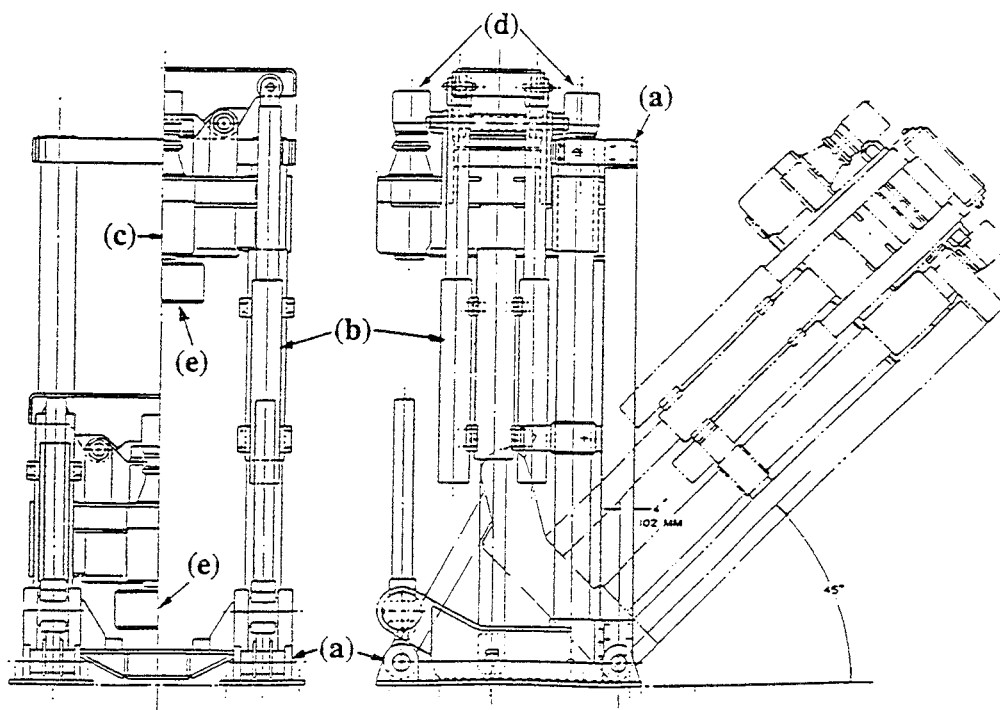
Figure 2.2-1. *Subterranean-005L-137 raiseboring machine. The main components of the machine are: a) base frame, b) hydraulic cylinders, c) gear box, d) rotation motors, e) fastening sleeve for drill string. The device for changing drill pipes and locking is not shown.*

The maximum thrust exerted by the boring machine was measured to be between 500 and 630 kN, depending on the position of the cutter head. The total installed electrical power rating of the boring machine was 151 kW (380 V and 50 Hz).

According to the manufacturer's specifications, the rotation speed could be varied over the range 0-98 rpm. When drilling the pilot holes at the maximum rotation speed of 98 rpm the torque created by the machine was approximately 11 kNm according to the specifications.

According to the manufacturer's specifications, when reaming with the large cutter head the rotation speed could be varied over the range 0-14.6 rpm. At 14.6 rpm the reaming torque was stated to be 74 kNm. In practice, it was observed that the maximum rotation speed with the large cutter head installed was about 12 rpm.

The raiseboring machine was placed on a 1.8 m high base frame so that it was possible to lift the large cutter head for inspection, maintenance and transfer from hole to hole, see Figure 2.2-2. The diameter of the drill pipes was 254 mm (10") and they were 1520 mm long. The inner diameter of the pipes was not constant but exhibited "bottlenecks" which reduced the efficiency of the vacuum flushing process. A polyethylene casing was therefore installed inside the pipes to form a flow path through the drill string with a constant diameter of some 120 mm. Standard stabilizer drill pipes were used behind the pilot bit.
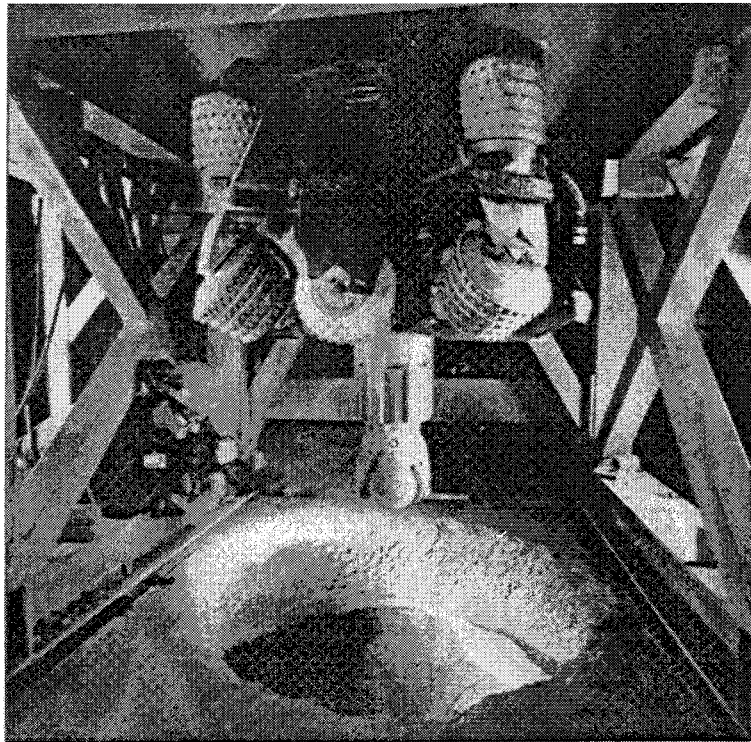
Figure 2.2-2. Cutter head under the base frame and above a bored hole.

2.3 THE PILOT BIT AND THE CUTTER HEAD

The pilot bit was a Sandvik Coromant Roller Bit, a standard three-cone bit with a diameter of 311 mm ($12^1/_4$") intended for use in very hard rock (UCS 250-700 MPa). The shape of the buttons was hemispherical, of type CH.

There were three openings for flushing channels in the bit. Vacuum suction nozzles were installed in these openings for use when boring the pilot holes.

The large cutter head was a used Sandvik Coromant CBH-5 blind-hole head designed for boxhole boring with a hole diameter of 1524 mm, see Figures 2.3-1 and 2.3-2. The weight of the fully-dressed cutter head was 3800 kg.

The large cutter head was furnished with eight roller-button cutters of type Sandvik CMR and four gauge rollers. A combination of 5- and 6-row cutters and 4- and 5-row cutters (see Figure 2.3-4) was used. With the 5- and 6-row cutter dressing the total number of button rows was 44 and with the 4- and 5-row cutter dressing the total number of button rows was 36. The corresponding numbers of grooves on the bottom of the excavated hole were 30 and 24 since some of the button rows followed the same groove.
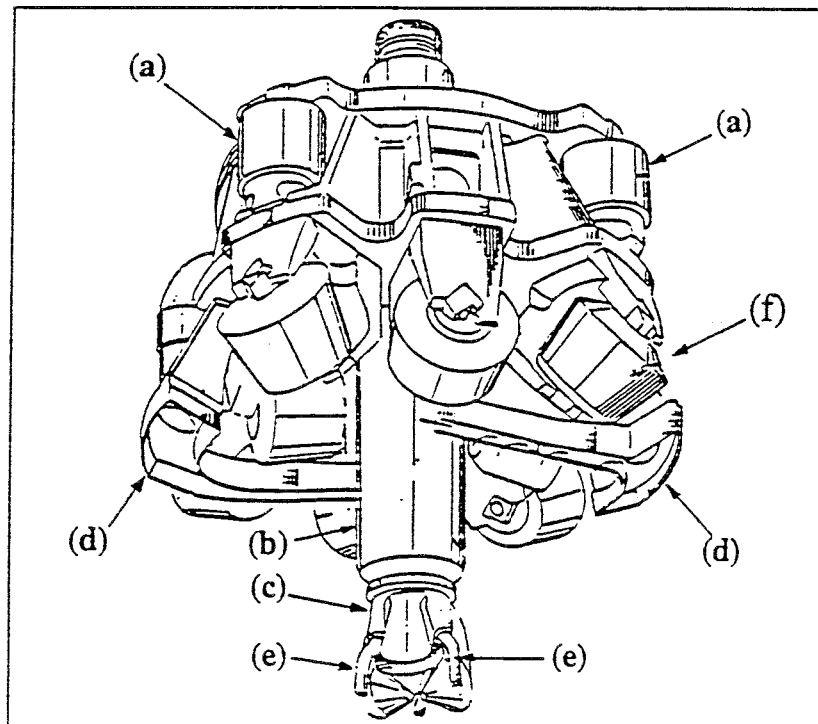
Figure 2.3-1. The Sandvik Coromant CBH-5 cutter head and the vacuum suction nozzles: a) gauge rollers, b) drill pipe and stem of pilot bit, c) pilot bit, d) nozzles in the cutter head, e) nozzles in the pilot bit, f) cutters.

With the 5- and 6-row cutters the row spacing was 39.6 mm and with the 4- and 5-row the row spacing was 51 mm. The corresponding spacings between grooves on the bottom of the hole were 19.8 and 25.5 mm, see Figure 2.3-3.

The two nozzles used to suck out the crushed rock were installed between the cutters in the cutter head.

With the cutter head rotating at 10 rpm the suction nozzles remained above each point on the bottom of the hole for 0.6 seconds. A rubber edging was fitted to the lower edge of the nozzles, the edge closest to the bottom of the hole.
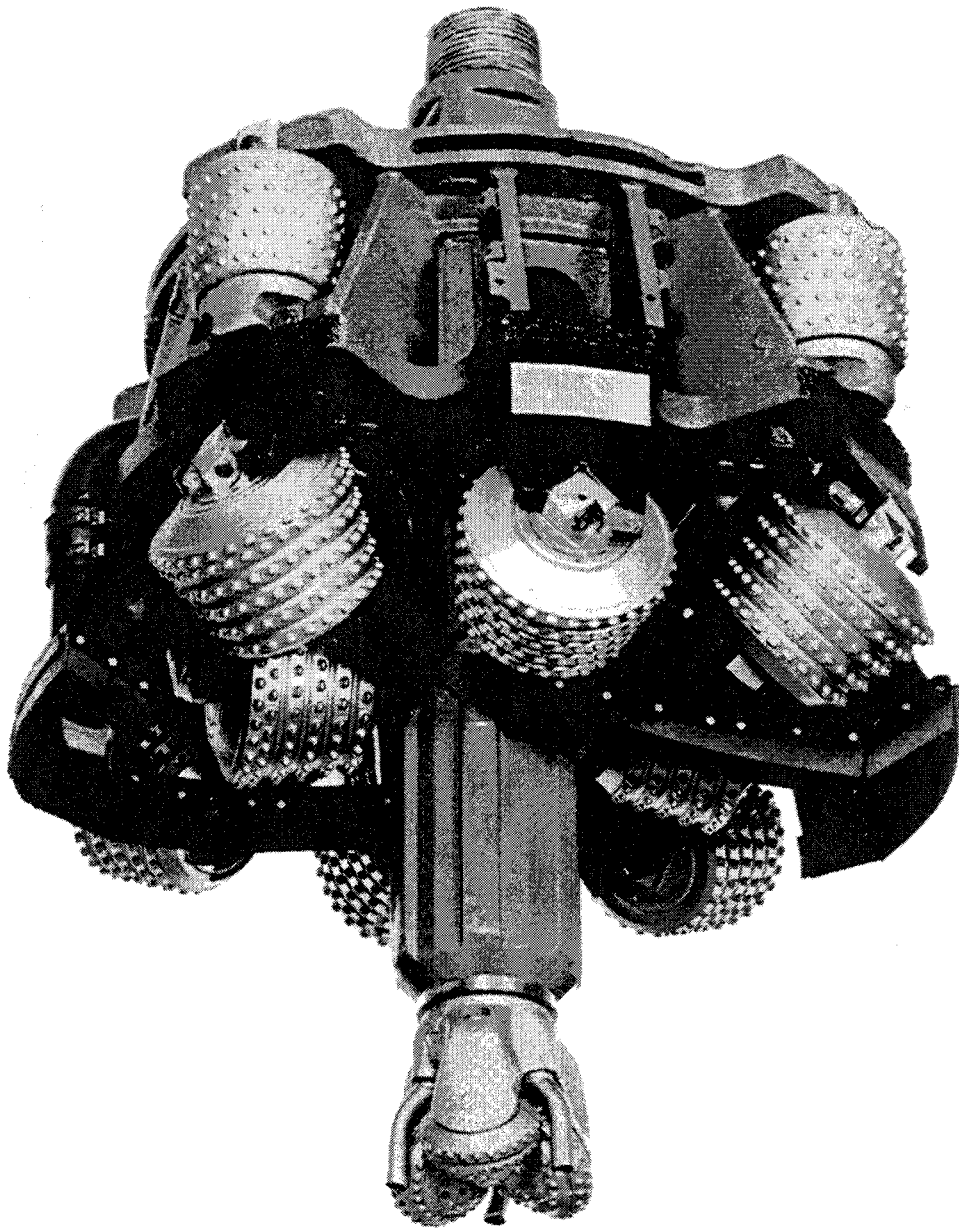
Figure 2.3-2. The cutter head.
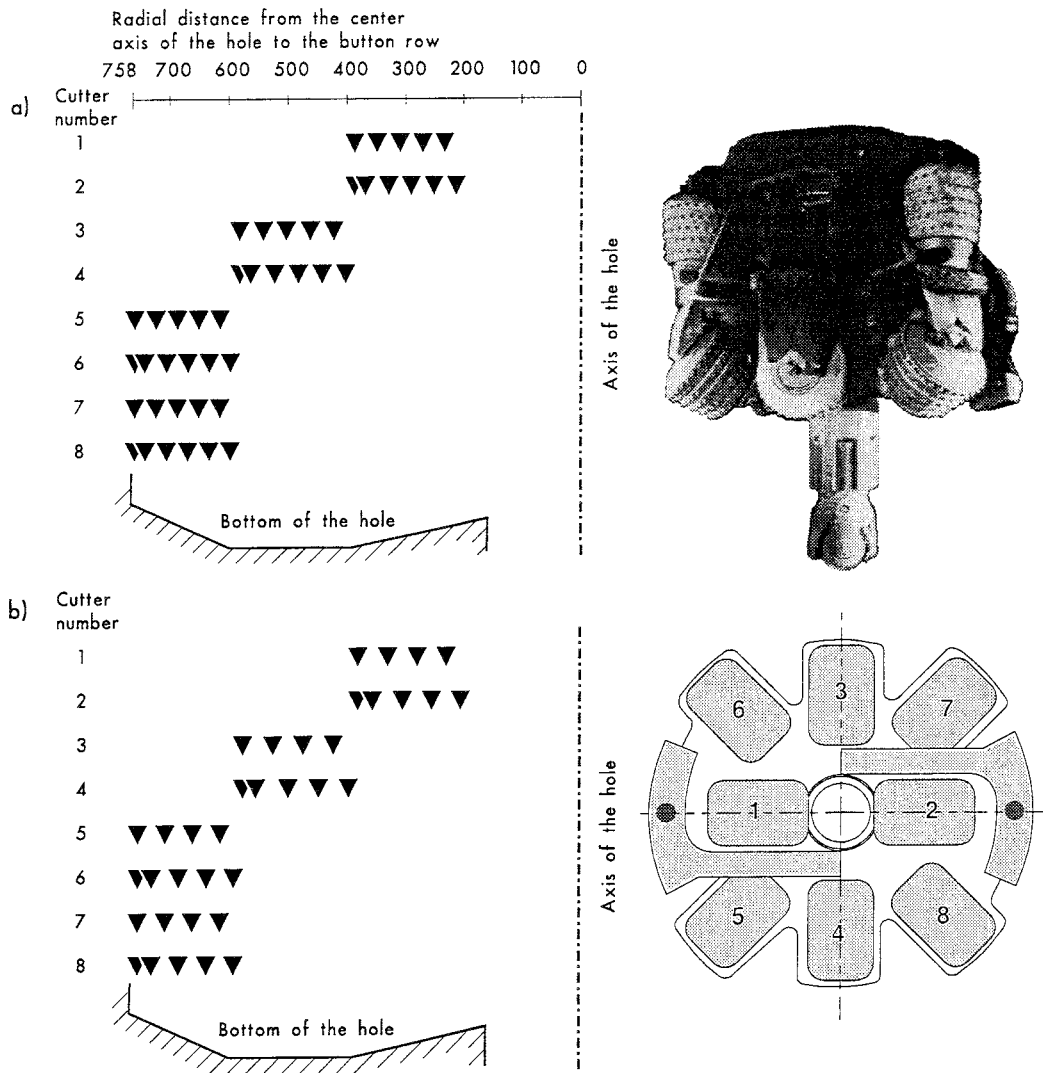
Figure 2.3-3. Positioning of button rows in the cutters. The cutter head was furnished with cutters of type a) CMR-41 & -52, b) CMR-55 & -66.
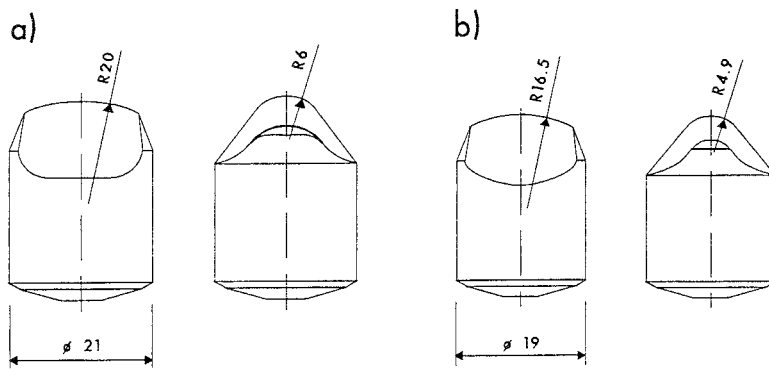
Figure 2.3-4. The shape of the buttons in cutters of type a) CMR-41 & -52, b) CMR-55 & -66.

3 GEOLOGY OF THE HOLES

3.1 GEOLOGY AND MINERALOGY

The VLJ-repository has been excavated in an east-west striking tonalite formation surrounded by mica gneiss. The rock types found in the Research Tunnel are gneissic tonalite and pegmatite, see Figure 3.1-1. The tonalite is usually slightly-foliated, medium-grained, massive and sparsely-fractured. Besides the gneissic tonalite, which is referred to as anisotropic tonalite or gneissic tonalite, a fine-grained, homogeneous tonalite variant is also met. Pegmatite is found as veins and is non-foliated, coarse-grained, massive and sparsely-fractured (Äikäs & Saclén 1993 and 1995).

The main rock type found in the large holes is gneissic tonalite. Minor sections consisting of pegmatite are found at the upper ends of holes R2 and R3. In addition, a small section consisting of homogeneous tonalite is found in hole R3 between the pegmatite and anisotropic tonalite. This can be seen in the investigation core samples (Figure 3.1-2 and 3.1-3), the geological fracture maps (Figures 3.1-4, 3.1-5 and 3.1-6) and the photographs of the large holes (Figures 3.1-7, 3.1-8 and 3.1-9). The orientation of fractures in the Research Tunnel can be divided into four different groups, of which the set of steeply-dipping fractures (dip direction east-west) is dominant (Figure 3.1-10).

Characterization of the Research Tunnel included comprehensive hydrological studies. The inflow of water into the investigation holes and later, into the full-scale holes, was measured. The results of these hydrological studies are reported elsewhere (Hautojärvi 1994, Hautojärvi et al. 1993, 1994 and 1995).
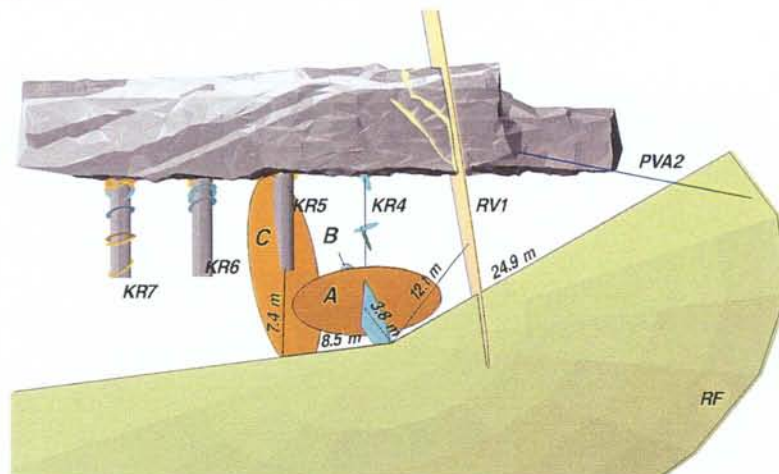
Figure 3.1-1. 3-D model of the Research Tunnel showing the hydraulically-conductive fracture zones in the vicinity of the tunnel and the three experimental full-scale deposition holes. Fractures found in the investigation core holes are shown. Pegmatite veins are shown shaded in lighter gray.
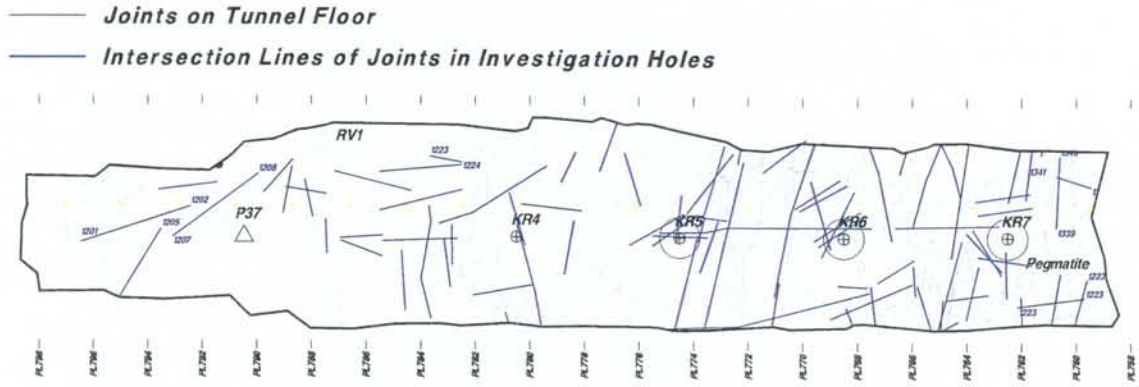
Figure 3.1-2. Floor plane of the Research Tunnel showing the surface topography, geology and the location of the investigation holes KR5-KR7 which were drilled in the position of the full scale experimental deposition holes.
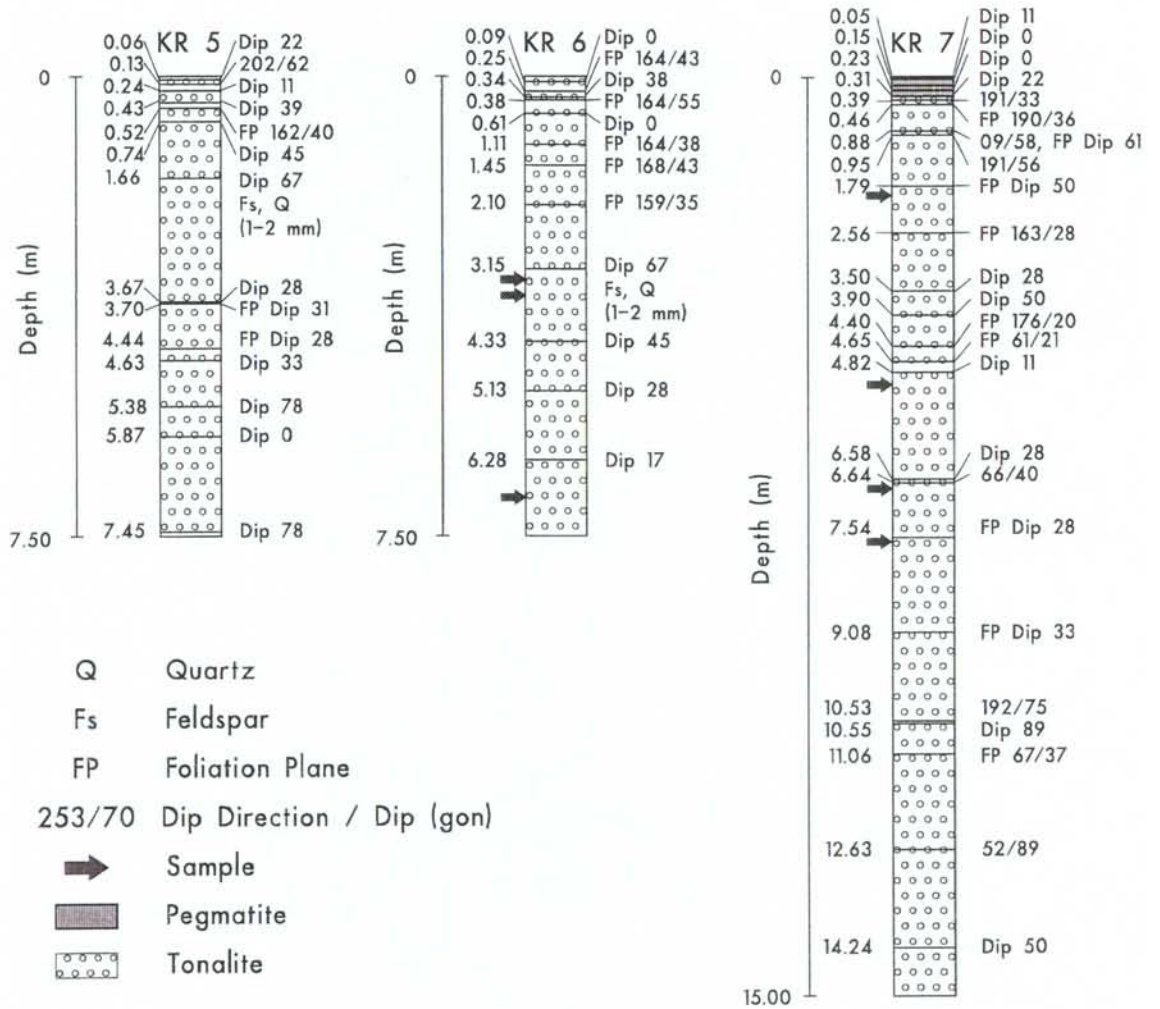
Figure 3.1-3. Diagram of investigation core samples showing rock types and fractures in the investigation boreholes KR5-KR7.
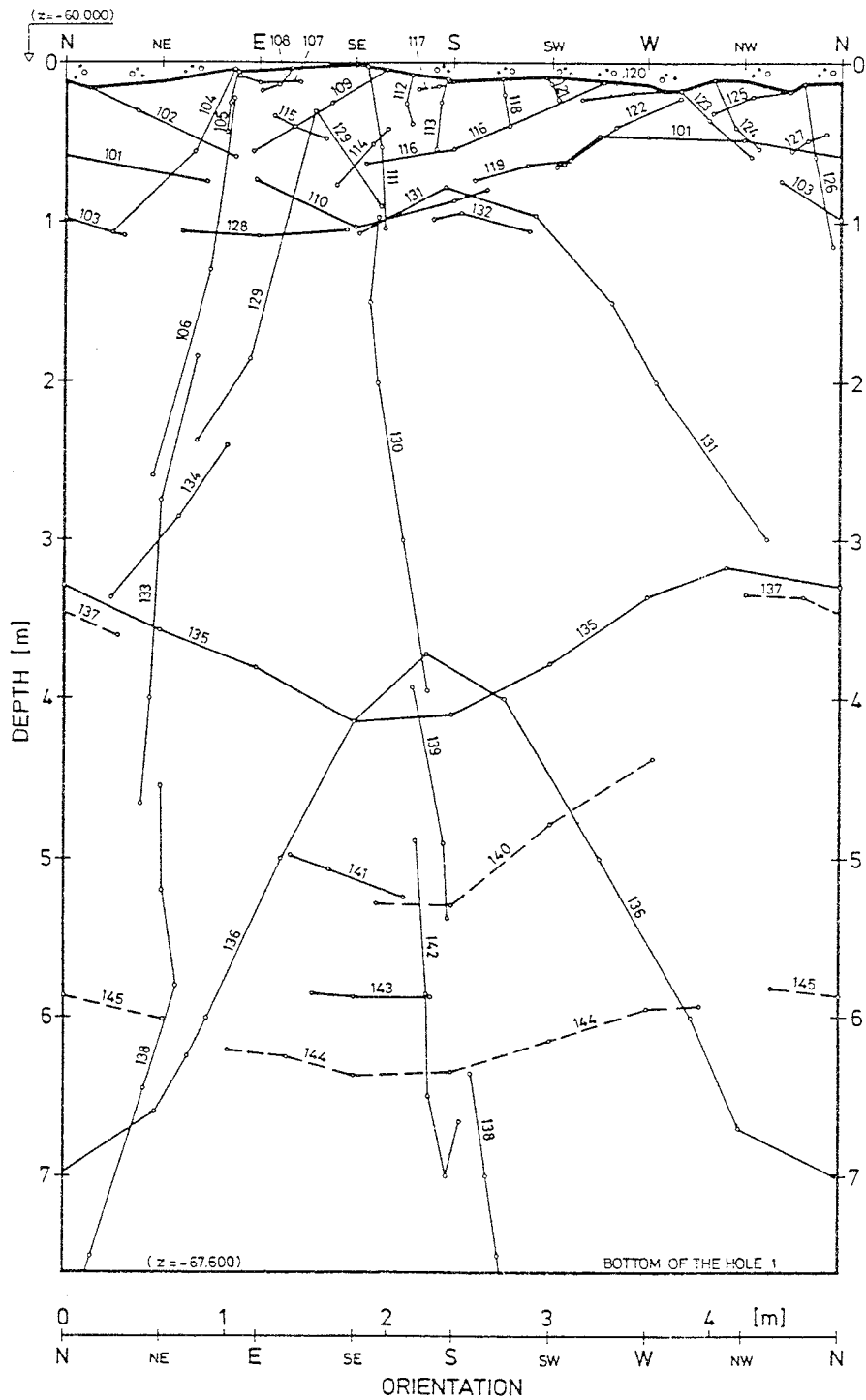
Figure 3.1-4. Geological map of Large hole 1. The solid lines show fracture traces and the dashed lines show foliation planes.
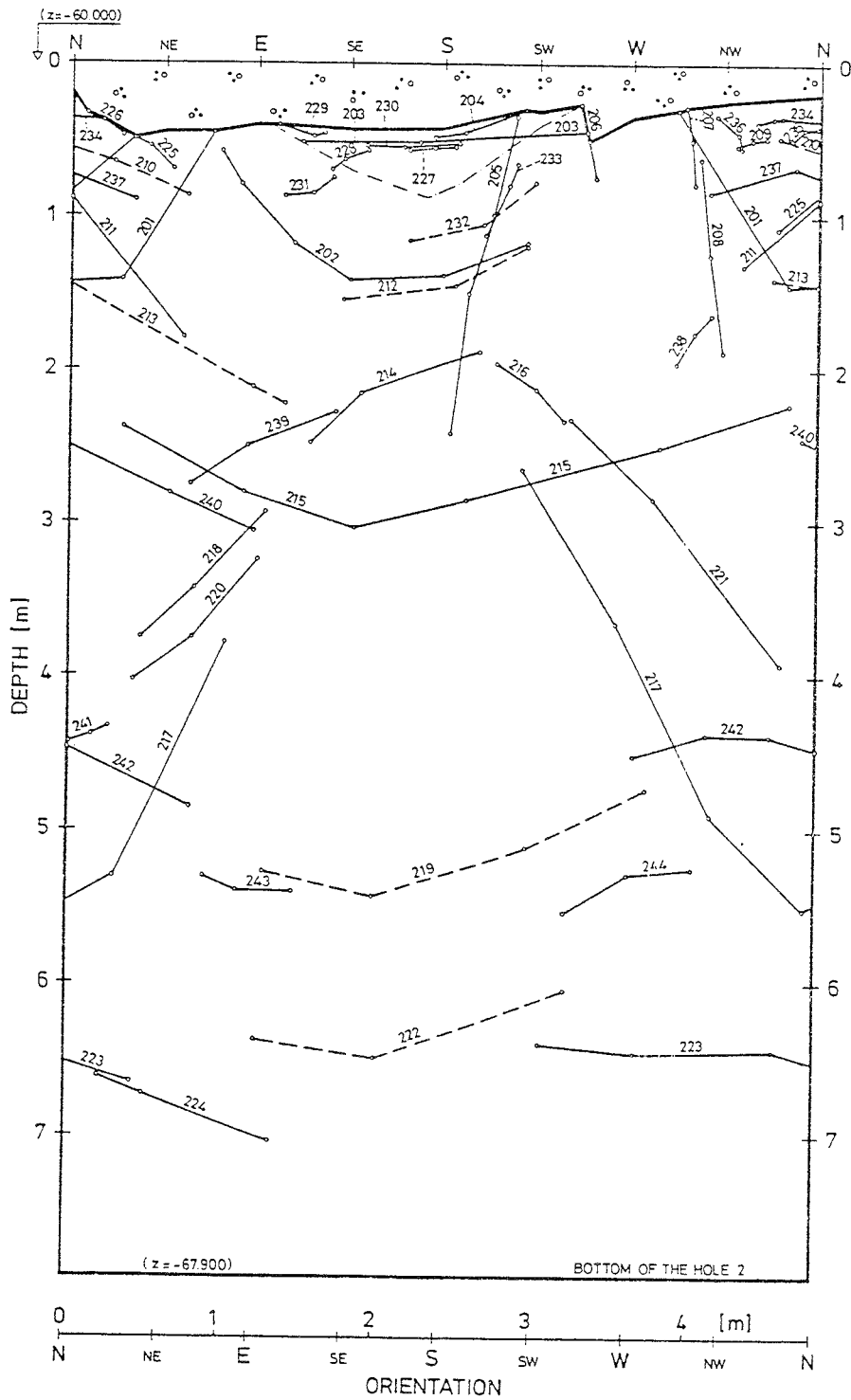
Figure 3.1-5. *Geological map of Large hole 2. The solid lines show fracture traces and the dashed lines show foliation planes.*
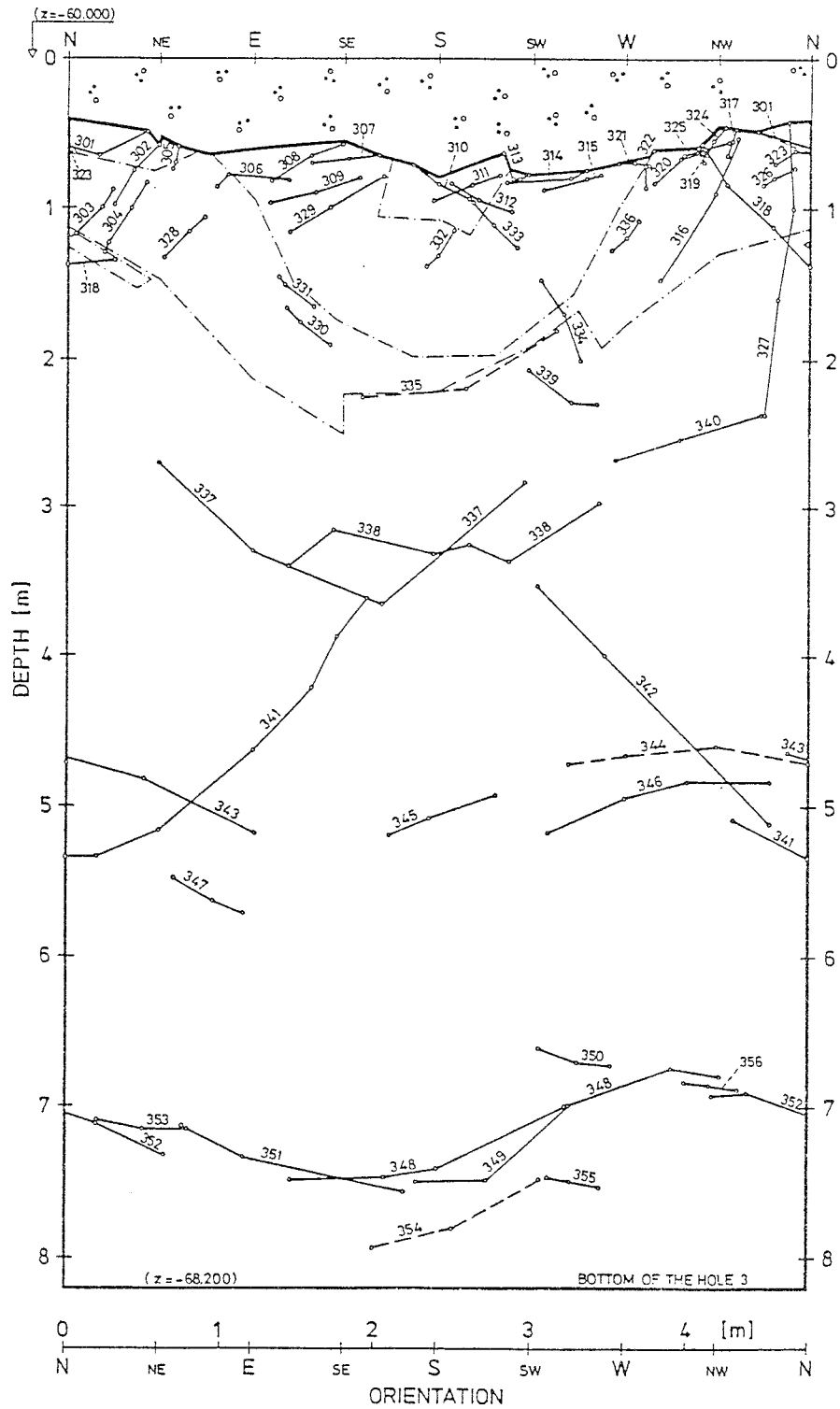
Figure 3.1-6. *Geological map of Large hole 3. The solid lines show fracture traces and the dashed lines show foliation planes.*
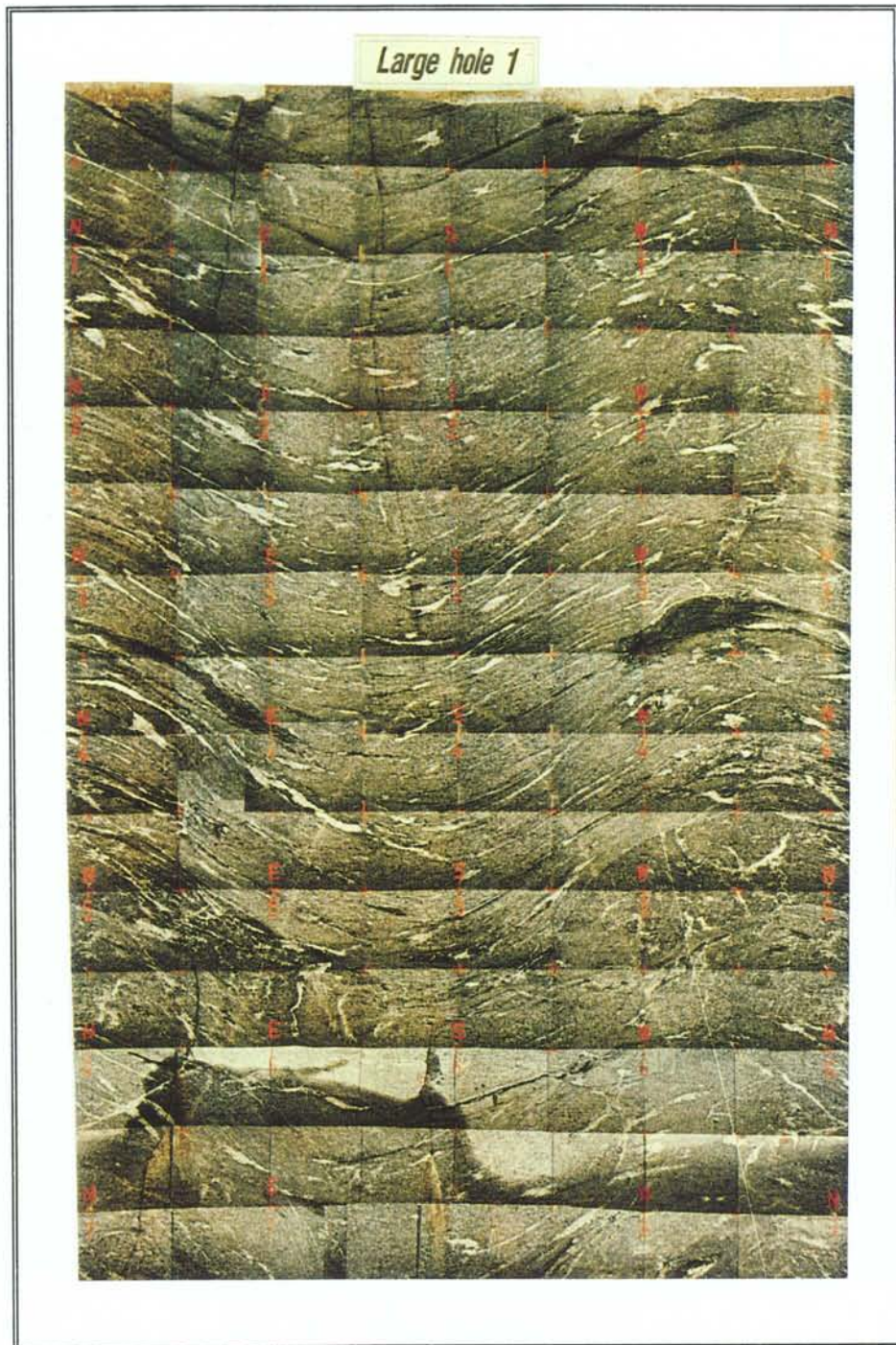
Figure 3.1-7. A photomosaic of the surface of Large hole 1.
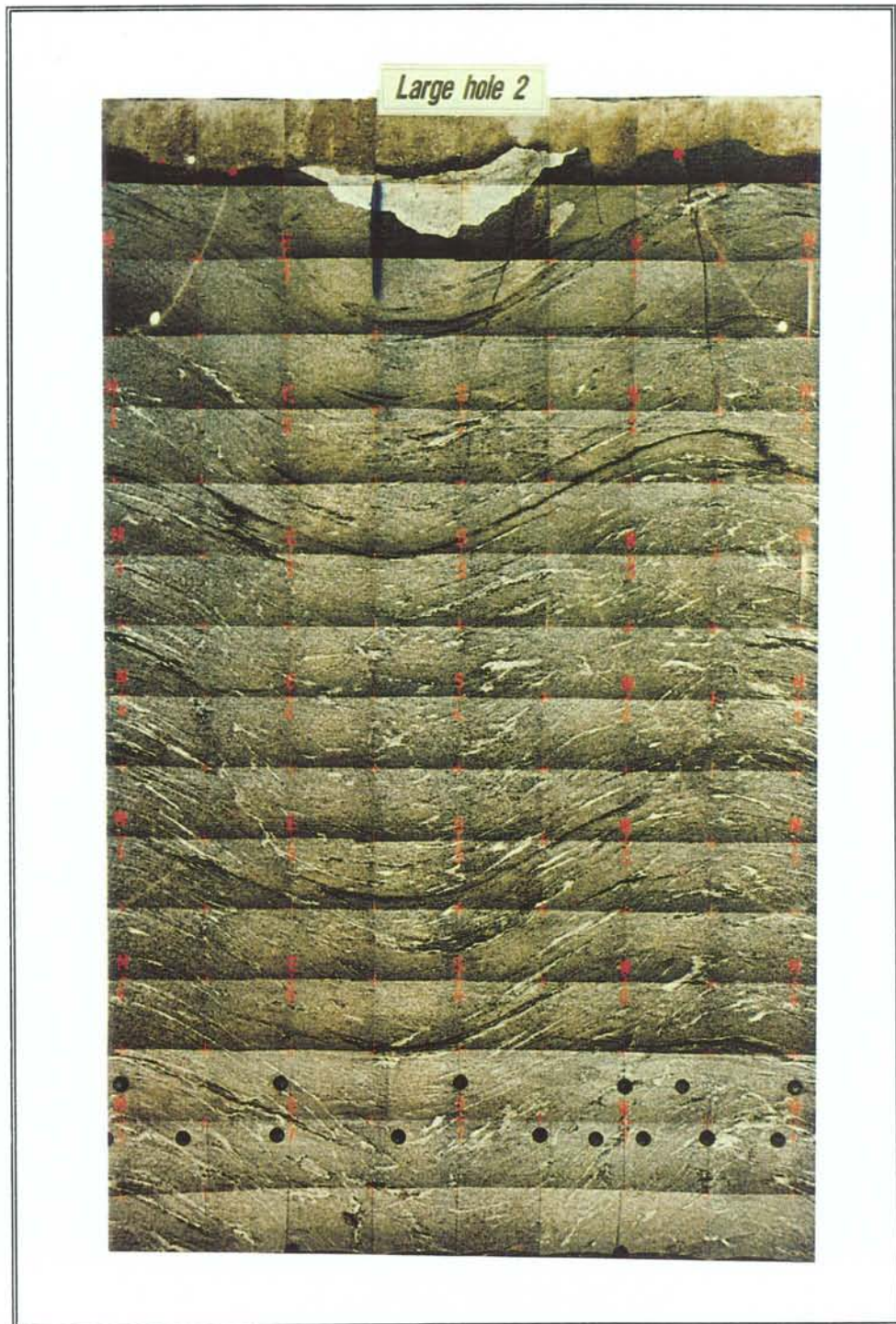
Figure 3.1-8. *A photomosaic of the surface of Large hole 2. The location of sample holes is also shown (diameter 98 mm).*
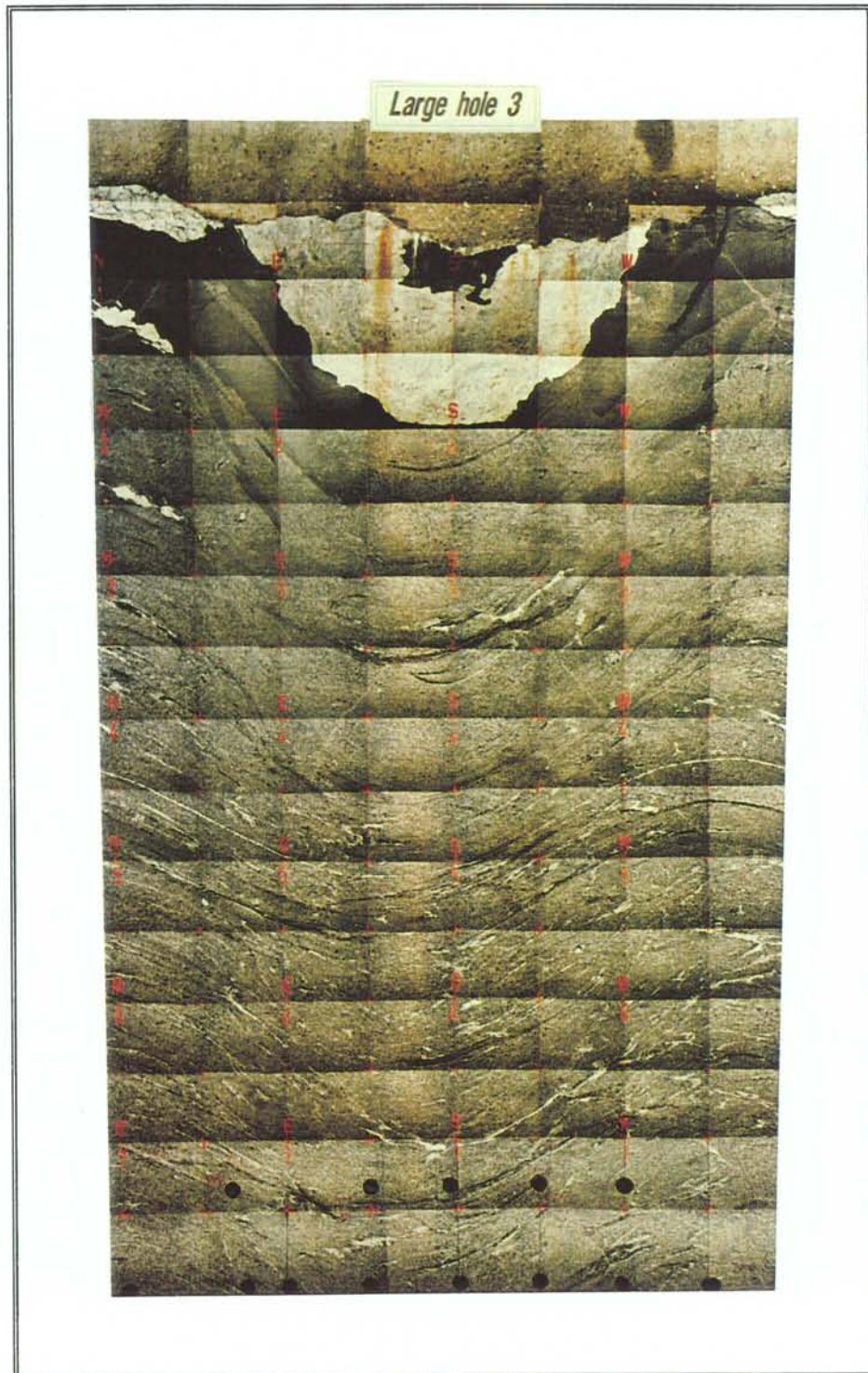
Figure 3.1-9. *A photomosaic of the surface of Large hole 3. The location of sample holes is also shown (diameter 98 mm).*
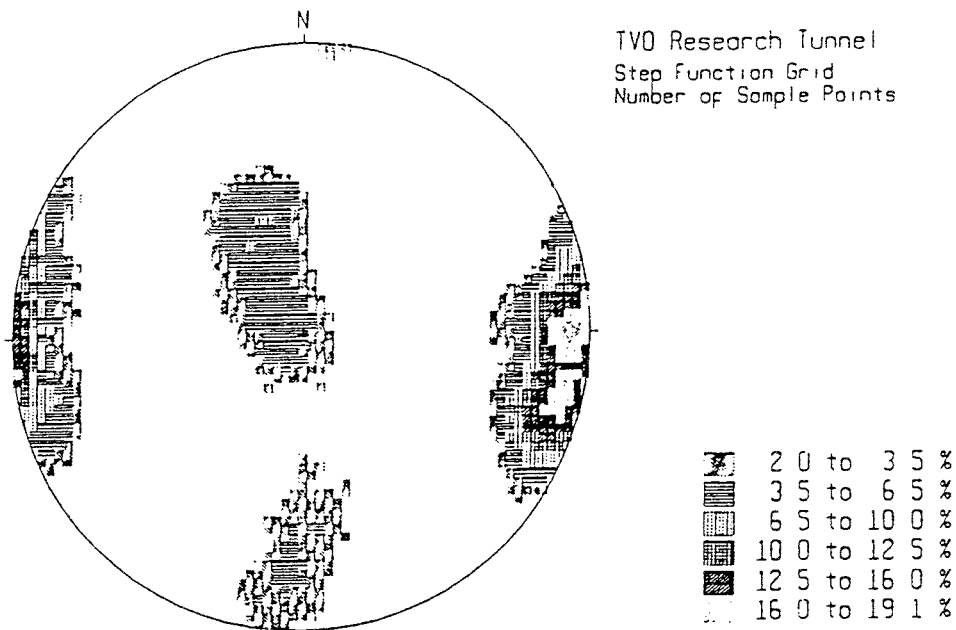
Figure 3.1-10. Distribution of fracture orientations in the Research Tunnel shown using Schmidt's equal area stereographic projection.

3.2 MINERALOGY AND PETROGRAPHY OF ANISOTROPIC TONALITE

The mineralogy of the gneissic tonalite was determined from Sample B4.111 taken from Test Section B (see Figure 7.1-1 in section 7.1). From a visual viewpoint the texture of the sample was considered to be representative of the average texture and mineralogy of the main rock type and, in particular, the sections of rock studied for excavation disturbance. According to the microscopic thin section examination (Figure 3.2-1) and point counting method carried out by the Geological Survey of Finland, the main minerals in the anisotropic tonalite (see Table 3.2-1) are quartz (16.4%), plagioclase (37.2%), biotite (29.6%) and hornblende (11%), making up about 94% of the total content. This division is consistent with results obtained at an earlier date and shown in Table 3.2-2, which represents a larger volume of rock in the Research Tunnel. The mafic minerals, especially oblong grains of biotite and hornblende are oriented. The grains are subhedral and the alteration to secondary minerals is insignificant.

The grain size of the quartz is 0.3-0.5 mm even though the size of the quartz clusters is 1-2 mm. The grain size of the plagioclase is larger, the largest grains observed being between 2 and 3 mm in size. The anorthic content of the plagioclase is 31-32%. Biotite occurs as clusters of flaky grains, typical size 1 to 3 mm.

Table 3.2-1. The mineralogy of gneissic tonalite, sample B4.111.

Mineral	vol.-%
Quartz	16.4
Plagioclase	37.2
Alkali-feldspar	+
Biotite	29.6
Serisite	0.8
Hornblende	11.0
Chlorite	0.4
Epidote	0.4
Apatite	1.8
Sphene	0.8
Zircon	+
Opaque	1.6
Total	100.0 vol.-%

Table 3.2-2. The mineralogy of gneissic tonalite, all samples.

Sample Mineral	TU-2* vol.-%	TU-4* vol.-%	KR6** (67 m) vol.-%	KR6** (65 m) vol.-%	B4.111 vol.-%	Average
Quartz	19.2	11.8	16.4	14.2	16.4	15.6
Plagioclase	50.2	48.2	37.2	53.8	37.2	45.3
Potassium feldspar	+	+	+	-	+	-
Biotite	22.6	25.6	29.6	24.4	29.6	26.4
Hornblende	3.6	10.8	11.0	4.4	11.0	8.2
Sericite/Muscovite	1.8	0.8	0.8	0.4	0.8	0.9
Chlorite	0.6	0.4	0.4	0.4	0.4	0.4
Calsite/Carbonate	-	-	-	+	-	-
Epidote	0.2	+	0.4	+	0.4	0.3
Apatite	1.2	1.4	1.8	2.0	1.8	1.6
Sphene	0.2	-	0.8	-	0.8	0.6
Zircon	+	+	+?	+	+?	-
Opaque	0.4	1.0	1.6	0.4	1.6	1.0
Total	100.0	100.0	100.0	100.0	100.0	100.3

* Samples TU-2 and TU-4 were taken from investigation holes KR6 (depth 6.8 m) and KR7 (depth 5 m) respectively, depths being measured from the tunnel floor (Johansson & Autio 1995).

** Samples KR6 (67 m) and KR6 (65m) were taken from from investigation hole KR6 (at the location of the subsequent Large hole 2, see Fig. 3.1-2) at depths of 7 m and 6 m from the tunnel floor (60 m level) respectively.

According to the results obtained using the ^{14}C-PMMA method and investigation by scanning electron microscope (SEM) the undisturbed rock matrix is solid and intragranular fissures are sparse. This observation is supported by the results of the optical microscopic examination. According to the ^{14}C-PMMA autoradiograms and microscopic examination, the properties of the rock matrix are characterized by oriented clusters of mafic minerals with higher porosity, as seen in Figure 3.2-2. The mineralogical content of the gneissic tonalite in the Research Tunnel and the basis for specification is shown together with the general classification of plutonic rocks in Figure 3.2-3.
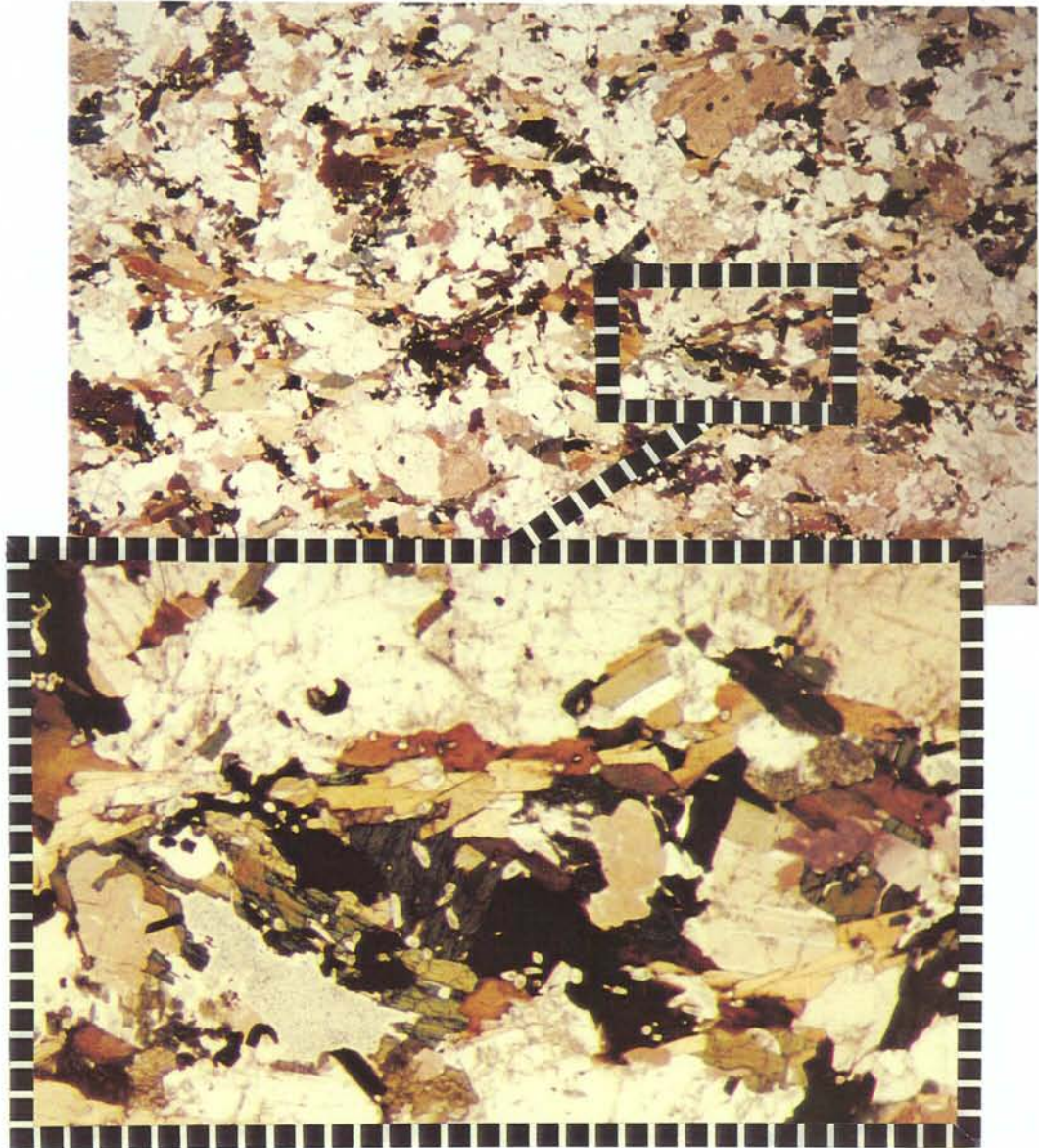
Figure 3.2-1. Photographs of a thin section of tonalite (sample B4.111, parallel nicols). The upper photograph is shown at a magnification of 5x, the autoradiograph in Figure 3.2-2 is corresponding to this one. Part of the photograph is shown also at a magnification of 25x (bottom). The quartz is mainly clear, the plagioclase is grayish and lamellar, the biotite is different shades of brownish-green, and the hornblende is darkish-green.
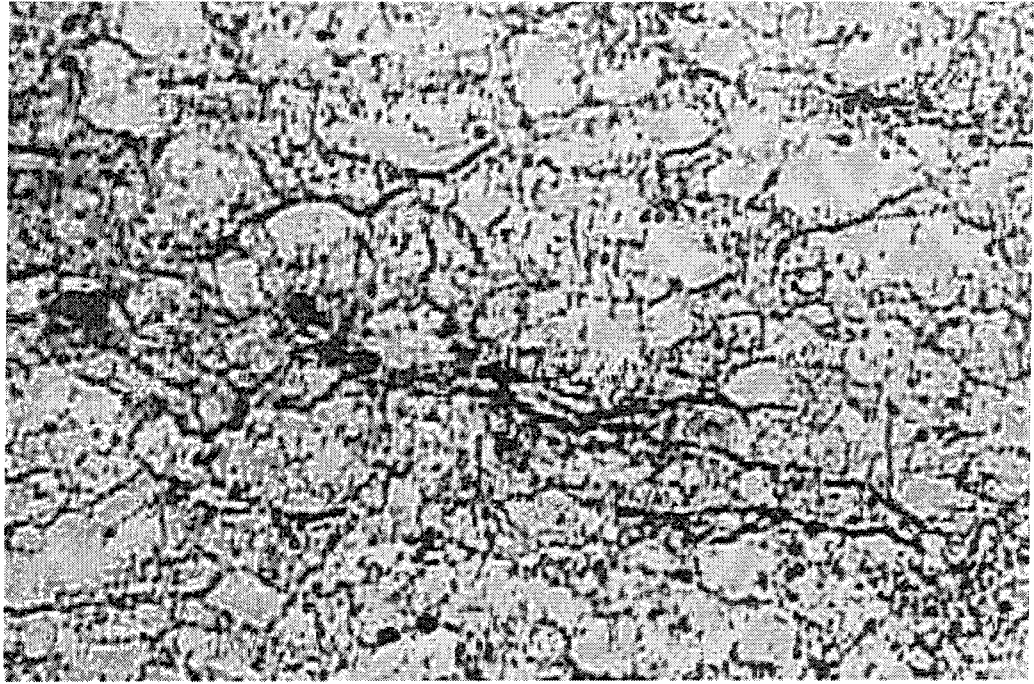
Figure 3.2-2. *Audioradiogram of the same section of rock sample B4 as that shown in Figure 3.2-1 as a thin section. The darker, fracture-like features are areas of increased porosity.*
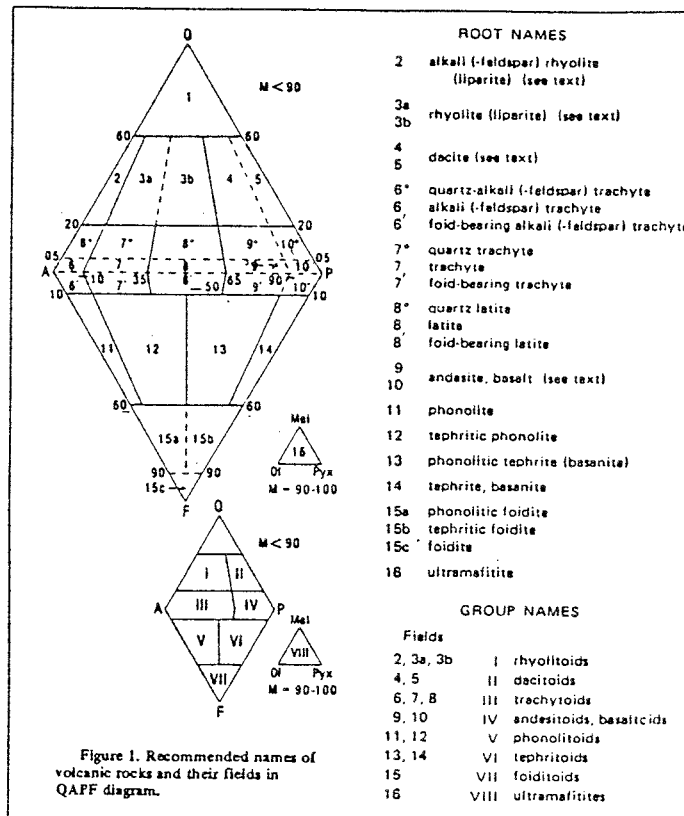
Figure 3.2-3. *The Q-A-P content of the tonalite in the large holes and the general classification of igneous rocks.*

4 MECHANICAL PROPERTIES OF THE TONALITE

According to stress measurements (Kuula & Johansson 1991, Nykyri et al. 1991) carried out before the construction of the VLJ-repository and the Research Tunnel the state of in-situ stress at the VLJ-repository and in the area of the Research Tunnel is low. Measured values of in-situ stress averaged from 5 to 6 MPa at the level of the repository. The results obtained from monitoring of the rock displacement during and after construction of the repository are consistent with the stress measurements (Nykyri et al. 1994).

The rock mechanical properties of intact rock in area the Research Tunnel were determined from irregular block samples of rock and from core samples extracted from the investigation holes (KR4, KR5, KR6 and KR7).

4.1 DRILLING RATE INDEX, DRI

The average DRI value obtained for the gneissic tonalite, the main rock type, was 55 and is typical for this rock type, see Figure 4.1-1. The average brittleness value S_{20} was 51 and the Sievers' SJ value was 32. The average DRI value for the pegmatite, 49, was slightly lower than values found in the literature. The DRI value of the pegmatite is close to that for gneissic tonalite, and according to their drillability both rock types can be classified as medium-hard (Lien R. 1980).
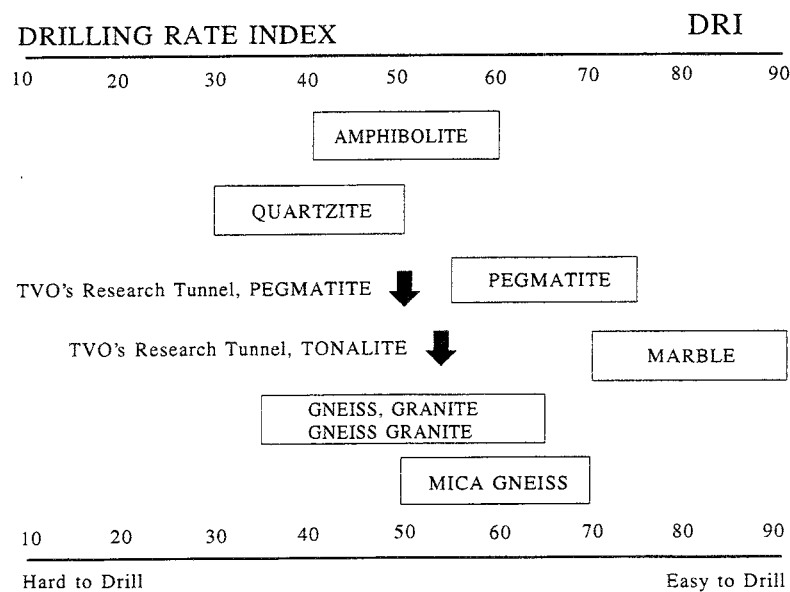
Figure 4.1-1. Variation of DRI in various rock types and the average DRI values determined for the rock types in the Research Tunnel (Johansson 1994).

The diagram of DRI value against compressive strength shown in Figure 4.1-2 implies that the values obtained are within the normal range, which for granitic rock is generally wide. The diagram of DRI value against quartz content shown in Figure 4.1-3 shows the general trend of decreasing DRI value with increasing quartz content.
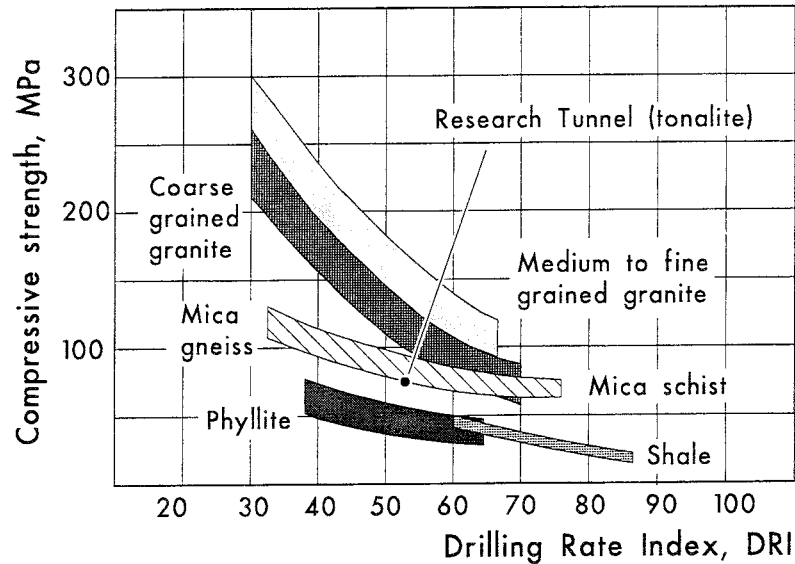
Figure 4.1-2. Relation between Drilling Rate Index, DRI and compressive strength in granitic rocks and in the Research Tunnel (Johansson 1994).
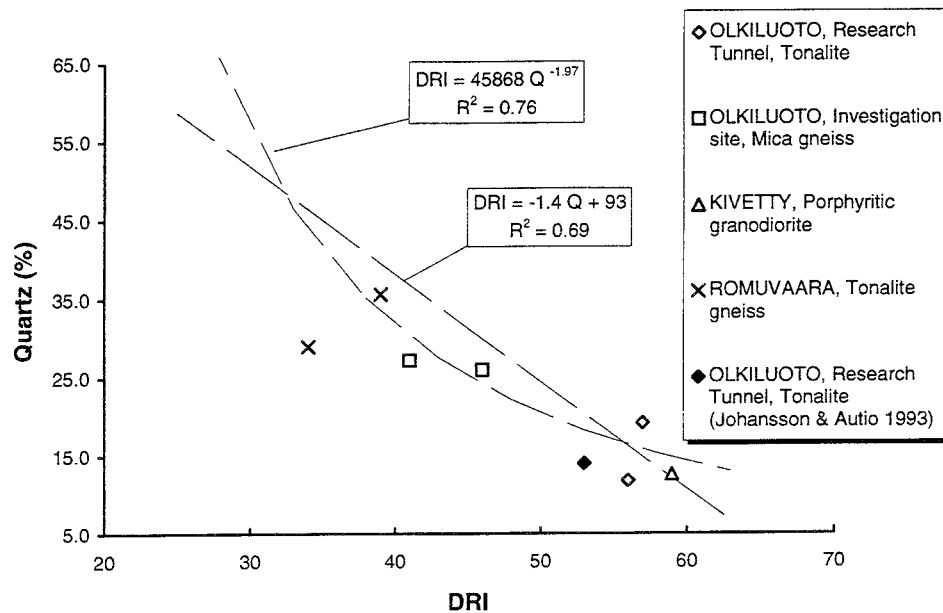
Figure 4.1-3. DRI values for gneissic tonalite in the Research Tunnel plotted as a function of quartz content. Values from three other investigation sites and the corresponding regression functions are also shown (Johansson & Autio 1995).

4.2   STRENGTH AND DEFORMATION PROPERTIES

The results obtained for the strength and deformation properties of both the tonalite and the pegmatite were very similar to the corresponding results obtained during the construction of the VLJ-repository (Johansson & Autio 1993). Tables 4.2-1 and 4.2-2 and Figures 4.2-1, 4.2-2, 4.2-3 and 4.2-4 contain all the results available for the rock mechanical parameters of the gneissic tonalite (Johansson & Autio 1993, Johansson & Autio 1995). The average value of compressive strength for gneissic tonalite, 80 MPa, is lower than that of typical granitic rocks and homogeneous tonalite (112 MPa). The gneissic tonalite, the most common form of tonalite in the Research Tunnel, exhibits compressive strength values that are clearly lower than the homogeneous tonalite encountered only in the upper part of borehole KR7. The tensile strength of the gneissic tonalite, 9 MPa, and its deformation properties (Young's modulus 60 GPa) are typical of those for granitic rocks. The tensile strength of the homogeneous tonalite was 10 MPa and its Young's modulus was 66 GPa.

Table 4.2-1. Average rock mechanical properties of the gneissic tonalite in the Research Tunnel.

Peak strength (MPa)	Tensile strength (MPa)	Young's modulus (GPa)	DRI value	CAI value	Quartz content (%)	Joint freq. pcs/m
80	9	60	55	3.8	15-20	1.0

Table 4.2-2. Compressive strength (UCS), Crack initiation strength and Crack damage strength of gneissic tonalite samples from the Research Tunnel.

Property Test sample	Compr. strength (MPa)	Tensile strength (MPa)	Crack Initiation (CI) (MPa)	(% of UCS)	Crack Damage (CD) (MPa)	(% of UCS)
VLJ- KR6- 3.55 m	84.4	6.2	26.1	23.0	74.2	87.8
VLJ- KR6- 6.85 m	91.9	7.6	43.4	35.0	80.0	87.0
VLJ- KR7- 1.90 m	99.6	12.1	43.3	32.2	87.6	88.0
VLJ- KR7- 5.00 m	86.1	10.5	28.4	24.4	77.7	90.3
VLJ- KR7- 6.69 m	95.8	10.7	43.4	33.6	85.7	89.5
average	91.6	9.4	36.9	29.6	81.0	88.5

STRENGTH PROPERTIES OF TONALITE
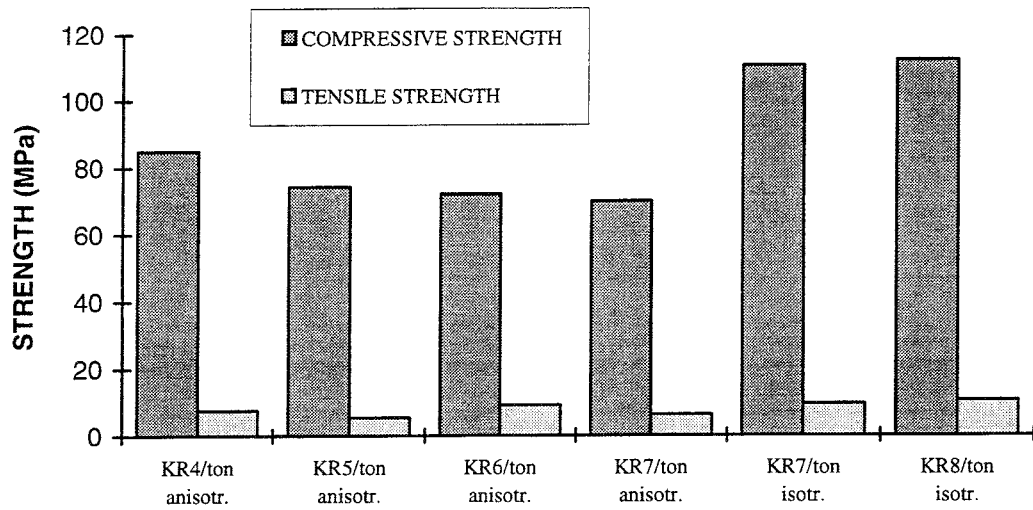
Figure 4.2-1. Strength properties of gneissic and homogeneous tonalite in the Research Tunnel (Johansson & Autio 1993).

OLKILUOTO, RESEARCH TUNNEL
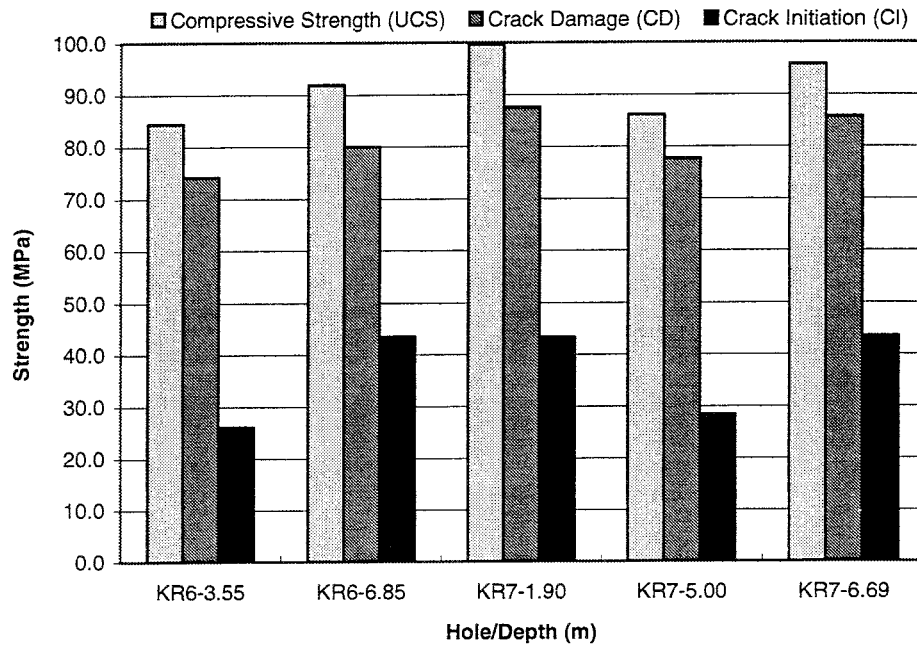
Figure 4.2-2. Strength properties of gneissic tonalite in the Research Tunnel (Johansson & Autio 1995). The values shown include the Crack damage and Crack initiation stress determined from the stress-strain curve.

OLKILUOTO, Research Tunnel, Tonalite
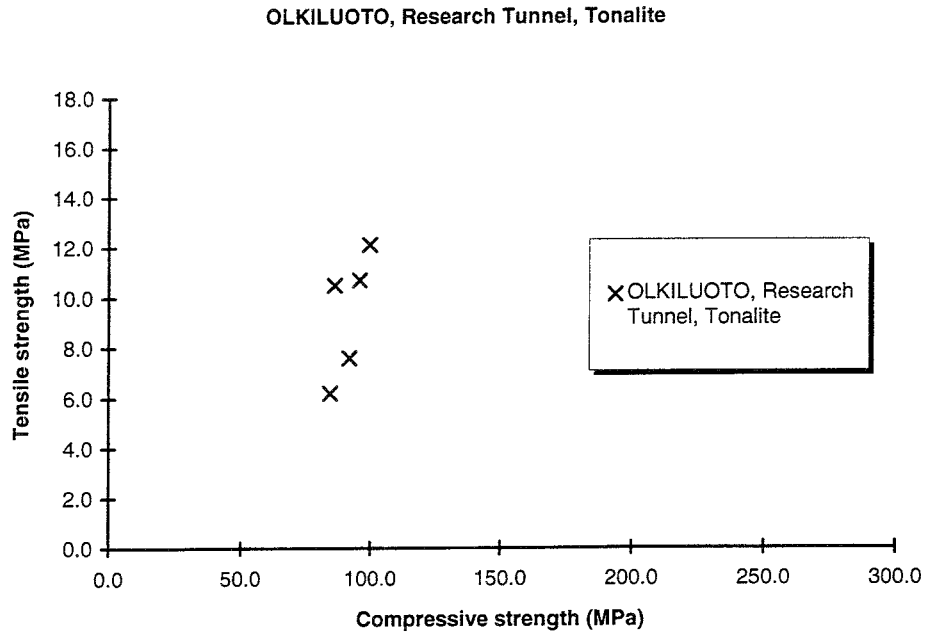
Figure 4.2-3. Compressive strength of the gneissic tonalite shown in Figure 4.2-2 plotted as a function of tensile strength.
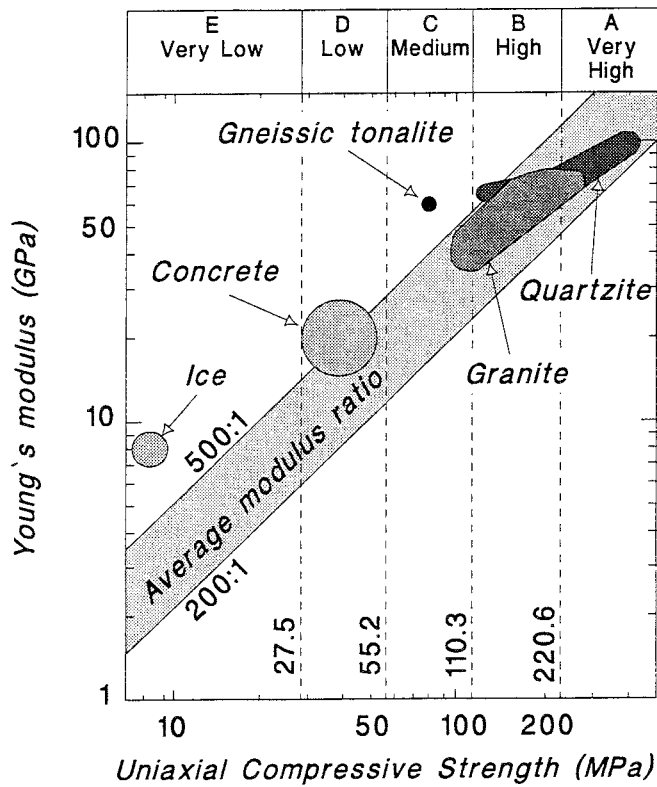
Figure 4.2-4. The position of gneissic tonalite in Deere's classification system.

4.3   CERCHAR ABRASITIVY INDEX, CAI

The CAI (Cerchar Abrasitivy Index) indicates the abrasiveness of a rock. The average CAI value obtained for the main rock type, anisotropic tonalite, was 3.8, see Table 4.2-1, classing it as very abrasive, see Figure 4.3-1.
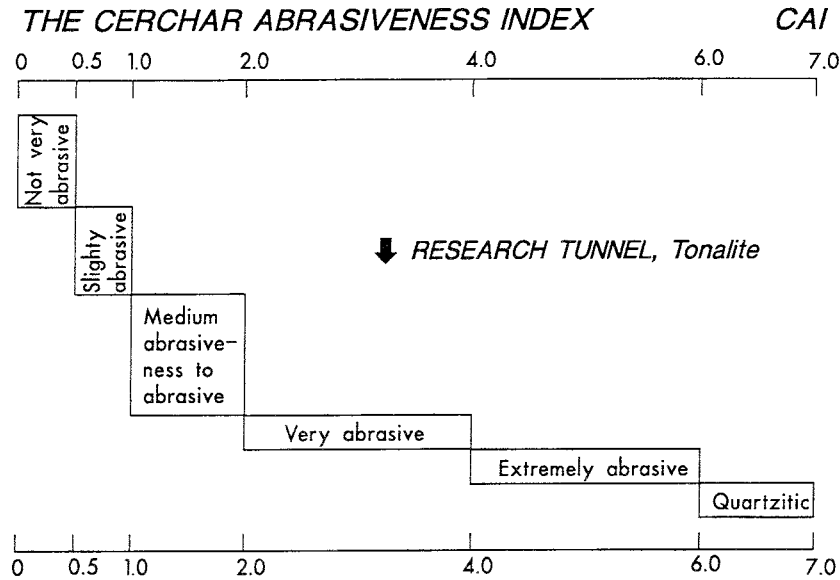
Figure 4.3-1. The average CAI value of gneissic tonalite with respect to the Cerchar abrasiveness classification.

4.4   PROPERTIES OF TONALITE FORMING MINERALS

The degree of mechanical disturbance caused by the boring process in the rock adjacent to the surface of the full-scale holes is a function of the grain structure and properties of the rock. The main minerals, which total about 95% of the content of gneissic tonalite are, as shown in Tables 3.2-1 and 3.2-2, plagioclase, biotite, quartz and hornblende.

As shown in Table 4.4-1 these minerals have different values for stiffness and Poisson's ratio. The stresses caused by external forces such as tool indentation during boring are therefore distributed unevenly in the rock. Quartz and hornblende are the stiffest minerals and these accept and transmit higher forces than less-stiff minerals such as plagioclase and biotite. In general, plagioclase grains are stiffer than grains of biotite but the difference is not great and depends to some extent on the source of information used. One major difference between these last two minerals is that the anisotropy of biotite is large since the grains exhibit monoclinic perfect single cleavage and usually appear as clusters of flaky crystals.

Another significant difference is that grains of plagioclase are much harder than biotite grains, as shown in Table 4.4-2 and Figure 4.4-1. Quartz is the

hardest mineral in the composition. It should be kept in mind that hardness is not the same as strength although some degree of correlation does exist. It is a general trend that harder minerals exhibit more brittle behaviour than softer minerals.

Table 4.4-1. The main minerals in the gneissic tonalite and their stiffness parameters.

Mineral	Composition	Average vol.- %	ρ^{**} g/cm^3	υ^{**}	E^{**} GPa	ρ^{***} g/cm^3	υ^{***}	E^{***} GPa
Plagioclase (An53)	Na-Ca-Al silicate	45	2.54	0.3	88.7	2.68	0.30	106.4
Biotite	K-Fe-Mg silicate	26	3.1	0.3	69.7	3.05	0.27	96.2
Quartz	SiO2- β- type	16	2.53	0.2*	99.6	2.53	0.20	179.3
Hornblende	Ca-Fe-Mg silicate	8	3.17	0.3	146.0	3.12	0.29	184.0

E=Young's modulus; υ= Poisson's ratio; ρ=density
* Poisson's ratio 0.08 has been presented for α-type quartz by Landolt&Börnstein 1982 and Zalesski
** Zalesski 1964
*** Landolt&Börnstein 1982

Table 4.4-2. The main minerals in the gneissic tonalite and their hardness parameters.

Mineral	Composition	Average vol.- %	VHN* kg/mm^2	Hardness* M
Plagioclase (An53)	Na-Ca-Al silicate	45	800	6
Biotite	K-Fe-Mg silicate	26	110	2.5
Quartz	SiO2- β-type	16	1060	7
Hornblende	Ca-Fe-Mg silicate	8	600	6

VHN= Vicker's hardness; M= Mohs' hardness
* Salminen&Viitala 1985
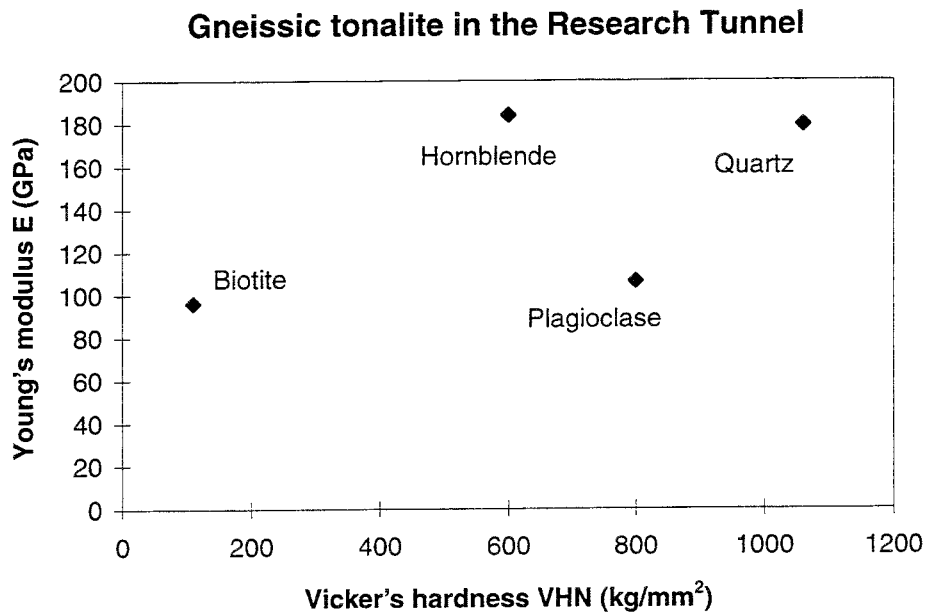
Figure 4.4-1. Values for hardness and Young's modulus of the main minerals in the gneissic tonalite.

As shown in Table 4.4-3 and Figure 4.4-2 the velocity of compression waves is clearly higher in hornblende, quartz and plagioclase than in biotite and the same is true of the velocity of shear waves. The impedance of a mineral directly affects the reflection of stress waves at grain boundaries. Impedance values for biotite and quartz are quite similar but clearly smaller than those for quartz and hornblende. This dynamic mismatch and the difference in the velocity of elastic waves in plagioclase and biotite, the most common minerals in the gneissic tonalite, are clear and may have some effect upon the opening of grain boundaries during stress-wave propagation.

In addition to the properties of the mineral grains, deformation of the grain structure also depends on the degree to which the structure is heterogeneous and the precise nature of the intergranular bonding, which is in turn a function of intergranular porosity, microcracks and flaws in the bonds. When considering deformation of the grain structure in the excavation-disturbed zone, it should be remembered that in this zone, both radial and tangential stress gradients adjacent to the open surface of the hole are high.

Table 4.4-3. The main minerals of the gneissic tonalite and wave velocities and impedance of these.

Mineral	Composition	Average vol.- %	v_c^* m/s	v_s^* m/s	I kg/sm^2
Plagioclase (An$_{53}$)	Na-Ca-Al silicate	45	6600	3540	1.77E+07
Biotite	K-Fe-Mg silicate	26	5350	3000	1.63E+07
Quartz	SiO$_2$-β-type	16	6635	4043	1.68E+07
Hornblende	Ca-Fe-Mg silicate	8	6810	3720	2.12E+07

v_c=velocity of compressive waves; v_s= velocity of shear waves; I= impedance
* Landolt&Börnstein 1982

Gneissic tonalite in the Research Tunnel
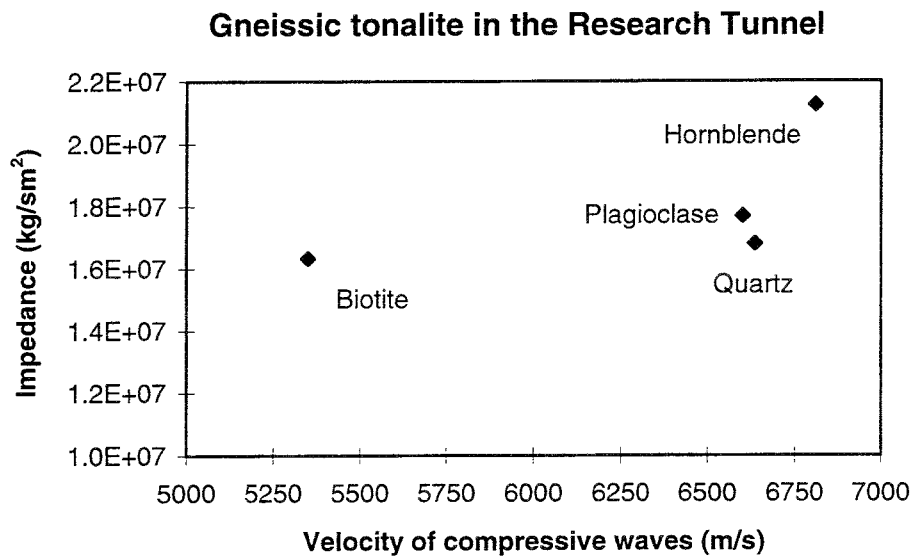
Figure 4.4-2. The velocity of compression waves and impedance of the main minerals in the gneissic tonalite.

4.5 NOTES ABOUT THE THERMAL PROPERTIES OF TONALITE FORMING MINERALS

The thermal properties of the minerals which make up the gneissic tonalite vary. The thermal conductivity of the most common mineral, plagioclase, is 1.68-2.34 $Wm^{-1}K^{-1}$ and is low compared to the anisotropic value for quartz, 6.15-11.3 $Wm^{-1}K^{-1}$. The thermal conductivity of biotite is highly anisotropic with a wide range of values, 0.52-3.14. The thermal conductivity of hornblende, 2.81-2.91 $Wm^{-1}K^{-1}$, is between that of quartz and plagioclase (Kukkonen & Lindberg 1995). A summary of these values is given in Table 4.5-1.

Although the thermal properties of the rock do not play any significant role in the production of excavation disturbance during boring, they have affected the formation and deformation of the rock microstructure under changing thermal conditions and during consolidation of the magma. Crystallization of the magma begins at temperatures above 1400 °C and ends at temperatures below 600 °C. Igneous rocks have therefore been subject to great changes in their thermal environment before reaching their present "normal" temperature, which in the Research Tunnel is about 7 °C.

The differences in coefficients of thermal expansion between minerals such as, for example, Quartz and Feldspar (see Table 4.5-1) have evidently, as the process of cooling progressed, created stress concentrations, deformations and internal residual stresses between mineral grain boundaries, this in turn resulting in the formation of intergranular microfracturing. These same processes will also occur during the artificial cooling and heating of rock samples, as shown for example in a study of the permeability of thermally-cracked granite made by Darot et al. in 1992.

Table 4.5-1. Thermal conductivities and coefficients of expansion for the main materials in the gneissic tonalite.

Mineral	Composition	Average vol.- %	Thermal conductivity * $Wm^{-1}K^{-1}$	Expansion coef. ** $10^{-5o}C^{-1}$	Remarks
Feldspars	Na-Ca-Al silicate	45	2.0-2.5	1-2	
Mica	K-Fe-Mg silicate	26	0.52-3.9	40	Anisotropic
Quartz	SiO_2- β-type	16	6.1-11.3	5	Anisotropic
Hornblende	Ca-Fe-Mg silicate	8	2.81-2.91	-	

*Kukkonen&Lindberg 1995
** Skinner 1966

5 GEOMETRY OF THE LARGE HOLES

5.1 HOLE DIAMETER

The diameter of the large holes was measured (Äikäs 1995) as the minimum peak-to-peak diameter in different directions at intervals of 1 m. The holes were found to be slightly elliptical. The average diameters ranged from 1.527 - 1.528 m, see Table 5.1-1 and variations in the average radii were less than 3 mm. The ratio between the north-south and east-west radii were determined in the large holes at depths of about 0.5 m and 6.5 m. Variations in the ratio of the diameters were small as can seen from Table 5.1-2. The average diameter of the large holes was 0.26% larger than the design diameter i.e. 1524 mm. The minimum diameter measured was identical to the design value.

Table 5.1-1. Diameters and radii of the large holes.

Depth of hole [m]	Hole 1	Hole 2	Hole 3	Average radius	Average diameter
0.5	0.762	0.763	0.766	0.764	1.527
1.0	0.764	0.764	0.764	0.764	1.527
2.0	0.764	0.763	0.764	0.764	1.527
3.0	0.764	0.764	0.764	0.764	1.528
4.0	0.764	0.763	0.765	0.764	1.528
5.0	0.764	0.763	0.764	0.764	1.527
6.0	0.764	0.763	0.764	0.763	1.527
7.0	0.764	0.764	0.764	0.764	1.528
Average radius	0.764	0.763	0.764	0.764	1.527
Average diameter	1.527	1.527	1.528		

Table 5.1-2. Ratio of north-south diameter to east-west diameter.

Depth of hole [m]	Hole 1	Hole 2	Hole 3	Average
0.5	0.998	0.998	0.998	0.998
1.0	0.997	0.998	0.998	0.998
2.0	0.996	0.998	0.998	0.997
3.0	0.998	0.998	0.998	0.998
4.0	0.998	0.998	0.998	0.998
5.0	0.998	0.998	0.998	0.998
6.0	0.998	0.998	0.998	0.998
7.0	0.998	0.998	0.998	0.998
Average	0.998	0.998	0.998	0.998

5.2 STRAIGHTNESS OF THE HOLES

The coordinates of the centerline of each large hole were determined and the straightness and curvature of the holes established by using these (Äikäs 1995). Measurements were carried out at intervals of 1 m.

Deviations in the direction of the large holes, expressed as the horizontal distance between the actual centerline at the bottom of the hole and the true centerline were 32 mm, 27 mm and 17 mm for large holes 1, 2 and 3 accordingly. This is equivalent to a deviation of some 0.2-0.4% of the total hole length as can be seen in Figure 5.2-1 and Table 5.2-1. Large holes 1 and 2 were inclined in a northwest direction and large hole 3 was inclined towards the southwest.

The large holes were slightly curved as shown by Figures 5.2-1 and 5.2-2. The bottom section of Large hole 1, which was bored without a guiding pilot hole, shows greater curvature at that level. Large hole 2 is evenly curved and Large hole 3 is curved in its upper part but fairly straight in the lower part.
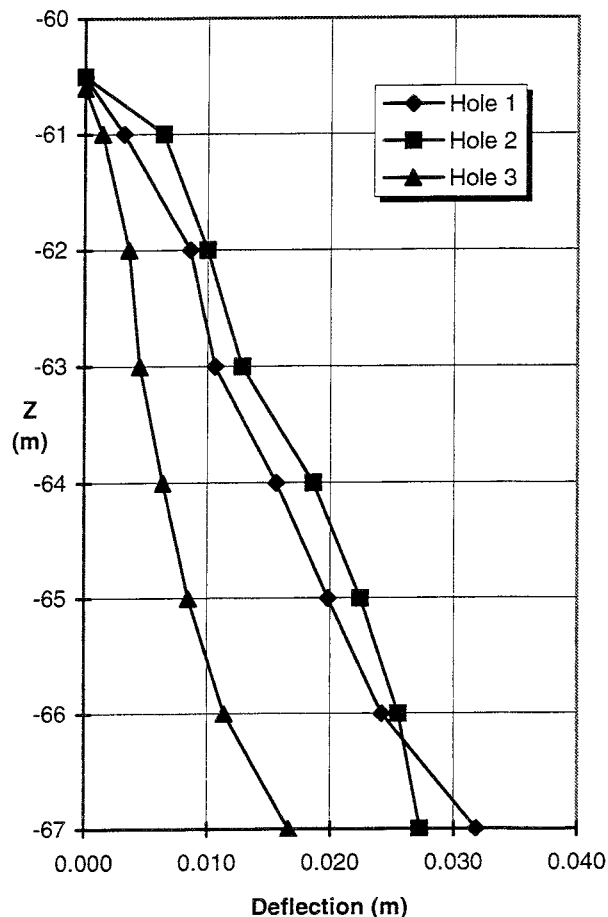
Figure 5.2-1. Deviation of the centerlines of the large holes at depths between the -60.5 and -67.0 levels (vertical section). The concrete floor of the tunnel is at the -60.0 level.

Calculated from the measured deflection the average radius of curvature of the centerline of the large holes was 960 m. This calculation was based on the simplifying assumption that the curvature of the large holes is circular.

The deviations which occur in the upper sections of the large holes are assumed to be primarily the result of misalignment of the drill string at the beginning of boring.

Table 5.2-1. Deviation of the large holes expressed as the horizontal distance between the actual centerline at the bottom of the hole and the true centerline.

Large hole	Direction	Deviation
1	316°	32 mm
2	298°	27 mm
3	237°	17 mm
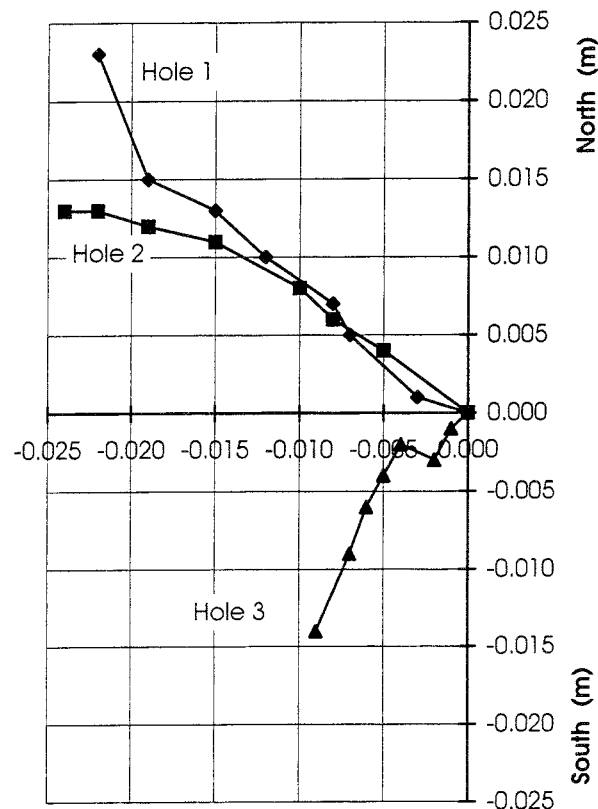
Figure 5.2-2. The deviation of the large holes between the -60.5 and the -67.0 levels projected on a horizontal plane. The concrete floor of the tunnel is at the -60.0 level.

6 SURFACE ROUGHNESS

6.1 METHOD AND RESULTS

The roughness of the surfaces of the three large holes was measured using an optical linear laser profilometer (Halttunen 1995), see Figure 6.1-1. In this method the distance to the rock surface is established by a CCD detector which measures the position of a reflected laser beam, see Figure 6.1-2.

Figure 6.1-1. The optical linear laser profilometer (Halttunen 1995).
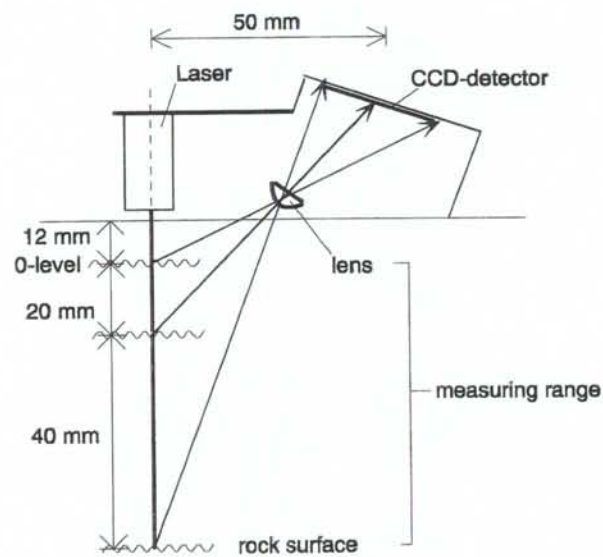
Figure 6.1-2. The principle of measurement used in the laser profilometer.

As the distance to the rock surface in Figure 6.1-2 increases the reflected laser beam moves towards the original outgoing primary beam, allowing the distance to be calculated from differences in the position of the reflected beam. The accuracy of the method depends, among other things, on the size of the laser beam and the properties of the reflecting surface such as wetness and the quantity of reflective cleavage plains in the mineral grains. Details of the technique used and the measurement procedure are given (Halttunen 1995). One example of a measured profile is shown in Figure 6.1-3.

Surface roughness was measured at 0.25 mm intervals along segments 512 mm in length. Surface profiles of the large holes were taken along four vertical lines projected radially towards the main cardinal points from the centerline of each hole. Profile measurements were taken every 500 mm, except for two lines (located in different holes) which were measured every 250 mm, these measurements provided overlapping profiles.

The roughness parameters calculated from measurements of the surface topography were: R_a and R_z (ISO), which quantify differences in height; and S_m, which quantifies differences between the spacings of peaks along the profile (Figures 6.1-4 and 6.1-5).
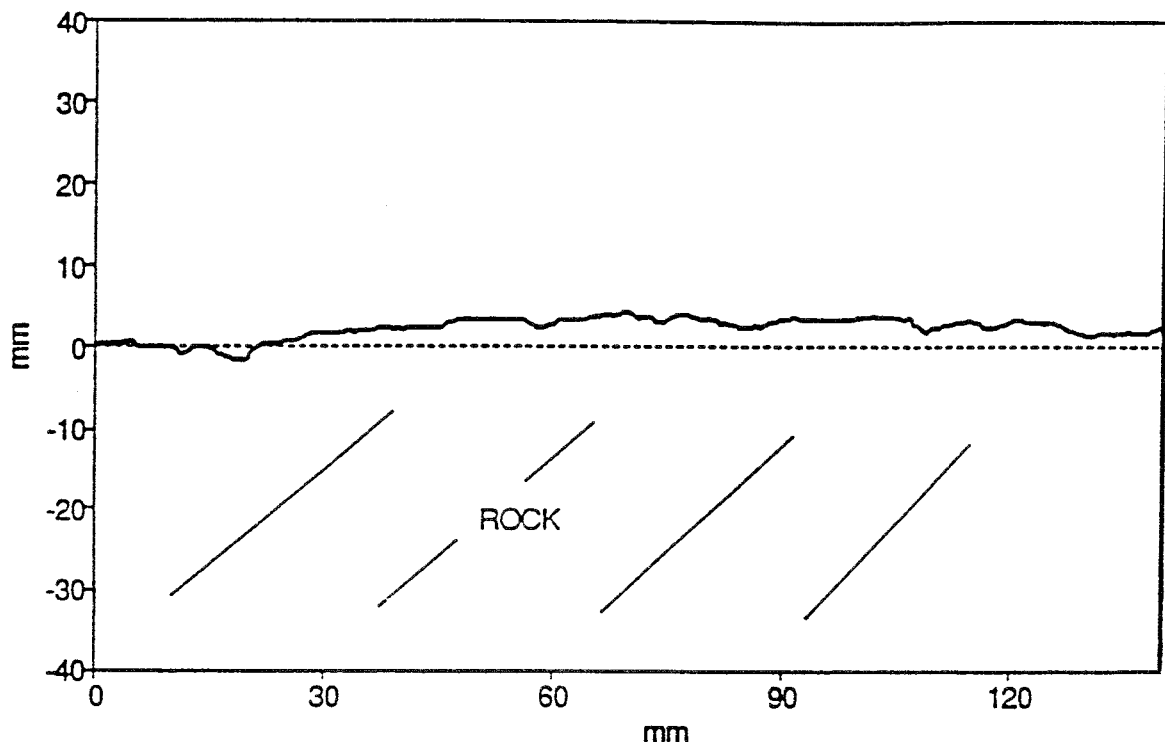
Figure 6.1-3 . *An actual-size example of a section of surface roughness profile. The mean line shown dotted is the average height for the 512 mm long profile section (Halttunen 1995).*
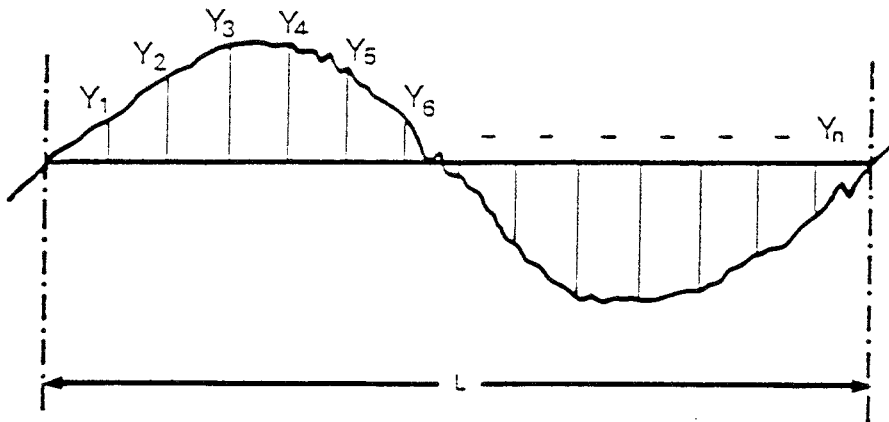
$$R_a = \frac{|y_1| + |y_2| \mathrm{K} \, |y_n|}{n}$$

Figure 6.1-4. Definition of R_a (Dagnall 1986).
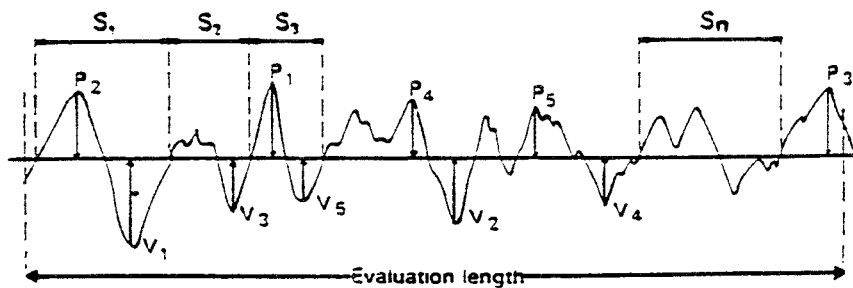
$$R_z(ISO) = \frac{(p_1 + p_2 + p_3 + p_4 + p_5) + (v_1 + v_2 + v_3 + v_4 + v_5)}{5}$$

$$S_m = \frac{s_1 + s_2 + s_3 + s_4 + \ldots + s_n}{n}$$

Figure 6.1-5. Definitions of R_z and S_m (Dagnall 1986).

Values of R_a varied between 0.25 mm and 2.37 mm (the average for all the profiles measured was 0.56 mm) and values of R_z varied between 1.63 mm and 9.38 mm (average value 2.74 mm). Values of S_m ranged from 3.46 mm to 49.60 mm (average value 8.71 mm) (Halttunen 1995).

In addition, two R_q parameters (root mean square of the amplitude), determined from the filtered profiles were calculated. These so called "mega" and "macro" roughness values were obtained from two filtered profiles. The macro value is found by eliminating wavelengths smaller than 0.5 mm and greater than 50 mm from the measured profiles. The corresponding filters used to obtain the mega values were 50 mm and 500 mm (Halttunen 1995). The mega values varied between 0.18 mm and 2.65 mm (the average mega value was 0.62 mm) and the macro values varied between 0.15 mm and 1.50 mm (the average macro value was 0.37 mm).

6.2 ANALYSIS OF RESULTS

The average values for the roughness parameters obtained from the different holes did not differ significantly, as can be seen in Table 6.2-1. Distinct variations were however found in the amplitude parameters of holes in relation to hole depth, as can be seen in Figure 6.2-1. The most distinct variations were found in the R_z parameter although consistent variations also occurred in the parameters for R_a and mega roughness. Most of the culmination points in the roughness parameter curves corresponded to points at which where the boring machine had been stopped to extend the drill string. This operation required that boring was stopped, thrust on the cutter head released, and the cutter head lifted slightly to allow a new drill pipe to be installed.

The amplitude distribution of the roughness profiles was calculated and found to be normal. Examples are shown in Figures 6.2-2 and 6.2-3 together with a normal distribution curve. It can be seen that the distributions are very close to normal even though the profiles exhibiting abnormal roughness (CSouth10 and CSouth12) are slightly skewed.

Further assessment of the results included the following topics. These are discussed in more detail in the following sections:

- comparison to results obtained by using a mechanical comb profiler

- accuracy of overlapping profiles

- analysis of the wavelength spectrum of roughness using FFT (fast Fourier transform) and autocorrelation

- smoothing of the profile with a moving average to reduce noise

- the effect of rock type on surface roughness

- sections of abnormal roughness.
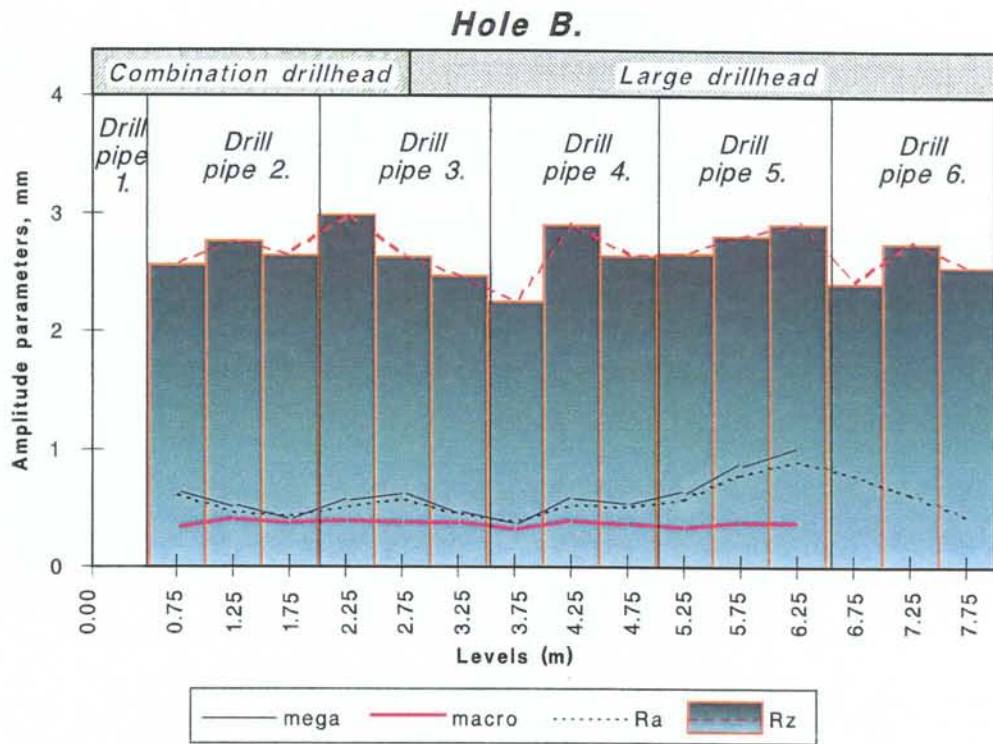
Figure 6.2-1. Amplitude parameter values at different levels in Large hole 2. These values are averages of four vertical lines.

Table 6.2-1. Average roughness parameters of the holes.

Hole	R_a	R_z	S_m	mega	macro
1, average	0.58	2.84	8.83	0.62	0.36
range	0.34-1.39	2.10-4.00	4.14-46.08	0.31-1.50	0.26-0.53
2, average	0.57	2.72	9.52	0.63	0.38
range	0.25-1.53	1.63-4.93	4.08-33.93	0.18-1.74	0.23-0.88
3, average	0.52	2.65	7.78	0.61	0.37
range	0.30-1.32	1.67-9.38	4.31-26.50	0.27-1.94	0.15-1.50
Total average	0.56	2.74	8.71	0.62	0.37
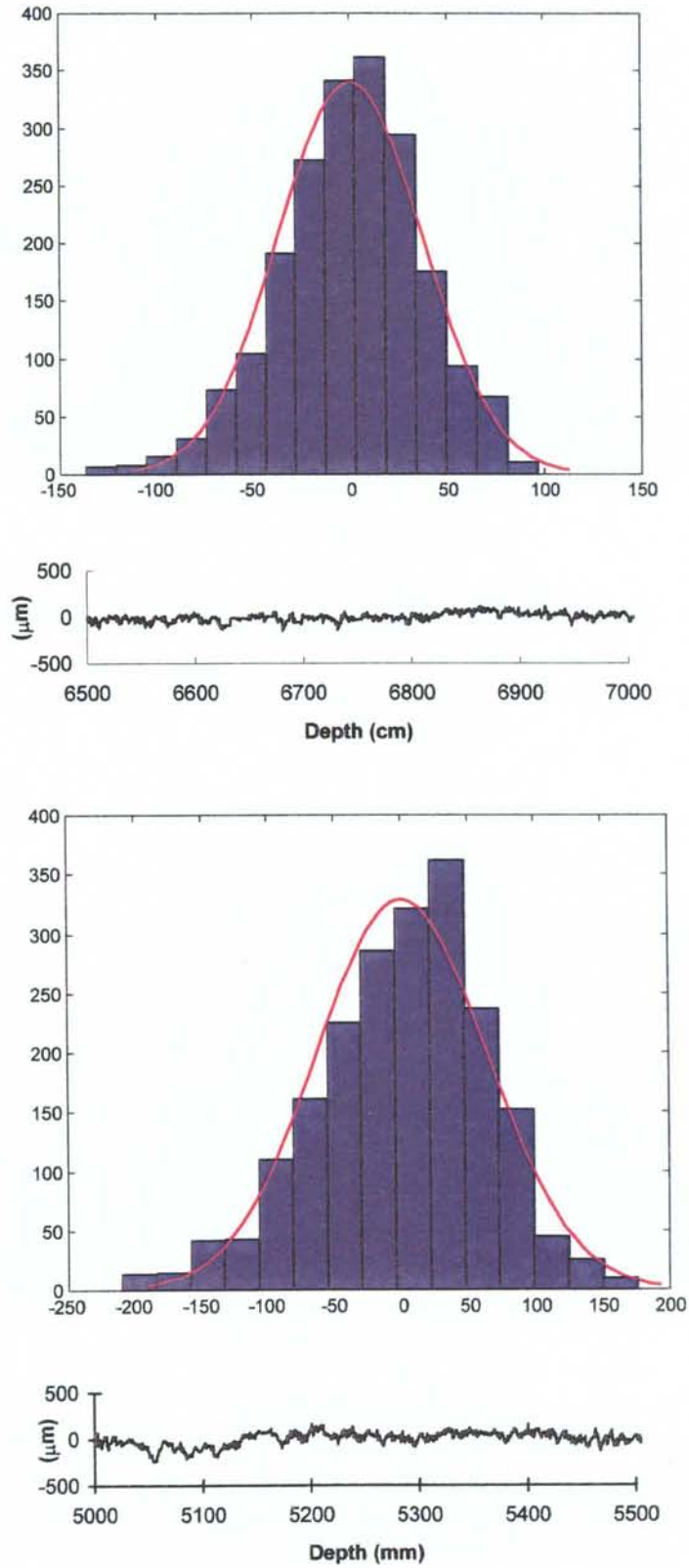
Figure 6.2-2. *Distribution of values for profile height shown fitted to a normal distribution curve. Profiles CNorth25 (top) and CSouth10 (bottom). The profiles have been linearly detrended with respect to the mean line.*
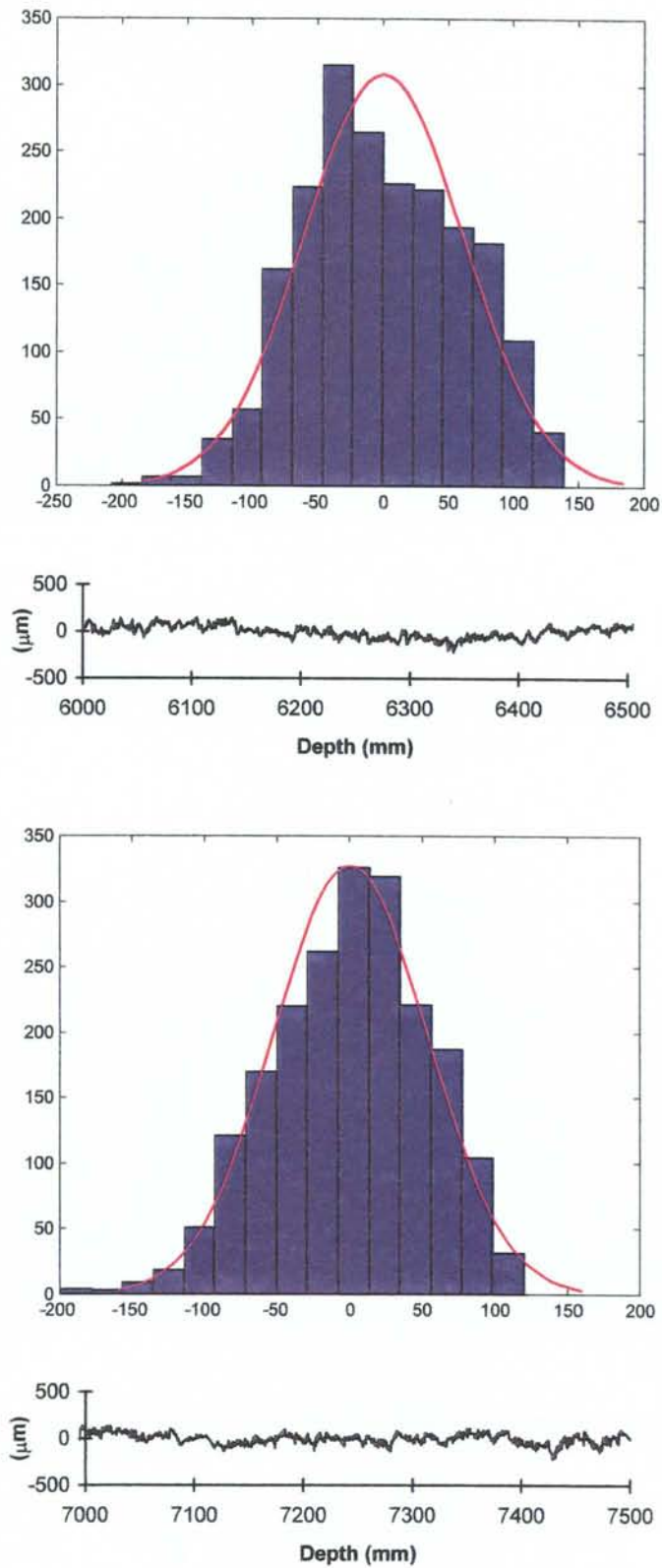
***Figure* 6.2-3.** *Distribution of values for profile height shown fitted to a normal distribution curve. Profiles CSouth12 (top) and CSouth14R (bottom). The profiles have been linearly detrended with respect to the mean line.*

6.2.1 Comparison with results obtained by using a mechanical comb profiler

The accuracy of the profiles obtained was studied by comparing the results from the linear laser profiler with results obtained from the same section with a mechanical comb profiler. In addition, a visual comparison with the exposed rock surface was also made.

The comb profiler employed was of type TEMU 367 made by Teräs-LVI Oy AB, see Figure 6.2-4. The width of the profile measured by the comb profiler was 200 mm and the diameter of the round-sectioned teeth in the comb was 1 mm.

The profiles shown in Figure 6.2-5 demonstrate that profile measurement using the laser profilometer is much more accurate, even though the same primary trends can be seen in both profiles. The measurement provided by the laser profilometer is a strongly center-weighted average of the area covered by the elliptical laser spot, the axis of which is 1 mm along the profile and 5 mm perpendicular to the profile.

When comparing the profiles obtained to a visual assessment of the rock surface it was found that filtering of the laser profile by use of a moving average smoothed out some of the very short wavelength roughness and yielded a result which corresponded well to a visual assessment of the profile, while providing significantly higher accuracy than the result obtained with the comb profiler. Wavelengths shorter than two millimeters are completely missing from the profile measured with the mechanical profiler which is consistent with the 1 mm diameter of the comb teeth. The result obtained with the comb profiler is in fact close to a 9-point moving average of values obtained from the laser profilometer.
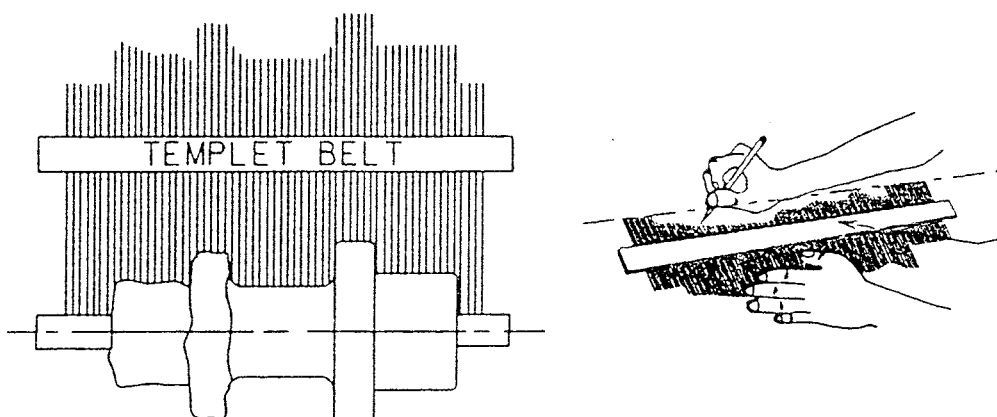
Figure 6.2-4. The comb profiler.
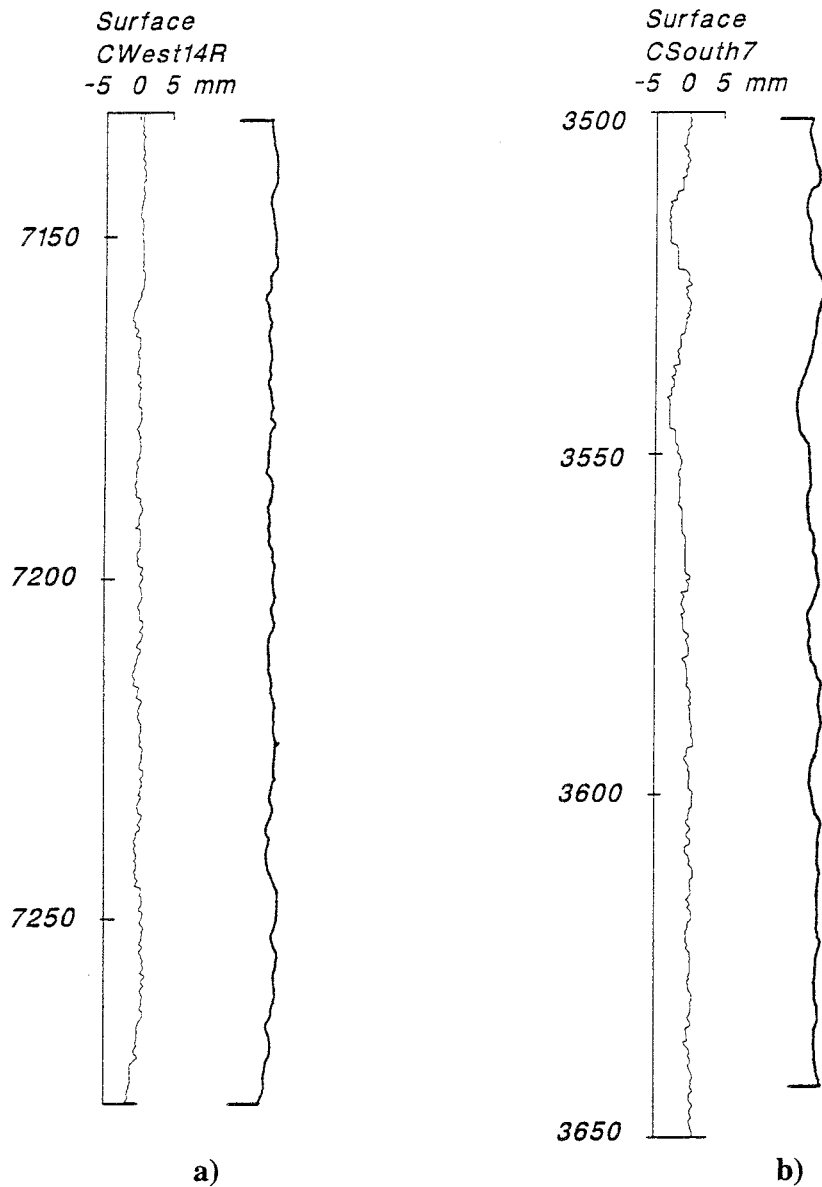
Figure 6.2-5. Profiles a) *CWest14R* and b) *CSouth7 measured with both a mechanical profiler and the laser profilometer. The laser profile is on the left, the mechanical profile is on the right.*

6.2.2 Accuracy of overlapping profiles

The measurement of surface profiles included a series of repetitive measurements taken without moving the measuring device. It was found that the average difference between repeated measurements of the surface height for individual points was 0.15 mm, which was also considered to be the accuracy of the measuring device (Halttunen 1995).

Profiles obtained with the laser profilometer were also compared to corresponding overlapping profiles, see Figures 6.2-6 and 6.2-7. The results show that because of the accuracy of the laser profilometer and the three-dimensional nature of surface roughness, a profile must be measured at

exactly the same location to achieve a reproducible result. In spite of this there are plenty of amplitude features less than 0.1 mm in size which can be recognized in both of the overlapping profiles.
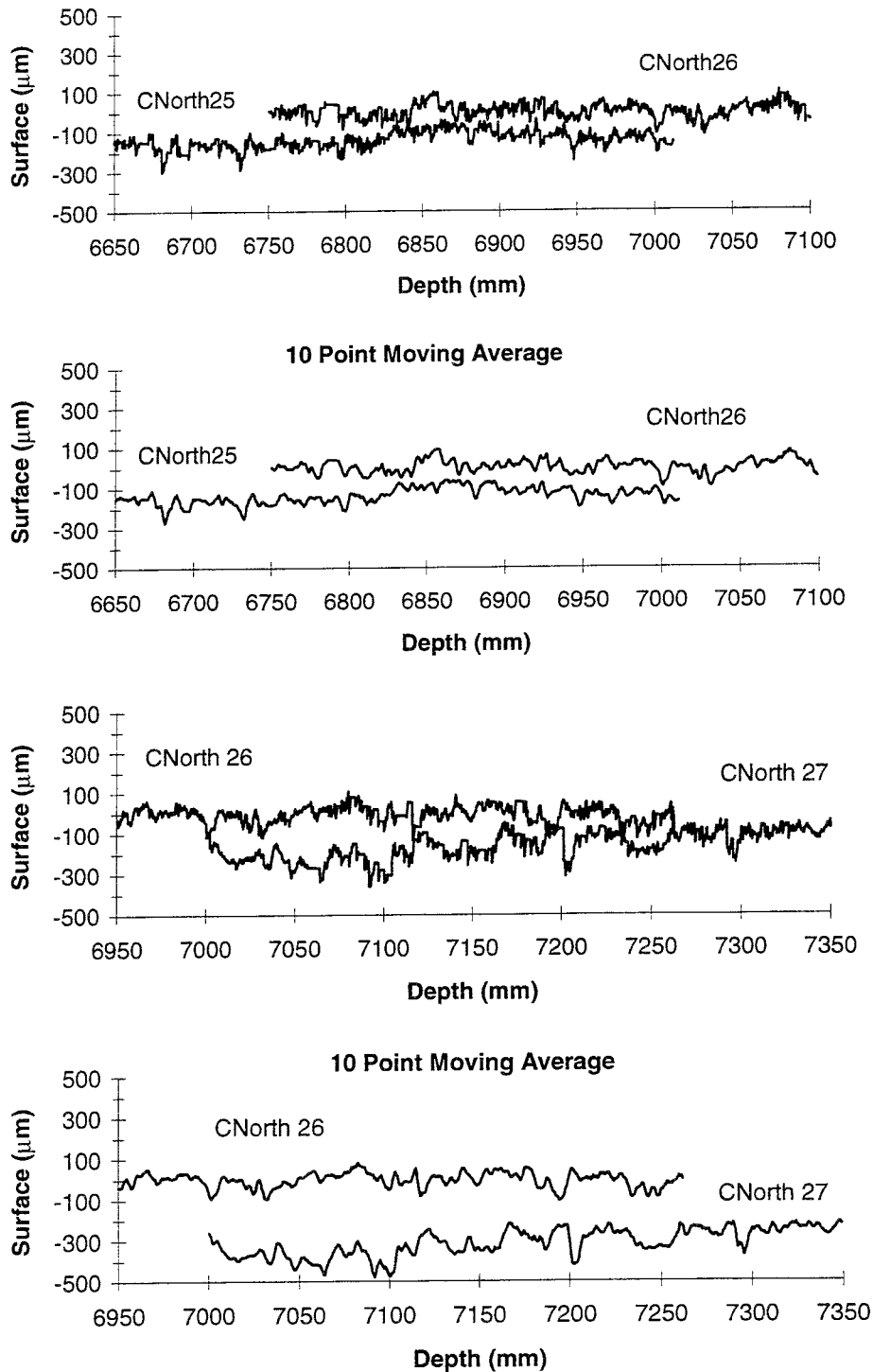
Figure 6.2-6. Two sections of overlapping profiles shown with and without smoothing by a 10-point moving average. The mean level of the overlapping profiles has been changed to make it easier to visualize the difference in shape. The differences are caused by variations of a few millimeters in the positions of the overlapping profiles.

BNORTH19-BNORTH24
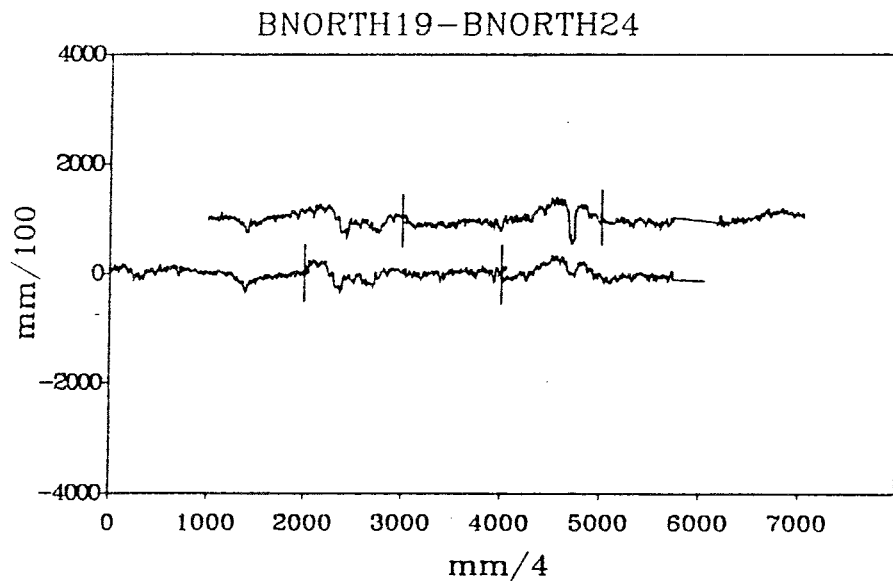
Figure 6.2-7. Two sections of overlapping profiles (Halttunen 1995). One section consists of three different profiles in series.

6.2.3 **Analysis of the surface roughness wavelength spectrum using FFT (Fast Fourier Transform) and autocorrelation**

Surface roughness profiles in the large holes are obviously composed of different wavelengths. Analysis of selected profiles were carried out using Fast Fourier Transform (FFT) to obtain an estimate of the frequency spectra they contained. The profiles were linearly detrended before carrying out the analysis. Each entire profile was then analyzed using Welch's method and unbiased scaling for the power spectral density (psd) computation. The FFT analysis was carried out using different size windows, with overlapping windows, and the whole profile was also analyzed without windowing. The result of each analysis was presented in a periodogram which gives the power spectrum in dB units with respect to wavelength frequency. In the periodograms obtained by this analysis, sampling frequency presented in Hz units (i.e. samples/second) was modified and actually represents sampling length (i.e. samples/unit length of 1 mm).

A total of 14 surface roughness profiles representing different parts of the large holes and different types of sections were analyzed. The profiles studied were CNorth5, CEast3, CSouth3, CSouth10, CSouth11, CSouth12, CSouth13, CSouth14R, CSouth15R, CNorth27R, CEast14R, CNorth21, BWest2 ans BWest2.

The effect of window size and overlapping on the power spectral density for the CSouth3 profile shown in Figure 6.2-8 can be seen in Figure 6.2-9. The window sizes used were 256, 512, 1024 and 2048 data points, corresponding to profiles of length 64 mm, 128 mm, 256 mm and 512 mm. The overlap between neighbouring windows was 64 points, corresponding to a profile length of 16 mm. The advantage of using a windowed calculation can be seen in Figure 6.2-9. The summation of the windowed results reduces noise and therefore the shape of the spectrum becomes smoother while still retaining the general trends - except for the longer wavelengths seen in other spectrums calculated by using larger windows.

All the periodograms calculated show a similar power spectral density to that shown in Figure 6.2-9. There are no clear peaks, showing that the distribution of frequencies is even across the frequency range which ends at the maximum frequency value of 2 Hz, half the sampling frequency, corresponding to a wavelength of 0.5 mm. The highest peak in the profiles is seen at a frequency of 0.02 Hz which corresponds to a wavelength of 5 cm. This is caused by the 256 point window size, corresponding to a length of 64 mm. Visual observations suggest that the surface roughness profile contains long wavelength components (i.e. wavelength greater than 1 m), but these appear to be sparse, cannot be generalized and are probably distributed in an uneven fashion.

Autocorrelation analysis of the CSouth10, CSouth11, CSouth12, CSouth13 and CSouth14R profiles shown in Figures 6.2-10 and 6.2-11 was carried out and the resultant autocorrelation diagrams are shown in Figures 6.2-12 and 6.2-13. Autocorrelation of the profiles was carried out as a special case of cross-correlation. Before correlating, the profiles were linearly detrended and scaling was performed so that the autocorrelation corresponding to a lag of zero was set to one.
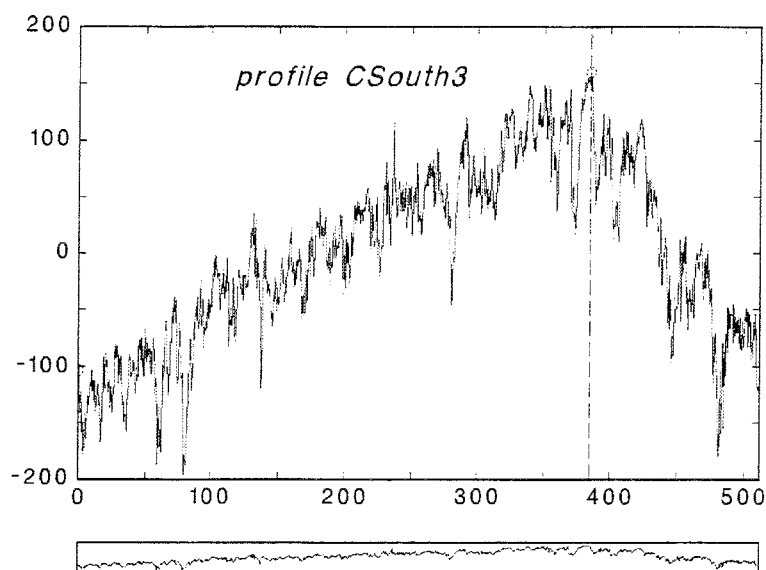
Figure 6.2-8. Surface roughness profile CSouth3.
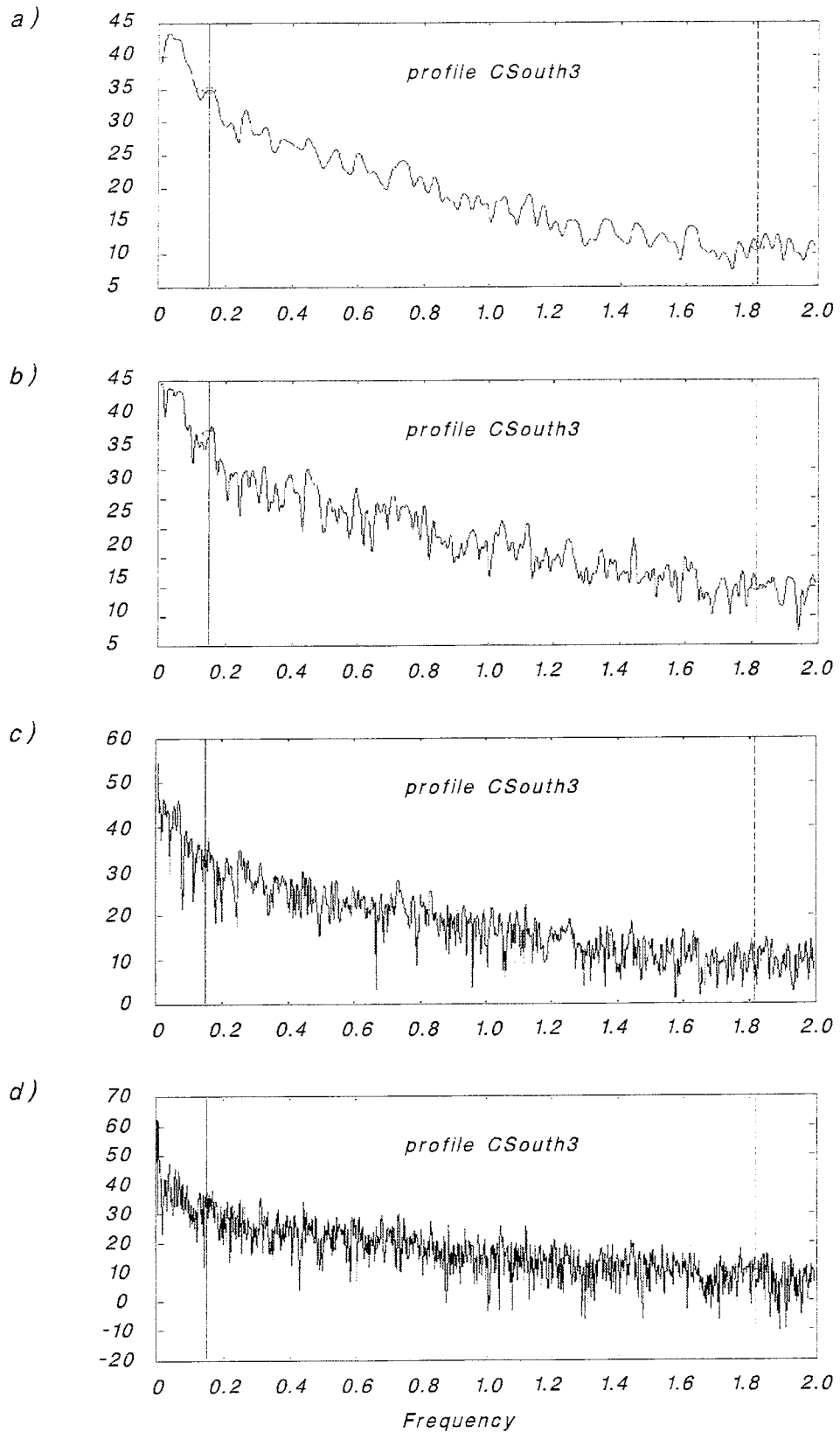
Figure 6.2-9. Power spectrum density periodogram for the profile shown in Figure 6.2-8 (CSouth3). The window sizes used were a) 256, b) 512, c) 1024 and d) 2048 data points, corresponding to profiles of length 64 mm, 128 mm, 256 mm and 512 mm. The overlap used between neighbouring windows was 64 data points (16 mm).
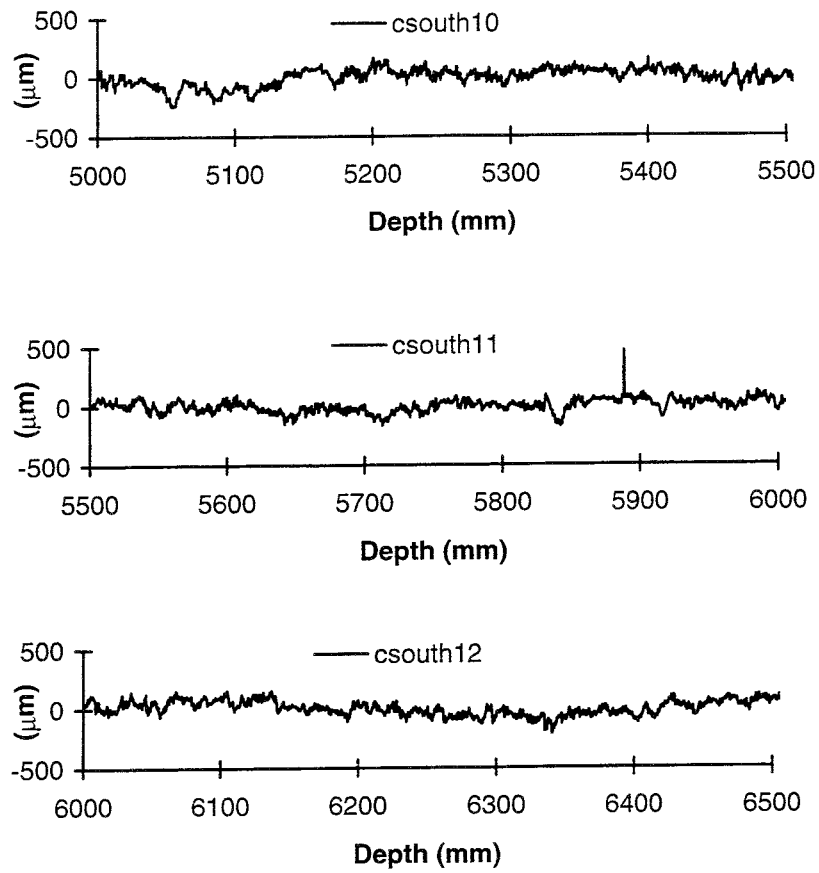
Figure 6.2-10. Surface profiles profiles CSouth10 (top), CSouth11 (middle) and CSouth12 (bottom).
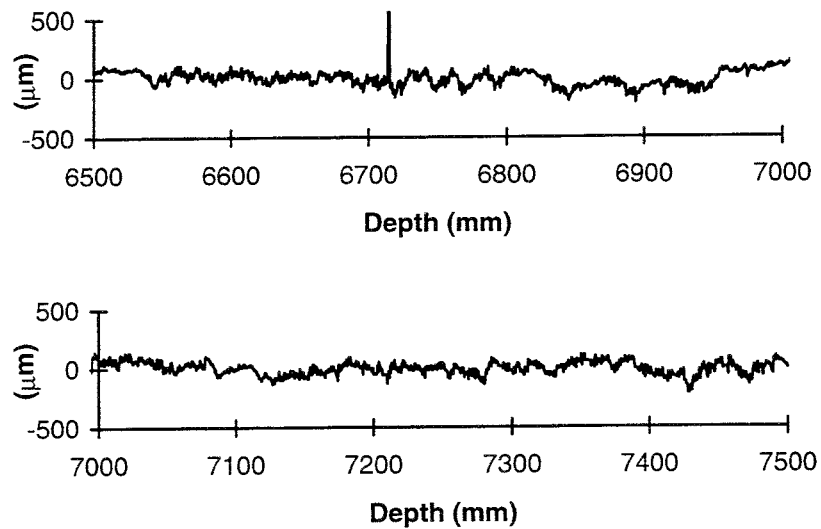
Figure 6.2-11. Surface roughness profiles CSouth13 (top) and CSouth14R (bottom).
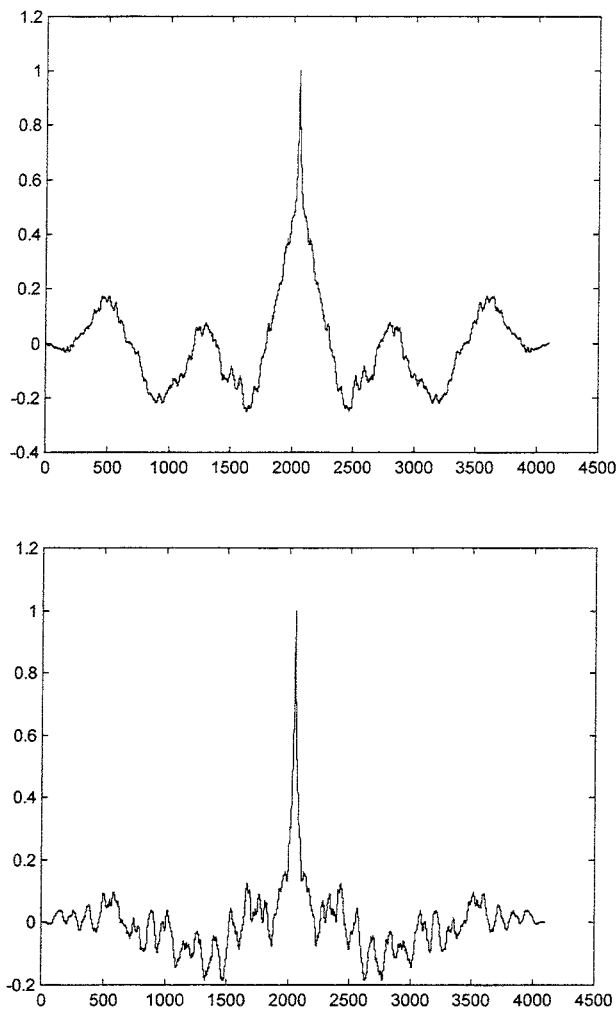
Figure 6.2-12. Scaled autocorrelation of surface roughness profiles CSouth10 (top) and Csouth11(bottom).

The highest degree of correlation is found in the center position where the identical profiles overlap. The edge areas show lower autocorrelation where the number of overlapping datapoints is smaller. It is therefore advantageous to unbias the result by emphasizing the edge areas to provide a more realistic view. As an example of this, unbiased autocorrelations are shown in Figure 6.2-14 for profiles CSouth10 and CSouth13. The general trend in these autocorrelations is similar to that found in the original autocorrelations (Figures 6.2-12 and 6.2-13), but the smaller variations in the edge areas are emphasized.
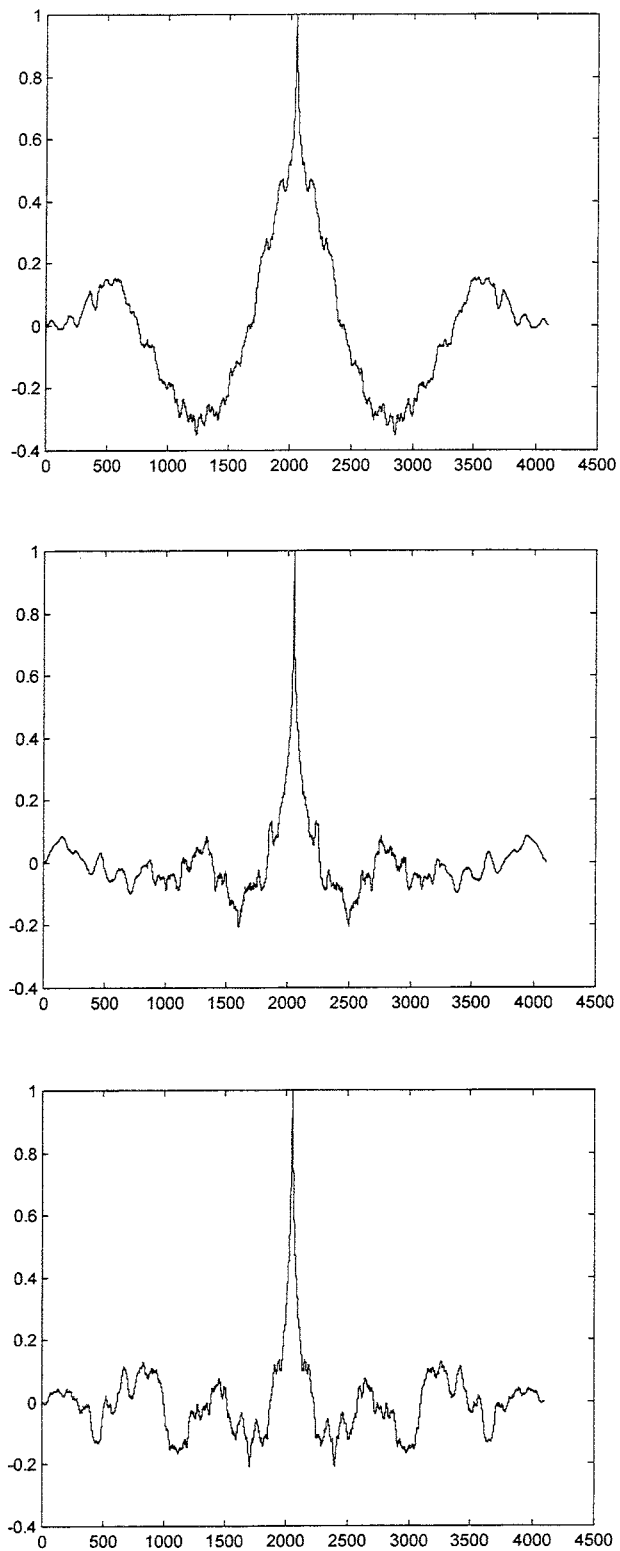
Figure 6.2-13. Scaled autocorrelation of surface roughness profiles CSouth12 (top), Csouth13 (middle) and CSouth14R (Bottom).

This analysis shows that there is periodic correlation between the profiles. In profiles CSouth10 and CSouth14R there is a wavelength periodicity of about 125 mm. In profiles CSouth12 and CSouth11 there is a wavelength periodicity of about 250 mm, double that found in the earlier profiles. There appears to be no significant wavelength periodicity in profile CSouth13. If the autocorrelation is plotted in an unbiased form (Figure 6.2-14), it can however be seen that there appears to be a wavelength periodicity of about 500 mm. This result suggests that some of the larger wavelength components of surface roughness are multiples of 125 mm, being 125, 250 and 500 mm.
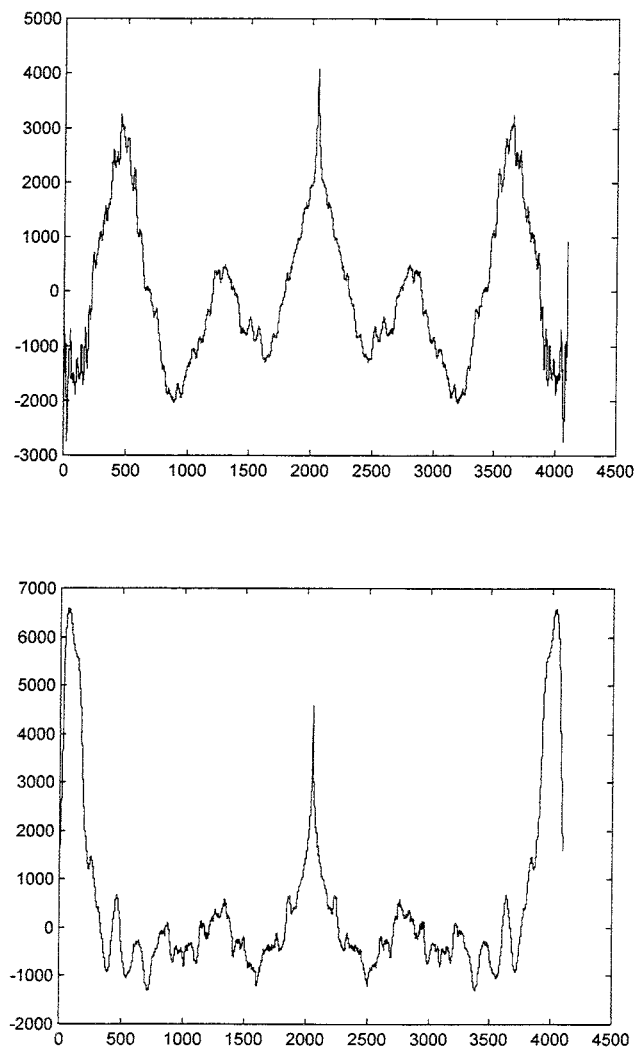
Figure 6.2-14. Examples of unbiased autocorrelation surface roughness profiles for CSouth10 (top) and CSouth13 (Bottom).

6.2.4   **Smoothing of the profile by a moving average to reduce noise**

As mentioned earlier (Section 6.2.2) filtering of the profile obtained from the laser profilometer by using a moving average of 9 points smooths out some of the very short wavelength roughness and yields a result which corresponds well to a visual assessment of the profile. A moving average of four points, as shown in Figure 6.2-15, was found to be effective in removing noise in the profile caused most probably by changes in the reflective properties of the minerals, without smoothing out the actual profile to any significant extent.
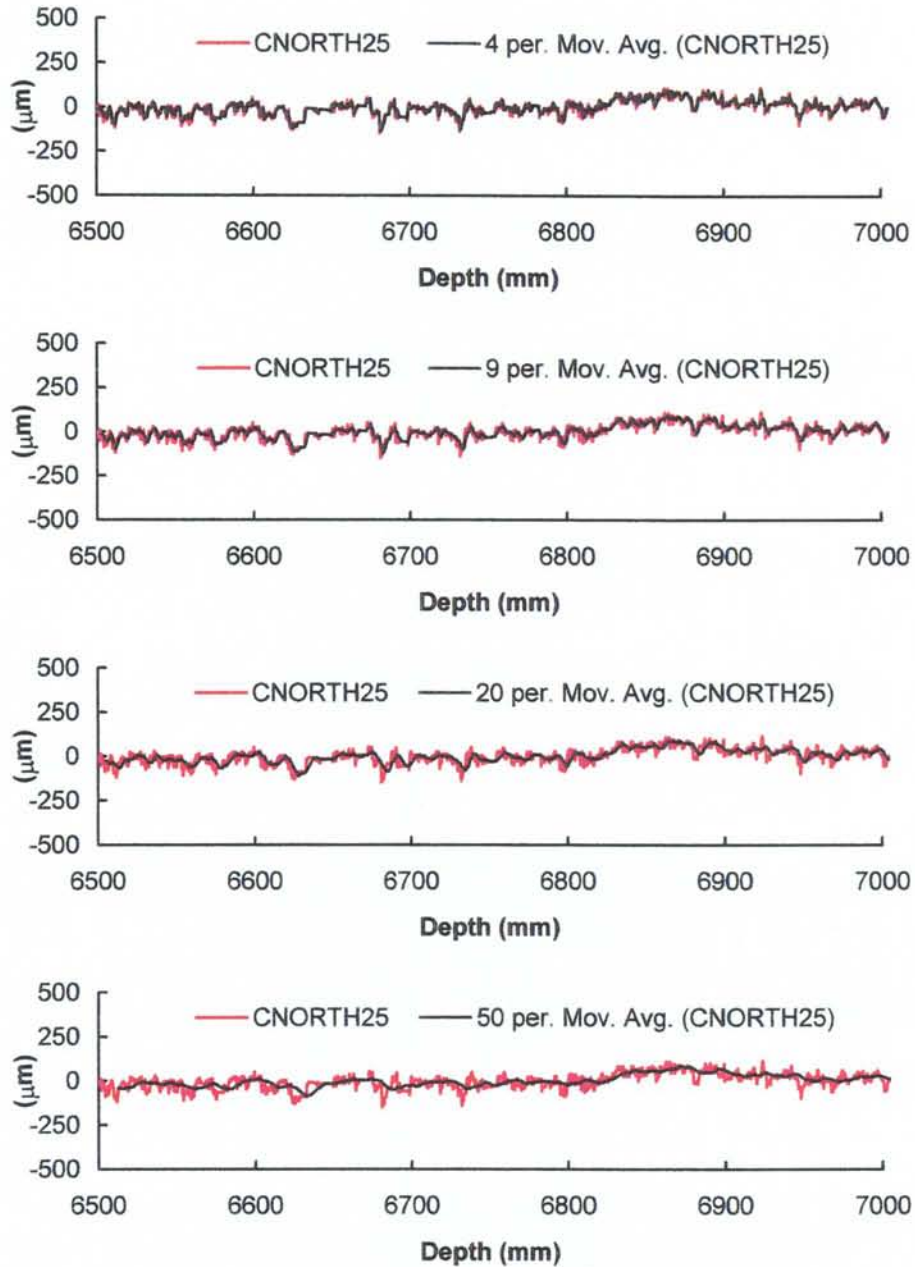
Figure 6.2-15. *A section of profile filtered with a moving average of 4, 9, 20 and 50 measurement points.*

An example of the effect of smoothing by four-point moving average on the power spectrum obtained from profiles CNorth27 and CEast14R (Figure 6.2-16), is shown in Figure 6.2-17. Wavelengths of 1 mm (corresponding to a length of four points) are reduced and a reduction in power spectrum densities can be seen up to a frequency of 0.4 (corresponding to a wavelength of 2.5 mm).
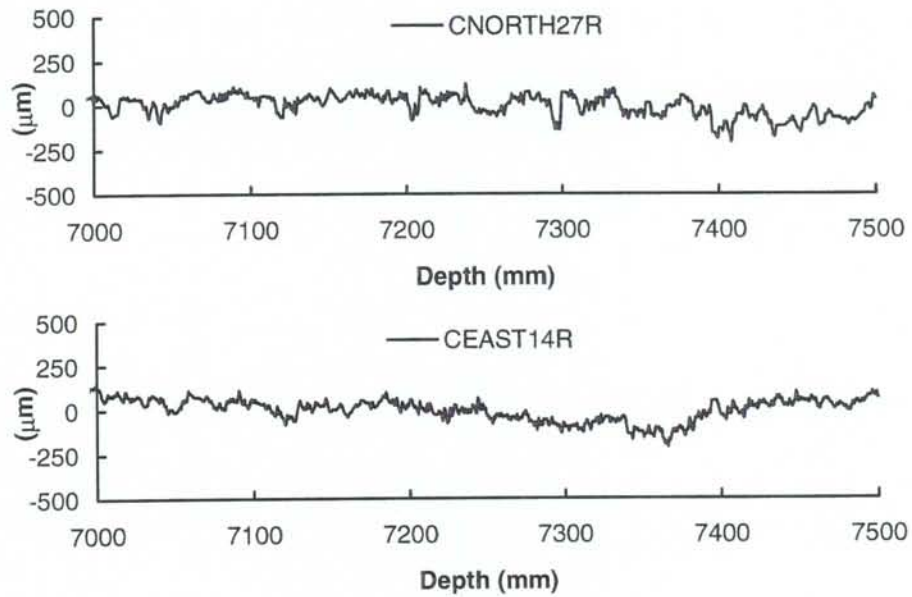
Figure 6.2-16. *Surface roughness profiles CNorth27R (top) and CEast14R (bottom) filtered with a four-point moving average.*
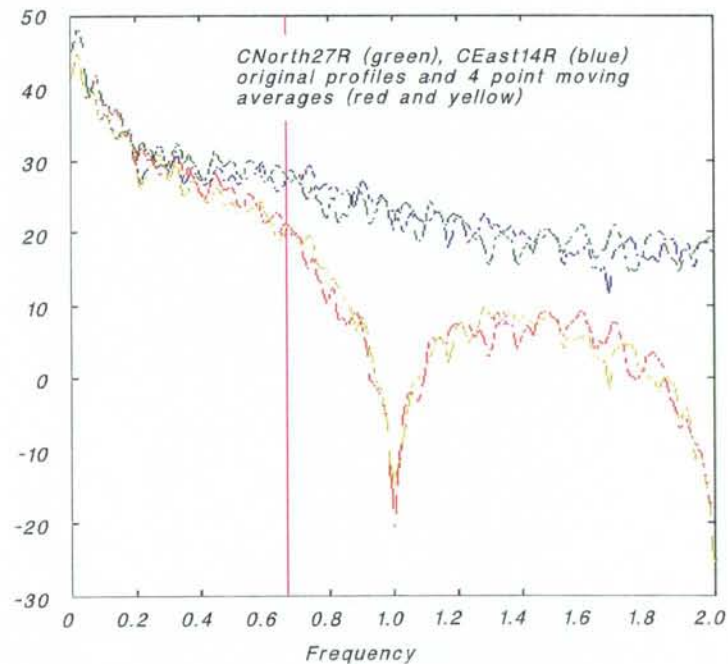
Figure 6.2-17. *Periodogram of profiles CNorth27R and CEast14R with the original data and a four-point moving average.*

6.2.5   **The effect of rock type on surface roughness**

A comparison was made of three corresponding profiles taken at the same depth in the large holes in three different types of rock - pegmatite, homogeneous tonalite and gneissic tonalite (see Figure 6.2-18). Since the depth at which the profiles were taken was the same, the boring parameters were the same and therefore the mineralogy remained the only variable.

According to the periodograms of the profiles shown in Figure 6.2-19 there are no significant differences in the surface roughness even though visual observation suggested that the degree of surface roughness was lower in the homogeneous tonalite and pegmatite. It was concluded that the effect of mineralogy on the degree of surface roughness was not significant.
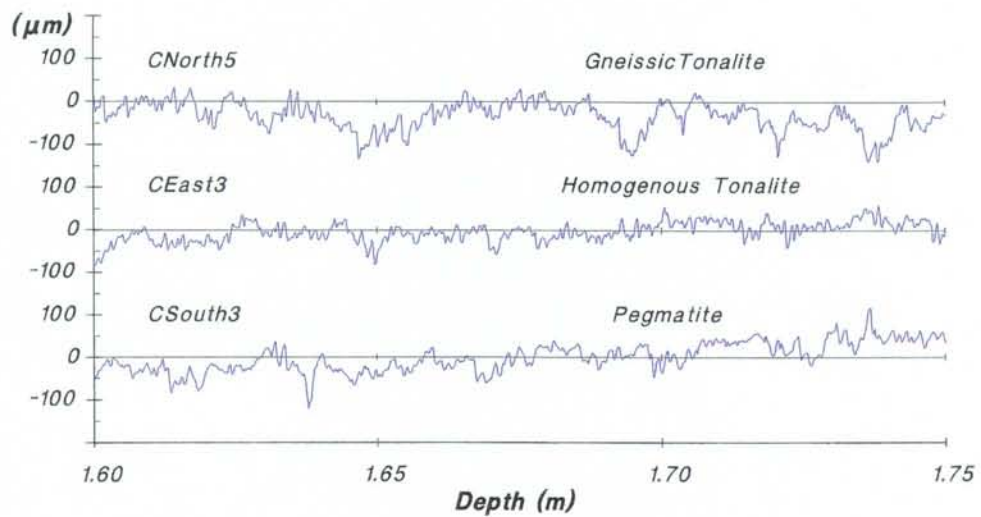
Figure 6.2-18. *Surface roughness profiles for sections of gneissic tonalite, homogeneous tonalite and pegmatite.*
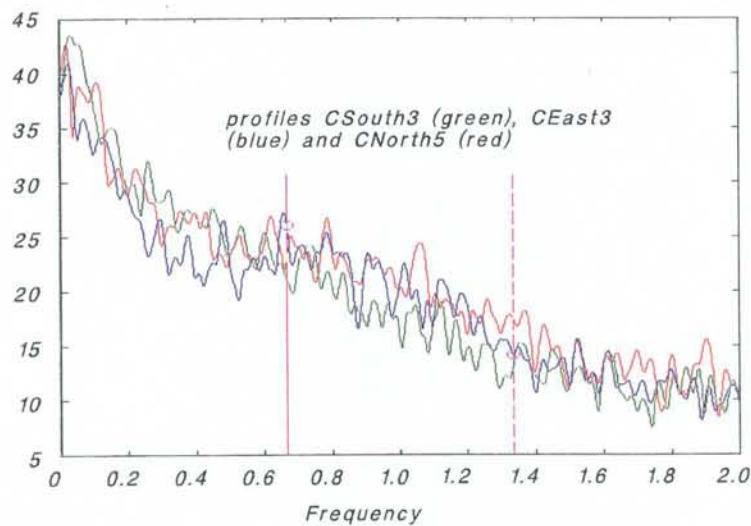
Figure 6.2-19. *Periodograms of surface profiles for the sections of gneissic tonalite, homogeneous tonalite and pegmatite shown in Figure 6.2-18.*

6.2.6 Sections of abnormal roughness

Although the surfaces of the large holes were generally quite smooth a few distinct anomalous sections exhibited a high degree of surface roughness. It was noted that the degree of surface roughness was different in sections where the gauge rollers had contacted the rock surface. There were also sections where only the cutters had touched the surface and made deeper grooves, these showed the indentations of single cutter buttons on the points where contact had been made.

Surface profiles CNorth27R and CEast14R, shown earlier in Figure 6.2-16, represent the same section at depth from 7.0 to 7.5 m in the large hole 3 but towards different directions. Surface profile CNorth27R represents a section where the gauge rollers have been in continuous contact with rock whereas CEast14R represent a section where the gauge rollers had not contacted the rock surface. The periodograms of these two profiles were compared to find out if there is difference in the frequency spectra, which could be usefull in discriminating the sections where the gauge rollers have been in contact with rock. There appeared to be no significant differences between the corresponding periodograms (Figure 6.2-20).

Indentation by the gauge rollers can be clearly seen in profiles CNorth21, BWest2 and BWest3. The surface roughness profile of the contact section in these last two profiles is shown in Figure 6.2-21. The periodogram derived from the profiles (Figure 6.2-22) shows a peak which could corresponds to the wavelength of 66 mm between the peaks which can be seen in the surface profile and the corresponding frequency of 0.015 Hz.
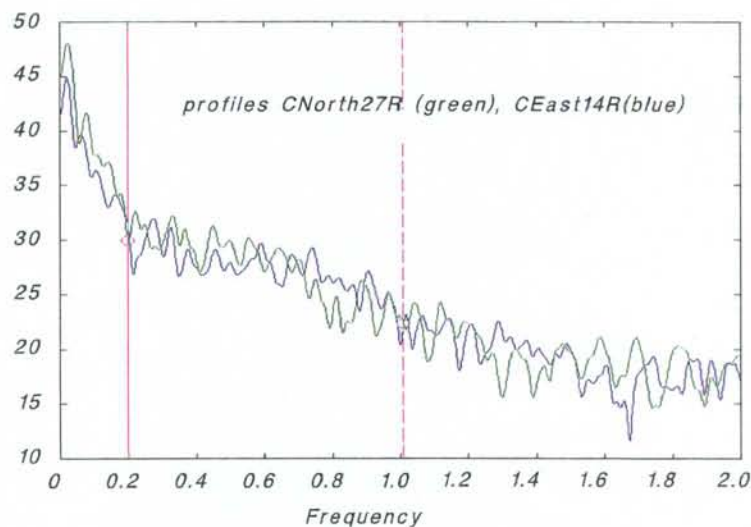
Figure 6.2-20. *Periodograms of surface roughness profiles CNorth27R and CEast14R. The periodograms are in principle the same as those in Figure 6.2-17 (original profiles) but shown on a different scale.*

Although the power spectrum density analysis of the profiles which included indentation kerfs caused by gauge rollers did not provide as much information as expected the method could perhaps be developed to a significant extent by focusing the analysis of data on the long wavelength end of the periodograms.

Anomalous changes in surface roughness can also be seen for example in the upper part of surface roughness profile CSouth10 (Figure 6.2-23). Cross-correlation was carried out between the section exhibiting abnormal roughness in profile CSouth10 (Figure 6.2.-23) and the neighbouring profiles shown in Figures 6.2-26 and 6.2-27.

The cross-correlation highlights areas in which the surface roughness is similar to that in the sample section, which was in this case one section of the CSouth10 profile. As expected, cross-correlation to profile CSouth10 gave the high peak seen in Figure 6.2-24 which corresponds to the location of the sample section. A similar cross-correlation peak was found in profile CSouth14R where a similar type of roughness feature is evident. In other profiles there are several correlation peaks but none are as distinct as in the earlier mentioned profiles CSouth10 and CSouth14R. The cross-correlation diagrams show a distinct periodicity with different wavelengths. Clear peaks correspond to wavelengths in the range 50 to 70 mm. The periodicity found in all the cross-correlation diagrams suggest that the roughness found in the sample section is a typical component of the surface roughness structure.
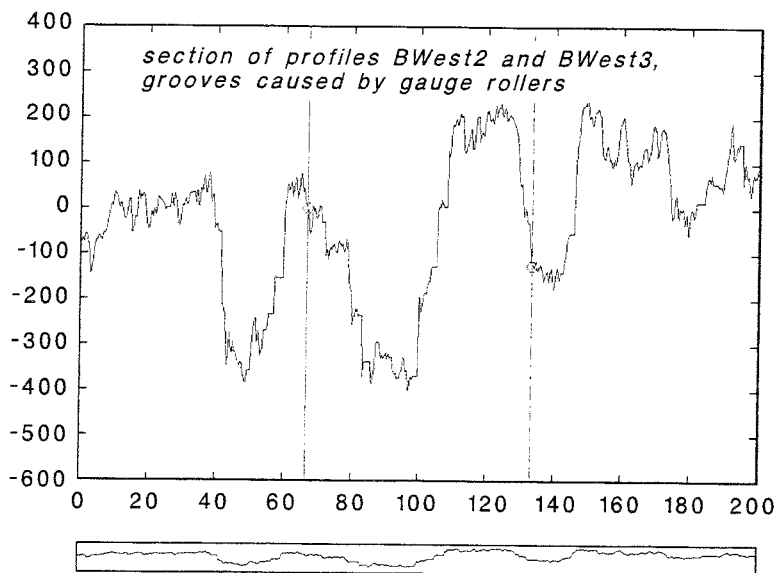
Figure 6.2-21. Sections where the gauge rollers contacted the rock surface in surface roughness profiles BWest2 and BWest 3.
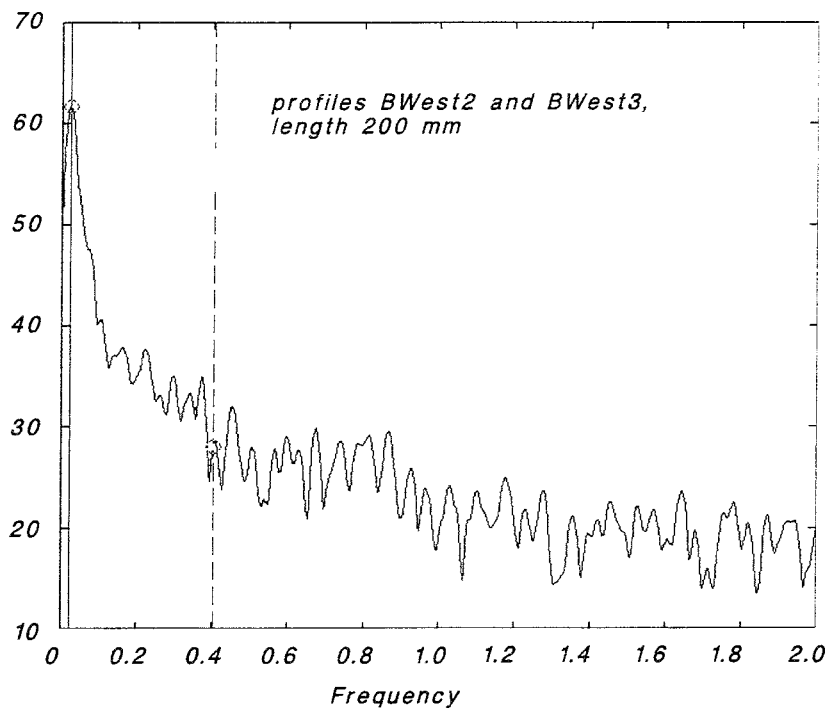
Figure 6.2-22. Periodogram derived from the sections where the gauge rollers contacted the rock surface in surface roughness profiles BWest2 and BWest3.
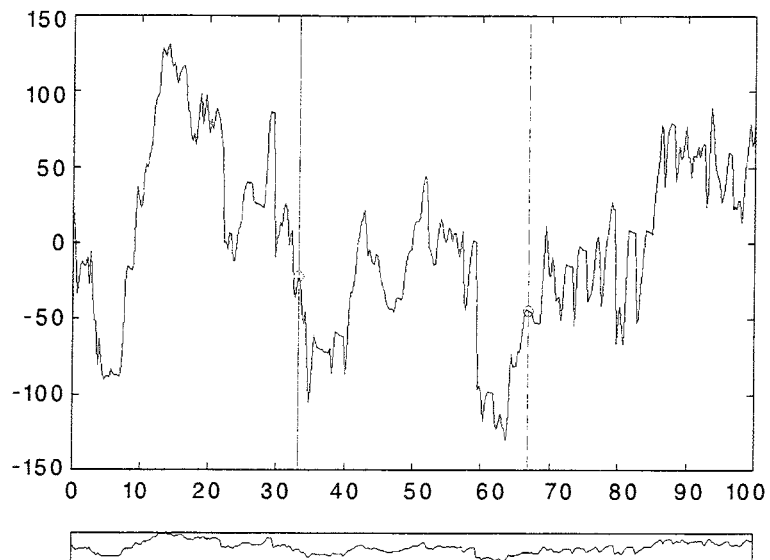
Figure 6.2-23. Surface roughness profile showing a distinct anomaly in surface roughness (CSouth10).
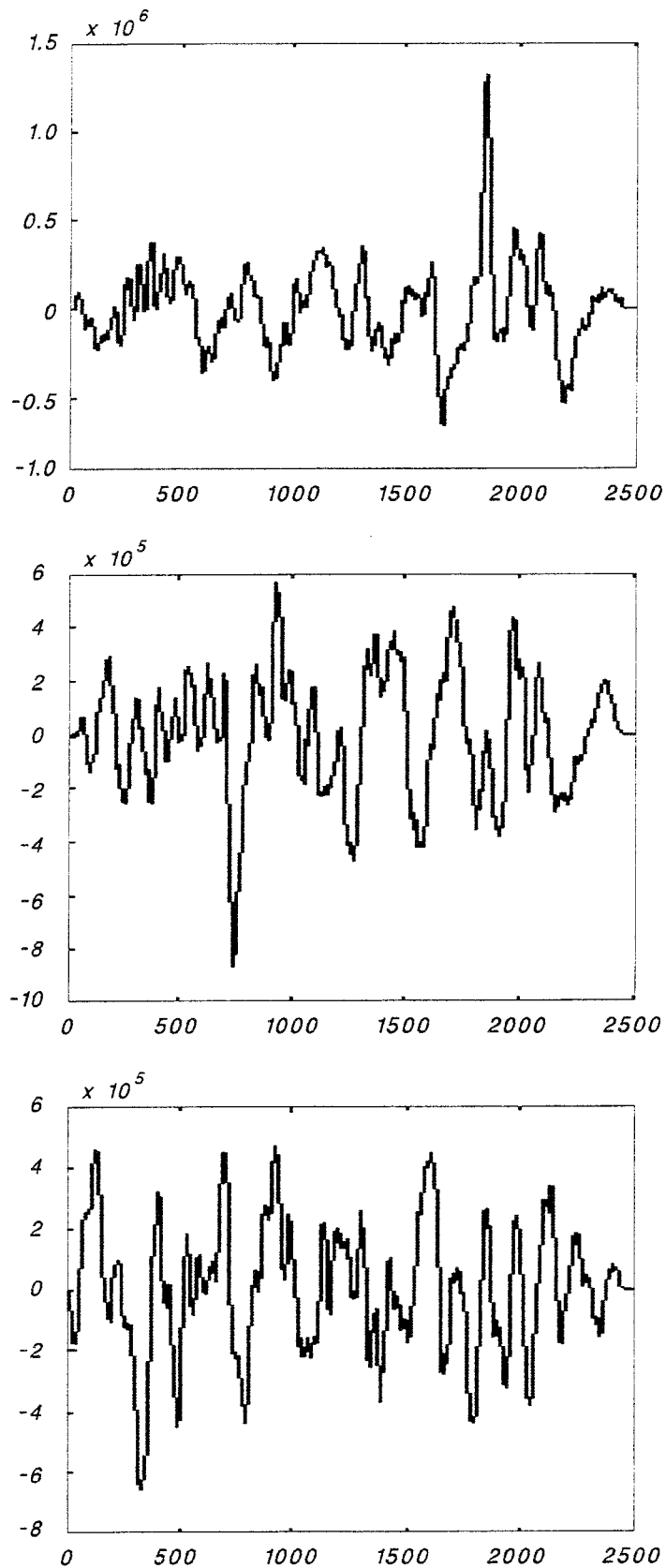
Figure 6.2-24. Cross-correlation between the abnormal section in profile CSouth10 at a depth of 5050 - 5150 mm, and the neighbouring profiles CSouth10 (top), Csouth11 (center) and CSouth12 (bottom) shown in Figure 6.2-26. Note the different scale on top figure.
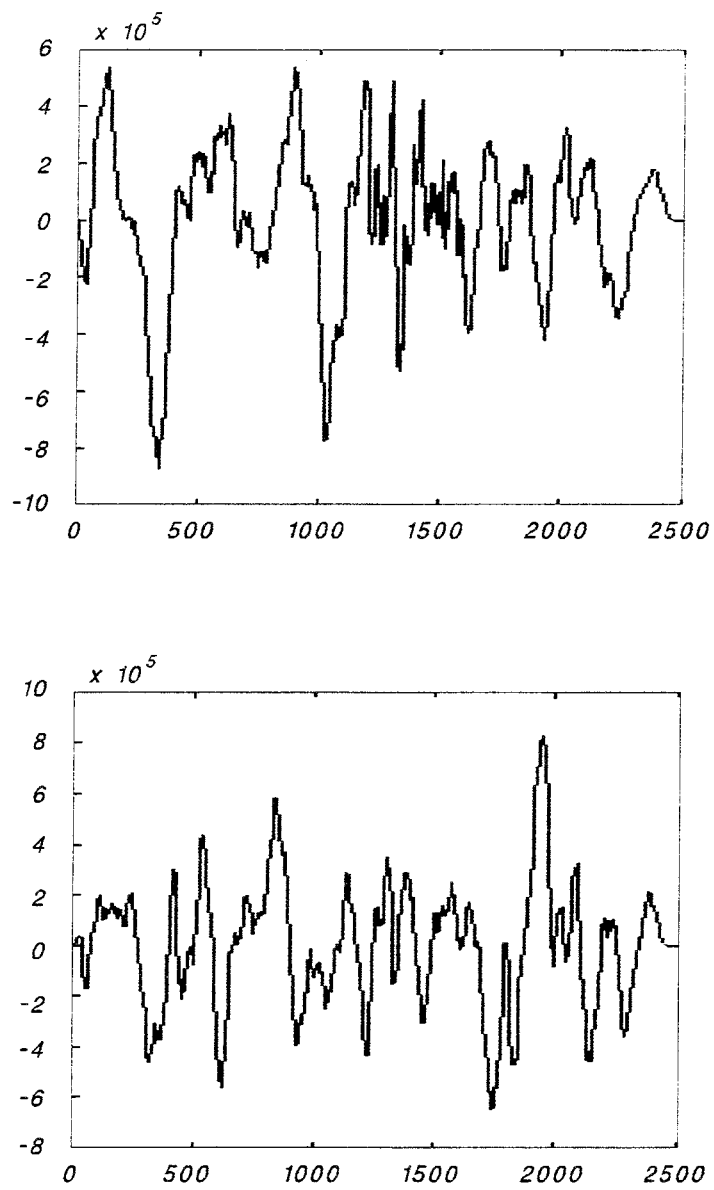
Figure 6.2-25. Cross-correlation between the abnormal section in profile *CSouth10* at a depth of *5050 - 5150 mm,* and the neighbouring profiles *CSouth13 (top)* and *CSouth14R (bottom)* shown in Figure 6.2-27.
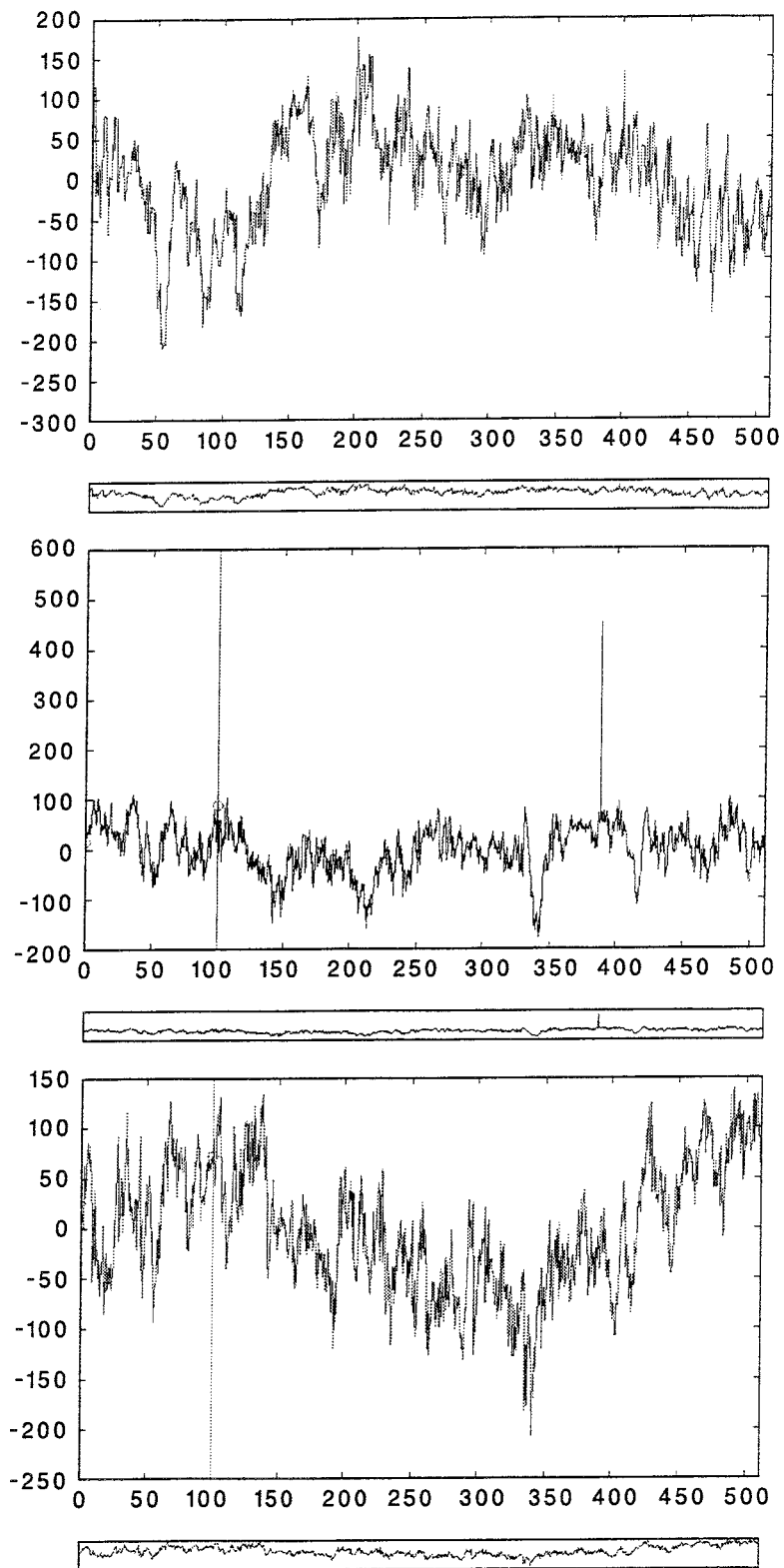
Figure 6.2-26. Profiles CSouth10 (top), Csouth11 (center) and CSouth12 (bottom).
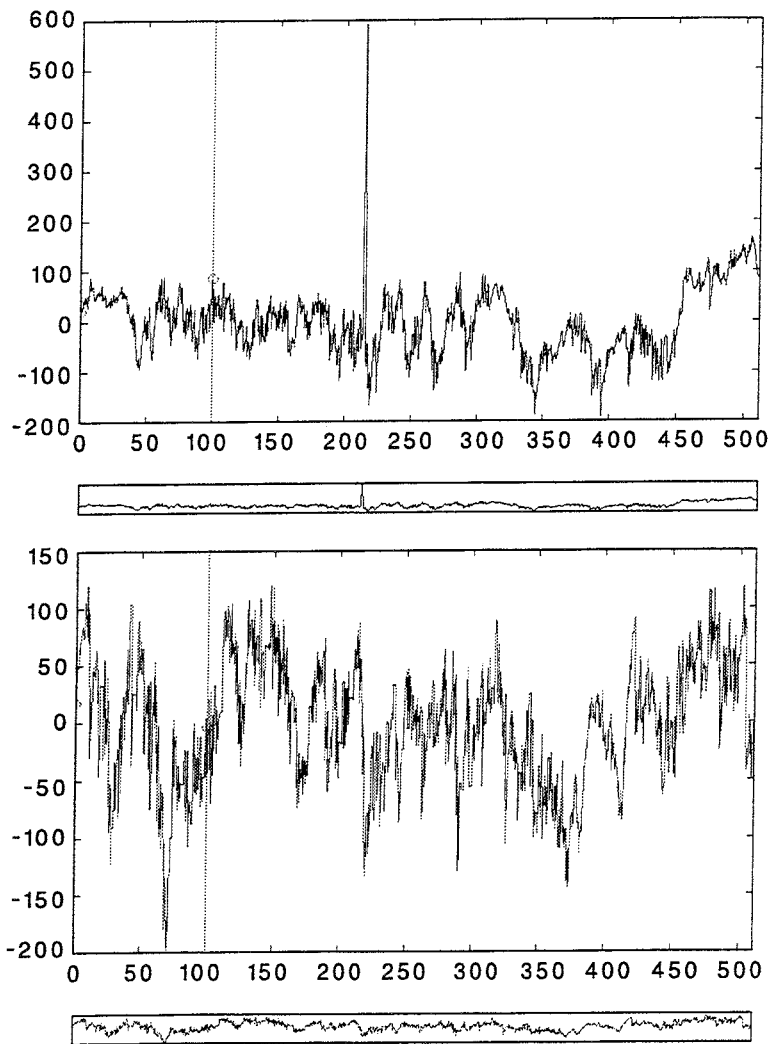
Figure 6.2-27. Profiles CSouth13 (top) and CSouth14R (bottom).

Some of the roughness anomalies were caused by contact between the gauge rollers and the surface of the rock or by penetration of the side button rows in the roller cutters into the rock surface. The reasons for these occurrences were assumed to be:

- movement of the cutter head caused by loose blocks of rock breaking away from the collar around the pilot hole

- movement of the cutter head caused by loose blocks of rock breaking away from the bottom of the large hole during boring

- repositioning of the cutter head for example after a lifting and inspection operation

- periodic movement of the drill string and cutter head.

6.3   DISCUSSION

The degree of surface roughness affects both the total surface area of the full-scale experimental deposition holes and their total volume. An estimation of these parameters was carried out by using the surface roughness data obtained as described in the preceeding sections and is shown in Table 6.3-1.

The increase in the total surface area of the walls of the large holes when compared to an ideal cylinder of equivalent dimensions was estimated to be 15% and the consequent increase in total volume was estimated be in the range 0.3 to 0.4%.

Any deflection of the hole also has an effect on the total surface area and total volume of the hole when compared to an ideal cylinder. Using the data in Table 6.3-1 a similar calculation was made for holes similar to deposition holes of two different nominal diameters, 1.5 and 1.6 m, both without deflection and with a deflection of 22 mm. The results of these calculations are in Table 6.3-2.

Table 6.3-1. Estimated volumes of Large holes 2 and 3. This estimate was based on the maximum peak heights H_{max}, average surface line lengths S and the average cross-sectional area A_k calculated from the profile measurements. See Figure 6.3-1 for explanations.

	Hole 2	Hole 3
Radius of the equivalent cylinder (cm)	76.20	76.20
Radius of the hole (cm)	76.33	76.43
Depth of the hole (m)	7.50	7.50
Relative length of the surface line, S (cm/m)	114.58	114.81
Relative area of the hole, A_H (m^2/m)	5.495	5.513
Area of the equivalent cylinder, A_C (m^2)	35.91	35.91
Area of the hole, A_H (m^2)	41.21	41.35
Surface area of the walls and bottom of the hole, A_{H2} (m^2)	43.04	43.18
Relative area of the cross section, A_k (cm^2/m)	16.34	12.08
Relative volume of the cross section, V_k (cm^3/m)	7835	5798
Volume of the cross section, V_k (m^3)	0.059	0.043
Volume of the equivalent cylinder, V_C (m^3)	13.681	13.681
Volume of the hole, V_H (m^3)	13.740	13.725
Relative volume of the hole, V_H (m^3/m)	1.832	1.830
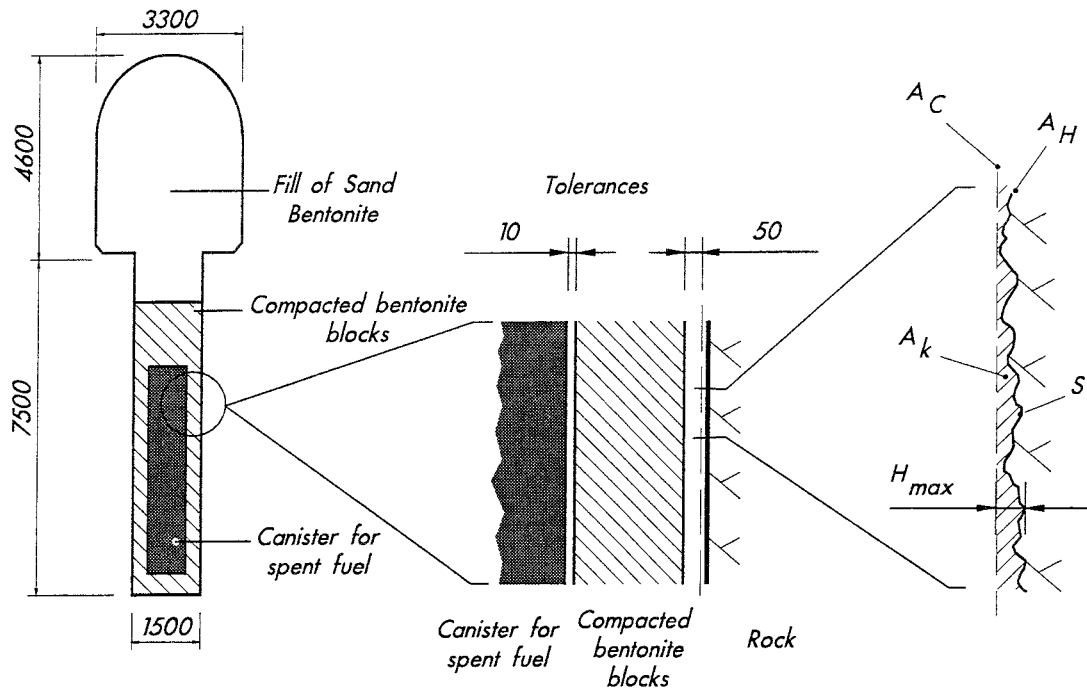
Figure 6.3-1. The effect of surface roughness on the volume and surface area of a KBS-3-type deposition hole. H_{max} is the peak height, S is the length of the surface line, A_H is the area of the surface of the hole, A_C is the cross-sectional area of the largest ideal cylinder (equivalent cylinder) which can be emplaced in the hole and A_k is the cross-sectional area of the profile.

The figures show that the total volume of the hole with a 1.6 m nominal diameter is 0.35 - 1.07% greater (the larger value corresponding to a hole with a deflection of 22 mm), than it would be in the case where the surface of the hole was completely smooth. In the case of the holes with a nominal diameter of 1.5 m the corresponding increase in volume is 0.38 - 1.10%. In both cases the surface area is correspondingly 16 - 17% greater than it would be if the surface of the holes were to be completely smooth.

As can be seen from Table 6.3-2 and Figure 6.3-2 the diameter of the hole must be slightly larger if the hole is deflected than when the hole is straight to fit in a cylinder of equal size, in the example shown the extra required being 5 - 6 mm.

The measurement of surface roughness by laser profilometer can be carried out with much higher accuracy if a smaller laser spot size is employed. Laser equipment with a spot diameter of 80 micrometers is available today but the benefit to be derived from such measurements is not obvious since the surface properties of the mineral grains seem to increase the degree of noise in the measurements. Use of a larger spot size resulted in partial smoothing of the measurements carried out.

Table 6.3-2. The estimated volumes of holes similar to the KBS-3-type deposition holes with a diameter of 1.5 and 1.6 m, length 7.5 m and deflections of 0 and 22 mm. See figure 6.3-2 for an explanation of deflections. The equivalent cylinder is the largest ideal cylinder (with a smooth surface) which can be emplaced in the rough-surfaced hole.

Minimum diameter of the hole D (m)	1.600	1.606	1.500	1.505
Heigth of the hole H (m)	7.50	7.50	7.50	7.50
Deflection of the hole s (mm)	0	22	0	22
Diameter of the equivalent cylinder d (m)	1.600	1.600	1.500	1.500
Surface area of the walls A_H (m^2)	43.202	43.358	40.502	40.649
Surface area of the walls and bottom of the hole A_{H2} (m^2)	46.218	46.396	43.153	43.318
Volume of the holes V_H (m^3)	15.134	15.242	13.304	13.400
Equivalent surface area of a cylinder A_C (m^2)	37.699	37.699	35.343	35.343
Equivalent surface area of the walls and bottom of the cylinder A_{C2} (m^2)	39.710	39.710	37.110	37.110
Equivalent volume of the cylinder V_C (m^3)	15.080	15.080	13.254	13.254
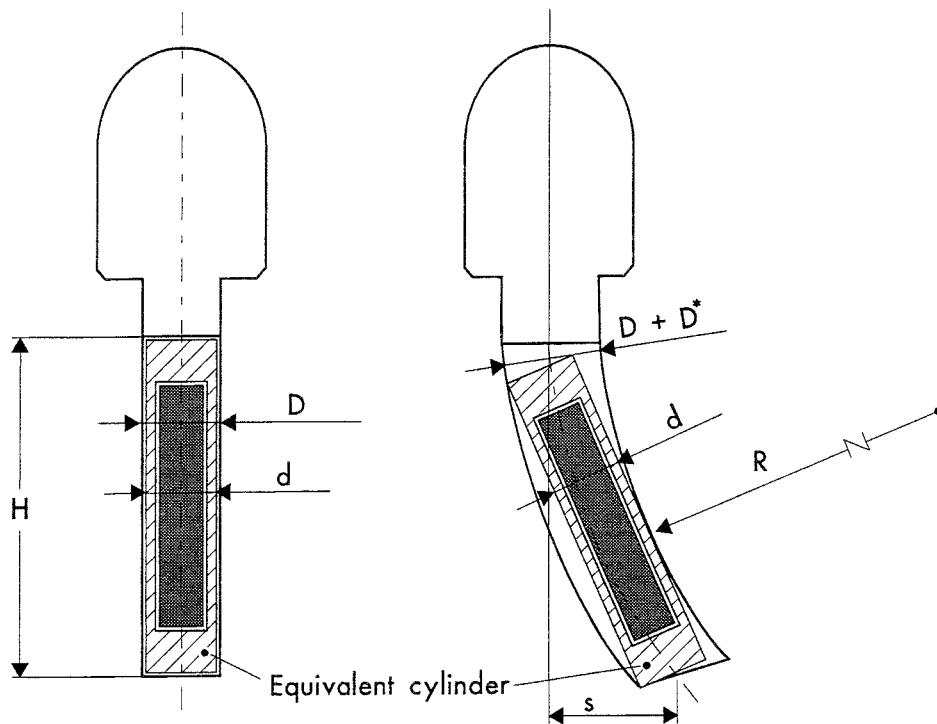
Figure 6.3-2. Deflection of a deposition hole and the principle behind its consideration in the calculations shown in Table 6.3-2.

amplitude, spatial, hybrid and functional parameters from the ones employed here can be determined. The accuracy of currently available surface topography measurement methods ranges from the atomic level with confocal SEM to conventional mechanical profiling and from ångstroms to kilometers. When evaluating alternative methods it is essential to remember that the objective of making the measurements is to reduce the topography data to essential parameters which can be used to characterize the surface properties. These parameters should have a clear physical interpretation since from the engineering point of view the purpose of surface characterization is to support and guide the design process. According to the experience gained during this work the method of measuring surface roughness used was accurate enough to produce information about the effect of the boring technique on the surface roughness and final dimensions of the holes. The standard parameters calculated for the surface roughness profiles were found to be useful to locate areas of different surface roughness. The method of measuring surface roughness used was found to be effective and reliable and, according to the experience gained, should be easy to automate.

The main advantages of the laser profilometer method when compared to the use of mechanical profilers, in addition to the increase in accuracy, is the ease of automating the measurement process, the ability to make measurements rapidly, the fact that the results are produced directly in data form and that measurements can be carried out without making contact with the surface.

It is suggested that further development should focus on the extraction of useful parameters from the surface roughness data. Use of 2-D or 3-D texture analysis and the development of functional parameters which characterize, for example, the surface area, changes in rock type and cutter head movement rates would appear to hold promise.

7   EXCAVATION DISTURBANCE CAUSED BY BORING

7.1   GENERAL

The disturbance of the rock structure caused by the boring process (the excavation disturbance) was studied by using two novel methods: the ^{14}C-PMMA method (Siitari-Kauppi 1995); and the He-gas method (Hartikainen et al. 1995). Studies were made in the laboratory by examining 98 mm diameter core samples taken from different parts of the large holes which were representative of different boring parameters, see Figure 7.1-1. The properties of both disturbed and undisturbed rock were studied.

A short description of the novel He-gas and the ^{14}C-PMMA methods is given before the results of the different studies are presented and analyzed. As these techniques were being employed for the first time in this type of application some conclusions about the suitability of the techniques are drawn.
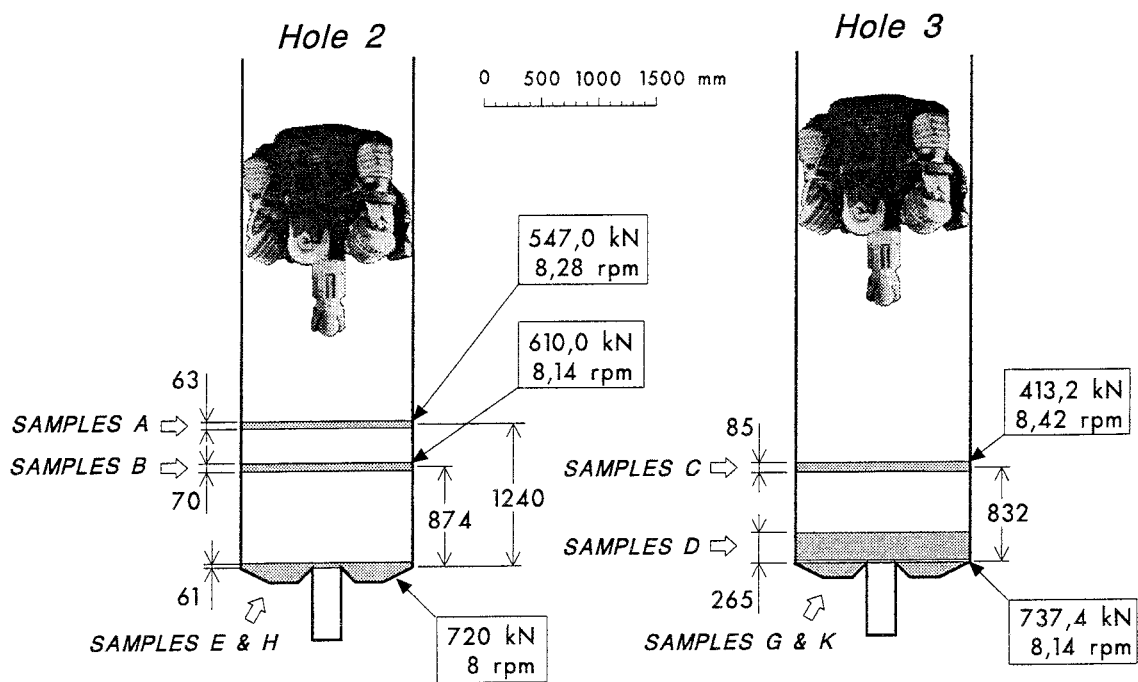
Figure 7.1-1. The location of sampling sections in the experimental full-scale deposition holes with the corresponding boring parameters (Autio et al. 1995).

7.2 ^{14}C-PMMA METHOD

The degree of mechanical disturbance of the rock in the side walls was assessed by using the novel ^{14}C-PMMA method (Siitari-Kauppi 1995) to investigate the geometry of microfractures and determine porosity profiles.

The ^{14}C-PMMA method involves impregnation of the rocks with ^{14}C labeled methylmethacrylate (^{14}C-MMA), irradiation polymerization, sample partitioning as shown in Figure 7.2-1, autoradiography (Figures 7.2-2 and 7.2-3 are examples of autoradiographs), and optical densitometry using digital image processing techniques. The detection limit of the ^{14}C-PMMA method is ±0.05 vol.% expressed as total porosity (Siitari-Kauppi et al. 1995). The different steps in the method and typical values for the parameters employed are shown in Figure 7.2-4. The impregnant, methylmethacrylate (MMA) is a monomer with low viscosity (0.00584 P, Daniels 1967) and small molecule size (Mol. Weight 100.1). It exhibits non-electrolytic properties and low polarity, behaving in the rock matrix as a non-sorbing tracer. The principles of the method have been described in greater detail in (Siitari-Kauppi 1995, Hellmuth et al. 1993 and Hellmuth et al. 1994). Results obtained by the method allow porosity profiles of selected sections to be determined. Examples of such profiles are shown in Figures 7.2-5 and 7.2-6.

In addition to the ^{14}C-PMMA method, optical microscopy, scanning electron microscopy (SEM) and energy dispersive X-ray analysis (EDS) were used to investigate the pore apertures and mineral structure of porous regions in greater detail. The SEM/EDS measurements were conducted on ^{14}C-PMMA impregnated samples which had been coated with carbon.
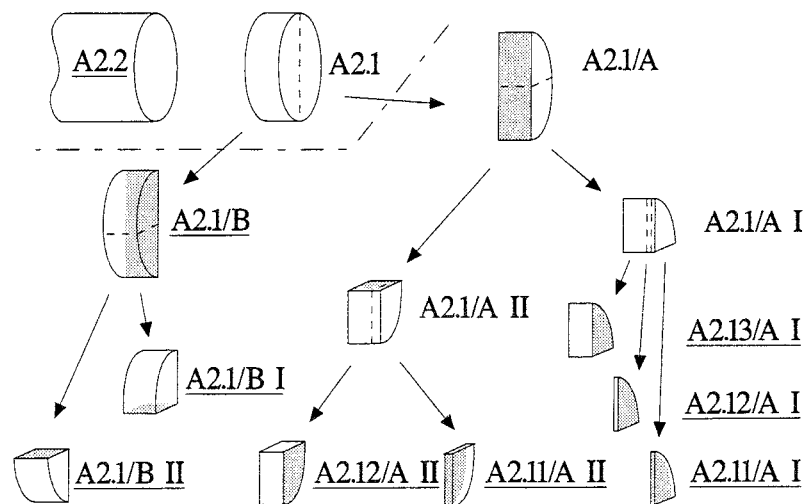
Figure 7.2-1. Partitioning diagram for ∅ 98 mm Core Sample A3 from full-scale experimental deposition hole 2. The exposed surfaces shown shaded gray were examined using the ^{14}C-PMMA method.
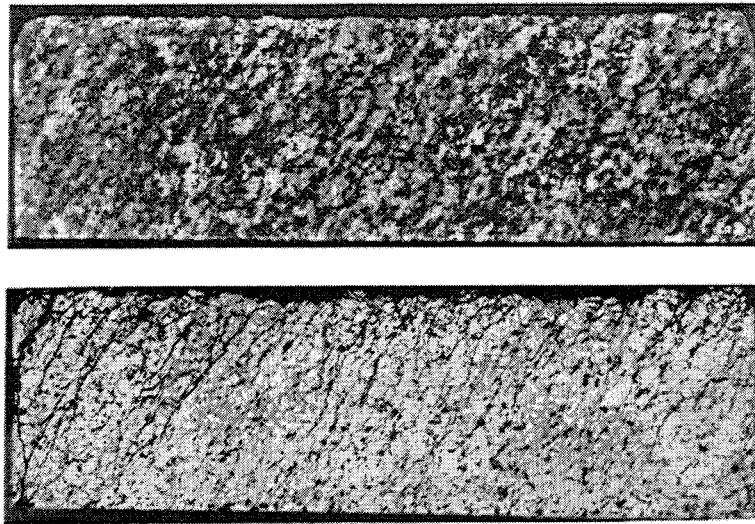
Figure 7.2-2. Example of a photograph (top) and corresponding autoradiograph (bottom), Sample C2. The upper surface is section through part of the surface of Large hole 3. The plane of the section is perpendicular to the surface. Different levels of gray represent different degrees of porosity.
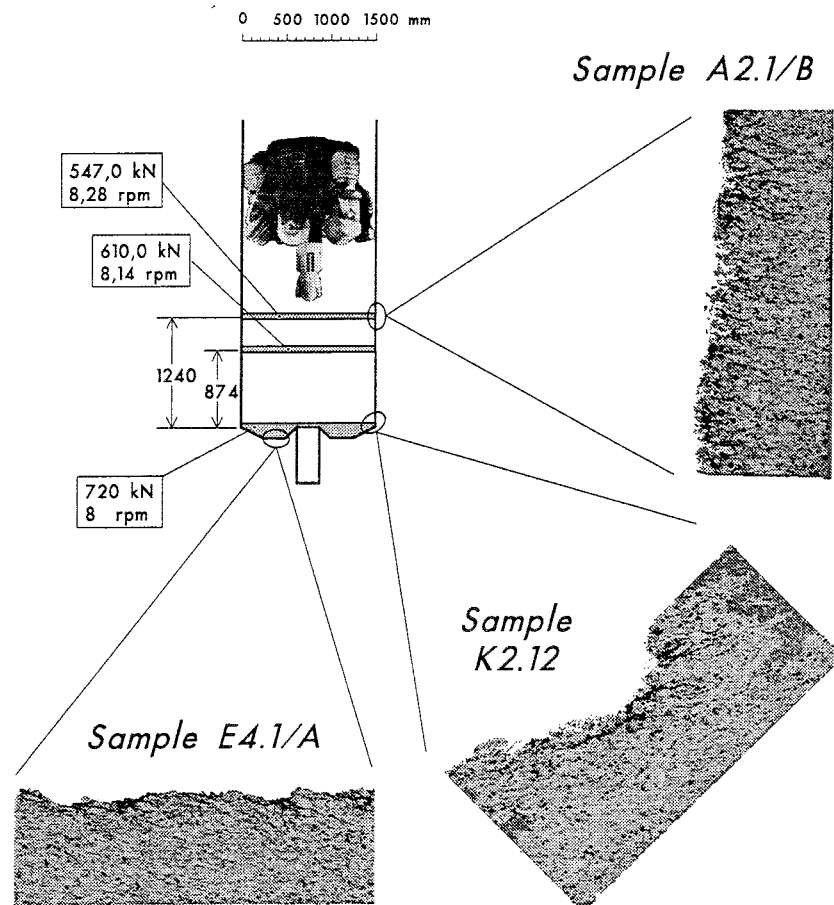
Figure 7.2-3. Examples of autoradiographs produced with the ^{14}C-PMMA method from sections of core samples taken from the surface of the full-scale deposition holes.

```
┌─────────────────────────┐
│      rock sample        │
│    drilling, sawing     │
└────────────┬────────────┘
             │
┌────────────┴────────────┐
│        drying           │
│  80°C,vacuum, 8-13 d     │
└────────────┬────────────┘
             │
┌────────────┴────────────┐
│     impregnation        │
│  ¹⁴CMMA, 50 µCi/ml,      │
│        8-14 d           │
└────────────┬────────────┘
             │
┌────────────┴────────────┐
│     polymerization      │
│ Co-60 irradiation 50 kGy │
└────────────┬────────────┘
             │
┌────────────┴────────────┐
│   thermoluminescence    │
│   heating 120°C, 3 h     │
└────────────┬────────────┘
             │
┌────────────┴────────────┐
│   sample preparation    │
│     diamond sawing      │
└────────────┬────────────┘
             │
┌────────────┴────────────┐
│     autoradiography     │
│     exposure 9-24 d      │
└────────────┬────────────┘
             │
┌────────────┴────────────┐      ┌─────────────────────────┐
│  digital image analysis │──────│    porosity histogram   │
│      table scanner      │      │     porosity profile    │
└─────────────────────────┘      └─────────────────────────┘
```
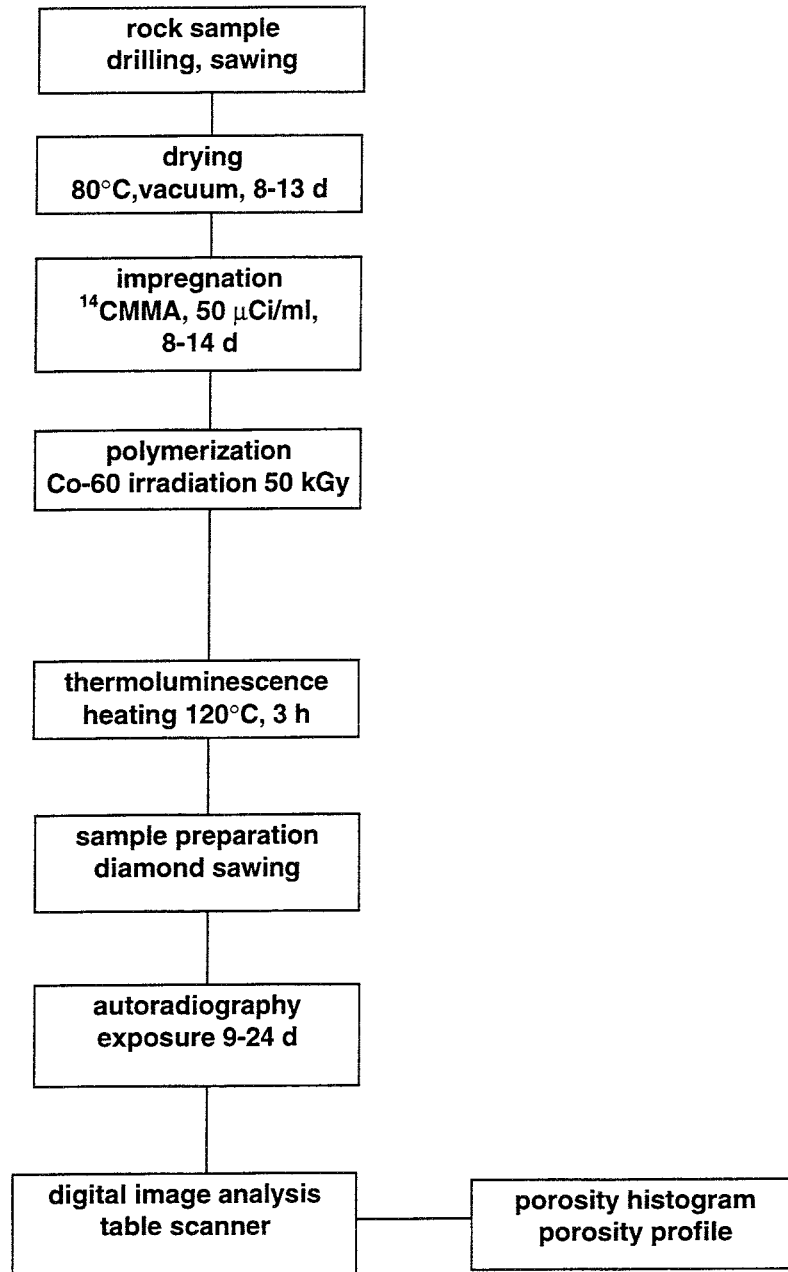
Figure 7.2-4. The ^{14}C-PMMA method.
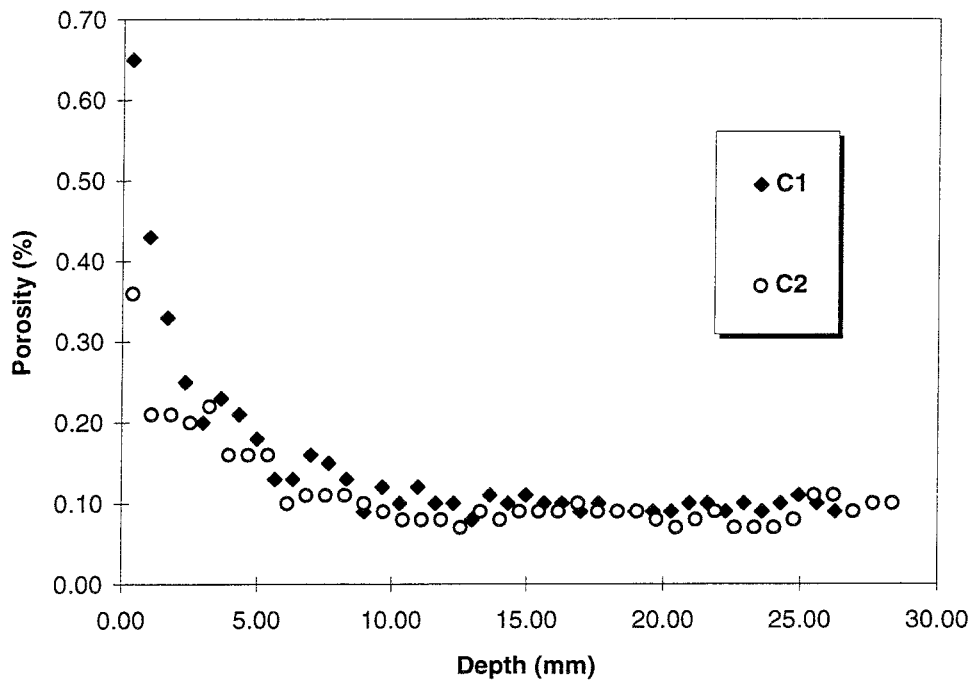
Figure 7.2-5. *Porosity profiles of samples in Series C. A section through sample C2 is shown in Figure 7.2-2. Porosity values are shown in relation to depth from the disturbed surface (Siitari-Kauppi 1995).*
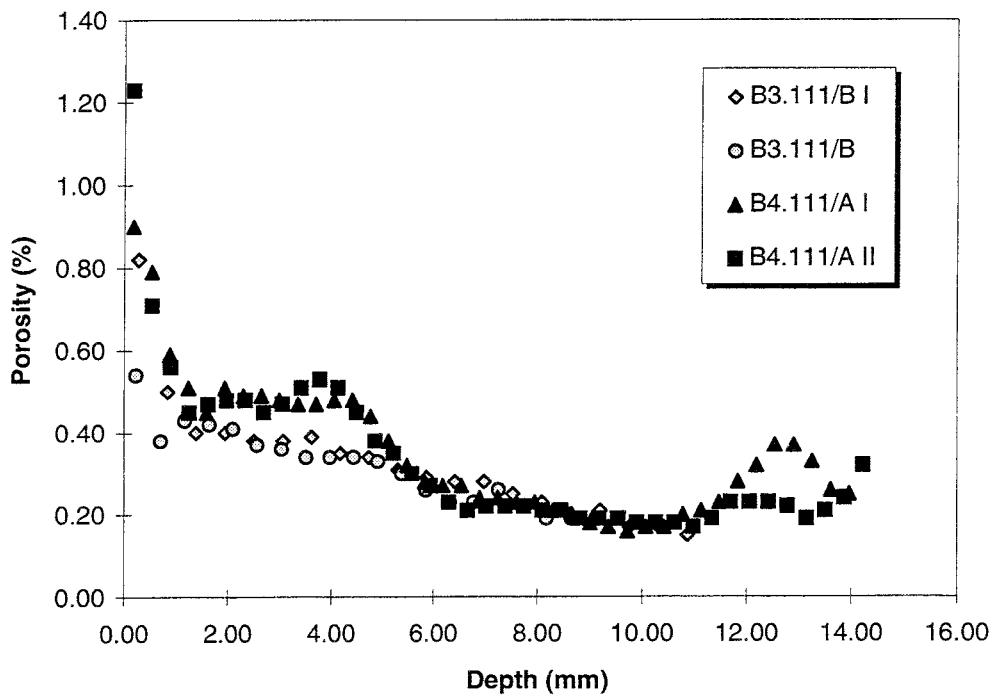
Figure 7.2-6. *Porosity profiles of samples in Series B. Porosity values are shown in relation to depth from the disturbed surface (Siitari-Kauppi 1995).*

7.3   He-GAS METHOD

The degree of disturbance of the rock in the side walls of the large holes was determined from samples cored from six positions in sampling sections B and D (Figure 7.1-1). Disturbance was established in terms of the effective diffusion coefficients, porosities and coefficients of permeability as shown in Figure 7.3-2. A novel method employing helium gas (the He-gas method) was used (Hartikainen et al. 1995).

The basis of the He-gas method is either the diffusion (see Figure 7.3-1) or flow of helium through a rock sample that has been saturated with nitrogen gas. In the case of permeability measurements the flow through the sample is initiated by a pressure gradient as shown in Figure 7.3-2. The He-gas method allows measurements to be made in a much shorter time than that required to carry out measurements in the liquid phase on samples of large size. The technique is described in greater detail in (Hartikainen et al. 1994 and Hartikainen et al. 1995).
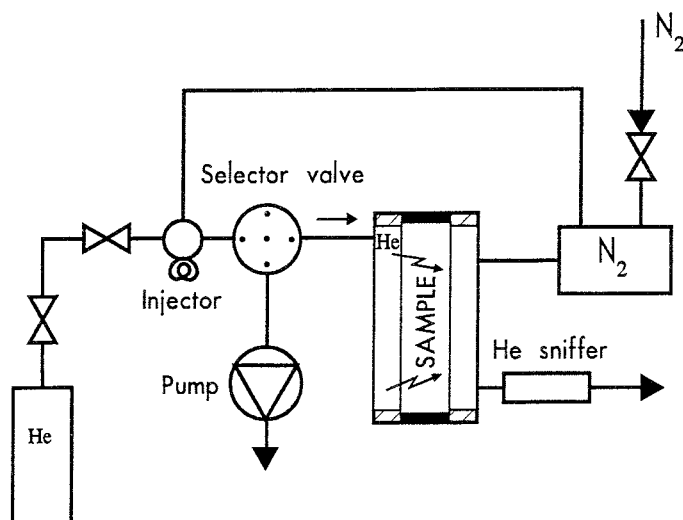
Figure 7.3-1. Experimental apparatus for measurement of through-diffusion (Hartikainen et al. 1995).
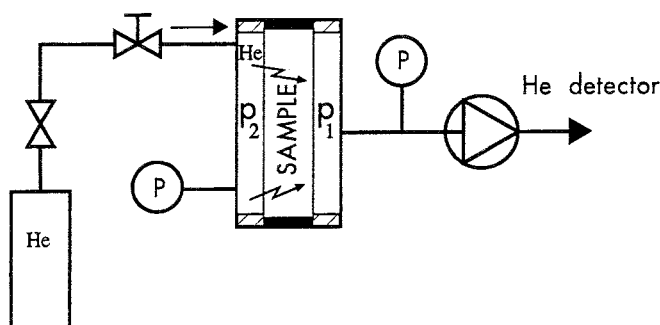
Figure 7.3-2. Experimental apparatus for measurement of permeability (Hartikainen et al. 1995).

7.4 PROPERTIES OF THE DISTURBED ZONE

7.4.1 General

Results obtained with both the ^{14}C-PMMA method and the He-gas method revealed a distinct zone of disturbance caused by the boring of the experimental full-scale deposition holes. The porosity, permeability and effective diffusion coefficient of the rock in the excavation-disturbed zone were all affected to depths ranging from 8 to 34 mm from the disturbed surface.

The geometry and porosity of the excavation-disturbed zone is first characterized by examining the results obtained with the ^{14}C-PMMA method. The results of measurements obtained with the He-gas method are handled later since the results provided by the ^{14}C-PMMA method reveal information which is significant when evaluating the results of permeability and diffusion measurements made with the He-gas method.

7.4.2 Porosity of the disturbed zone

Average porosity profiles determined perpendicular to the disturbed wall surface for sample sets A, B, C, D, H and K can be seen in Figure 7.4-1. Both the porosities given for each individual sample and the porosity profiles shown are the averages of the many determinations made in order to eliminate errors caused by natural variations in rock composition. The porosity profile obtained for Sample K2 exhibited anomalous variations which were assumed to be the result of the presence of clusters of mafic and felsic minerals. The results obtained for sample set K are therefore of limited value.

To eliminate the effect of differences in background porosity levels, the porosity profiles for sample sets A, B, C, D and H shown in Figure 7.4-1 were normalized to yield the profiles shown in Figure 7.4-2. Normalization was carried out with respect to the porosity value of undisturbed rock, this being determined as the average of the porosity values given by the profiles at depths of 12 to 15 mm from the excavation-disturbed surface.

The distribution of normalized porosities in the depth interval from 12 to 15 mm in the undisturbed section of the porosity profiles obtained from sample sets A, B, C, and D is shown in Figure 7.4-3 together with a normal distribution curve. The distribution of normalized porosities does not resemble a standard distribution, and there is a significant drop in frequency at a level 10% higher than the average porosity. This feature was chosen as the criteria for establishing disturbance i.e. the thickness of the zone of increased porosity, h, which was defined to be the distance from the disturbed surface at which the measured porosity value fell for the first time to a cut-off level 10% higher than the reference level for undisturbed rock.

Porosity profiles perpendicular to the disturbed surface
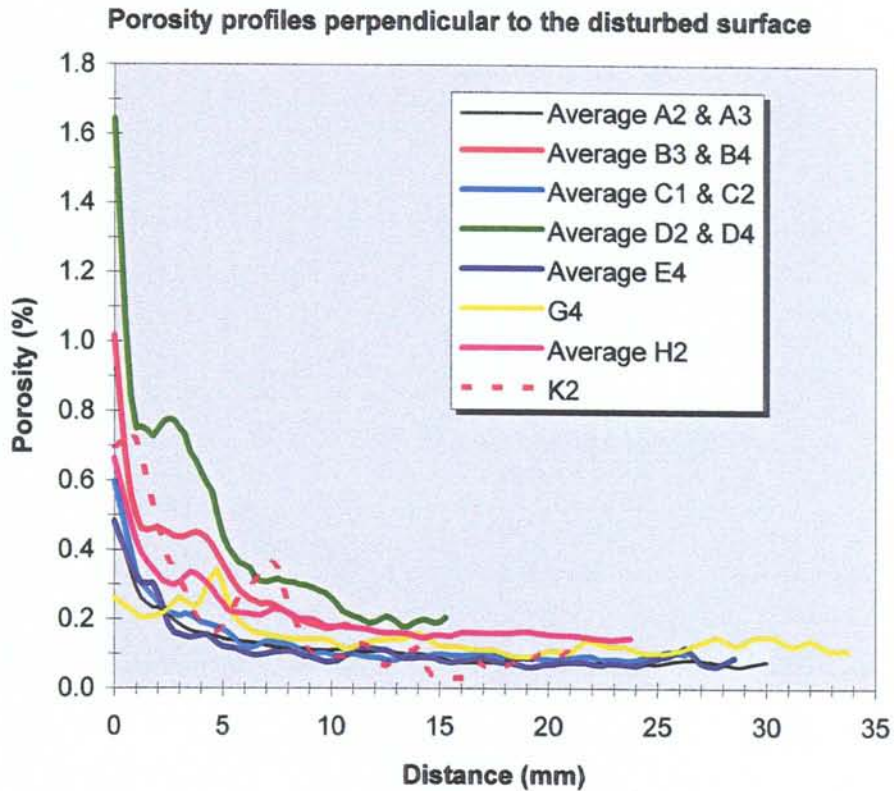
Figure 7.4-1. Averages of all the porosity profiles measured perpendicular to the excavation-disturbed surface of the large holes. A, B, C and D represent samples taken from the walls, E and G represent samples taken from the floor and H and K represent samples taken from the corners.
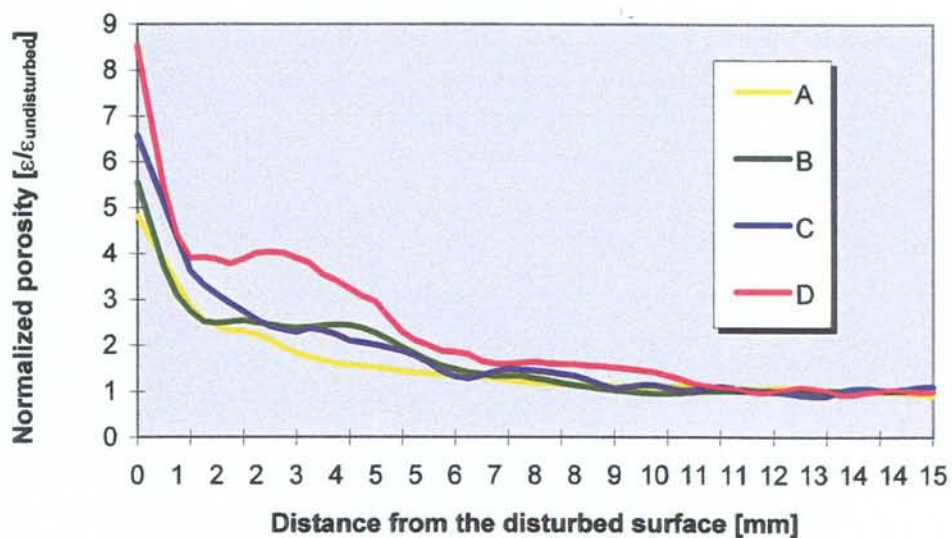
Figure 7.4-2. Normalized porosity profiles perpendicular to the walls of the large holes. The average value for the porosity of undisturbed rock was 0.14 vol.%.
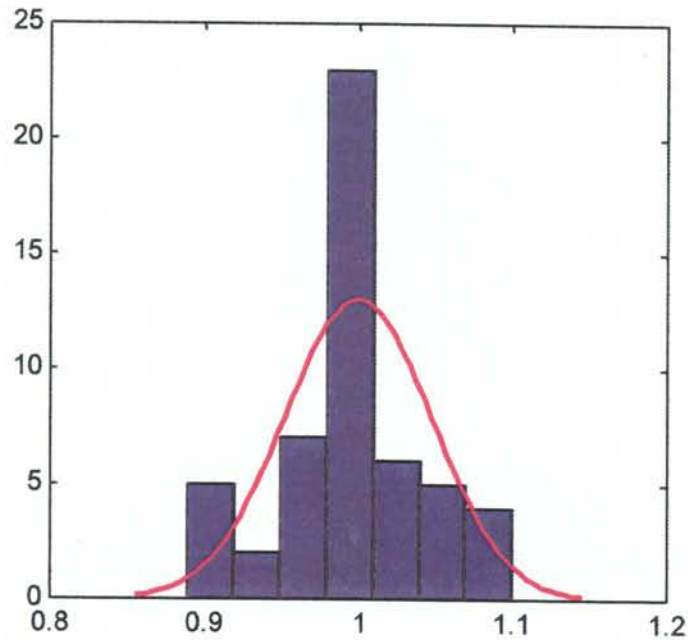
Figure 7.4-3. *The distribution of scaled porosities in the undisturbed section of the porosity profiles for sample sets A, B, C, and D and a normal distribution curve. The cut-off level of the normalized nondimensional porosity used to determine the limit of the excavation-disturbed zone was 1.1.*

The thickness of the zone of increased porosity (h) shown in Table 7.4-1 was calculated from the normalized porosity profiles shown in Figure 7.4-2 using the criteria already specified. The extent of this zone was lowest in sample set B (8.5 mm) and highest (excluding values obtained from sample set K) in sample set H (11.5 mm), the average value for sample sets A, B, C, D and H being 10.0 mm.

The porosity of the undisturbed rock was determined in order to provide a reference value for comparison. The porosity of undisturbed rock in all the 98 mm diameter samples was measured using the ^{14}C-PMMA method and found to lie within the range 0.09-0.19 vol.%. The porosity of a smaller, 42 mm diameter sample of undisturbed rock taken from the position of the investigation holes (i.e. a sample cored prior to the boring of the full-scale deposition holes) was also measured and found to lie in the range 0.13-0.15 vol.%. The average porosity of undisturbed rock in sample sets A, B, C, D, H and the smaller diameter core samples was calculated to be 0.14 vol.%. This value was then taken as the reference value for the average porosity of undisturbed rock, and the average porosities for rock in the disturbed zones were made comparable by calculating them from the normalized porosity profiles using 0.14 vol.% as the value for the porosity of undisturbed rock.

The average initial measured porosities of rock in the excavation-disturbed zone ranged from 0.16 vol.% in sample set E to 0.53 vol.% in sample set D.

Excluding values from sample set K, the adjusted average porosities, ε_{ave}, for the excavation-disturbed zone calculated from the normalized porosity values using a value of 0.14 vol.% for the porosity of undisturbed rock, ranged from 0.19 vol.% in sample set G to 0.38 vol.% in sample set D, see Table 7.4-1.

The average porosities, ε_{ave}, used for comparison purposes were calculated over the full distance from the excavation-disturbed surface to h. There are inaccuracies in the porosity values obtained for the first 1.5 mm of this distance. These inaccuracies are primarily the result of the existence of wide aperture fractures which do not satisfy the fundamental requirements of the method. The inaccuracies have the effect of reducing measured porosities with respect to actual real values. Average porosities, $\varepsilon_{ave,1.5-h}$, used for comparison purposes were therefore also calculated over a distance of 1.5 mm from the disturbed surface to h. The average values for the porosity of the disturbed zone over this range, $\varepsilon_{ave,1.5-h}$, (excluding values obtained from sample set K) ranged from 0.18 vol.% in sample set G to 0.32 vol.% in sample set D, see Table 7.4-1.

The average values for additional porosity, ε_d, caused by disturbance of the rock during excavation, were calculated by subtracting the porosity of undisturbed rock from the porosity profiles. This operation was carried out for the whole of the extent of the disturbed zone and also for additional porosity for the range 1.5 mm to h, $\varepsilon_{dave,1.5-h}$. The results obtained emphasize the differences found between the sample sets, see Table 7.4-1.

The quantity of additional pore space caused by disturbance during excavation per unit length of surface, V_d, was calculated by integrating the measured porosity over the measured length of the disturbed zone. This gives the area A shown in Figure 7.4-4 and hence the total pore volume. The value for the porosity of undisturbed rock was then subtracted to obtain the amount of additional porosity caused by disturbance during excavation. This same procedure was carried out over the range 1.5 mm to h to obtain the area A" shown in Figure 7.4-4 (an explanation of the reasons for doing this has already been given). The results are shown in Table 7.4-1. The additional pore volume V_d in sample sets A, B, C and D ranged from 11 cm^3/m^2 in sample set B to 26.6 cm^3/m^2 in sample set D.

Porosity values and the extent of the disturbed zone in floor sample sets E and G (see Figure 7.4-5) are clearly smaller than corresponding values in samples taken from the walls of the large holes, this can be clearly seen from Table 7.4-1.

The average porosities, ε_{ave}, for the floor sample sets (E and G) and the wall sample sets (A, B, C and D) were 0.21 vol.% and 0.63 vol.% respectively. Corresponding values for the additional porosity caused by disturbance during excavation, ε_d, were 0.07 vol.% and 0.35 vol.% respectively and for the additional pore volume, V_d, 4.5 and 17.2 cm^3/m^2 respectively.

Table 7.4-1. Thickness of the zone of increased porosity h, average porosity values and additional pore volume caused by disturbance during excavation.

Samples	h [mm]	ε_{ave} [%]	$\varepsilon_{ave,1.5\text{-}h}$ [%]	ε_d [%]	$\varepsilon_{d,1.5\text{-}h}$ [%]	V_d [cm³/m²]	$V_{d,1.5\text{-}h}$ [cm³/m²]
A- wall	9.25	0.26	0.21	0.12	0.07	10.99	5.58
B- wall	8.50	0.31	0.26	0.17	0.12	14.26	8.70
C- wall	10.00	0.31	0.25	0.17	0.11	16.91	9.09
D- wall	11.00	0.38	0.32	0.24	0.18	26.65	17.29
E- floor	6.00	0.23	0.19	0.09	0.05	5.69	2.24
G- floor	7.00	0.19	0.18	0.05	0.04	3.37	2.34
H- corner	11.50	0.26	0.22	0.12	0.08	13.40	8.26
K- corner	12.25	0.52	0.41	0.38	0.27	46.13	29.42

h, thickness of the zone of increased porosity

ε_{ave}, average porosity of the disturbed zone of thickness h

$\varepsilon_{ave,1.5\text{-}h}$, average porosity of the disturbed zone from depth 1.5 mm to h

ε_d, average additional porosity caused by the disturbance

$\varepsilon_{d,1.5\text{-}h}$, average additional porosity caused by the disturbance from depth 1.5 mm to h

V_d, additional porespace caused by the disturbance per unit area of the hole surface

$V_{d,1.5\text{-}h}$, additional porespace caused by the disturbance per unit area of the hole surface from depth 1.5 mm to h
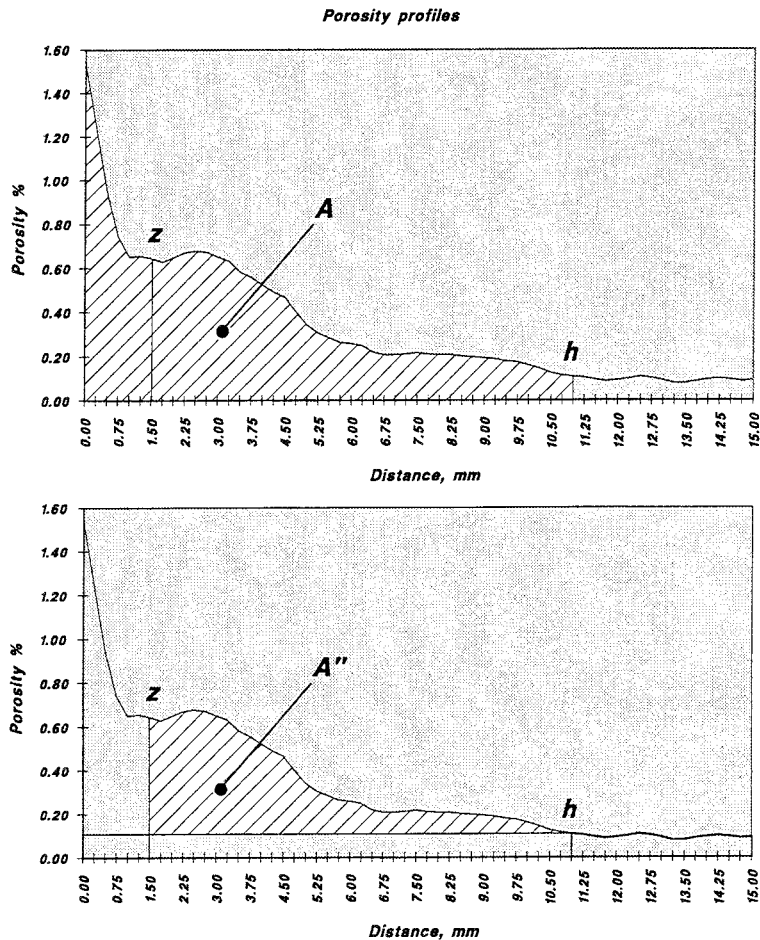
Porosity profiles

Figure 7.4-4. The areas A and A" integrated from the porosity profiles to obtain the average pore volume (A) of the disturbed zone, and the average additional pore volume (A") over the range 1.5 mm to h resulting from disturbance during excavation. In this case the depth of the zone of increased porosity was 11.0 mm.

An exponential function (of type $y = cx^b$) was found to give the best fit with correlation for R^2 of 0.90 to 0.99, see Figure 7.4-6. The correlation was better in the case of sample sets A and C, correlation coefficient R^2 being 0.99 and 0.96 respectively. The porosity profiles obtained for sample sets B and D, which were thinner and measured using both the ^{14}C-PMMA and He-gas methods, are not as smoothly curved as the corresponding profiles for sample sets A and C. In sample sets B and D there appears to be a section in the porosity profiles between depths of 1 and 4 mm in which porosity does not decline with increasing distance from the disturbed surface, this is one obvious reason for the lower correlation obtained for sample sets B and D.
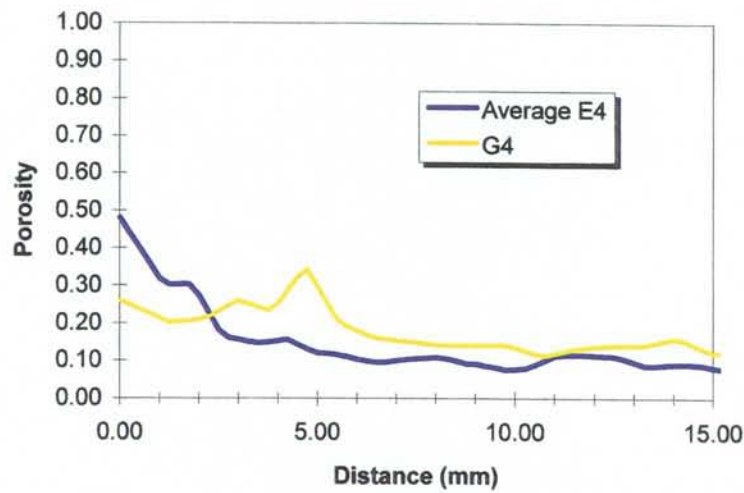
Figure 7.4-5. *Porosity profiles measured perpendicular to the floors of the large holes.*
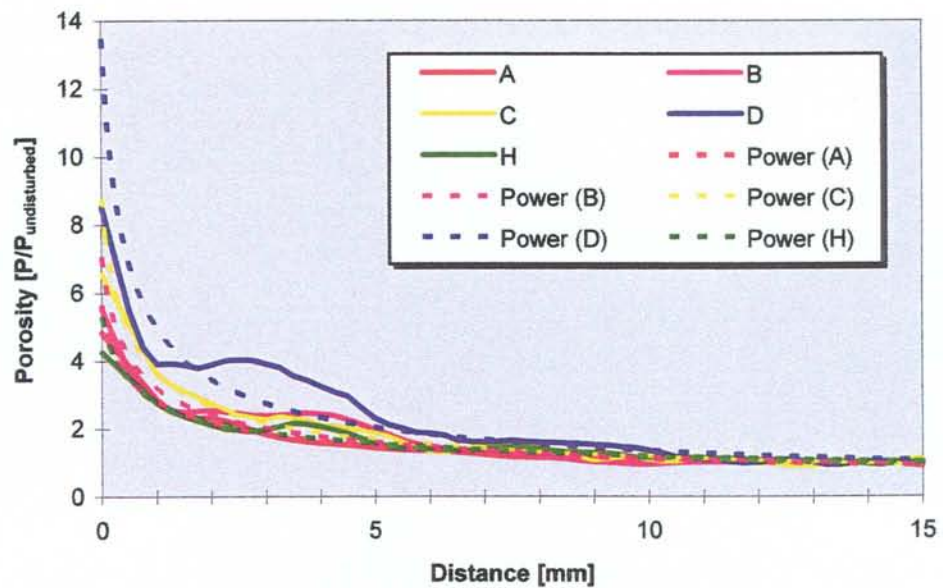
Figure 7.4-6. *Porosity profiles of sample sets A, B, C, D and H measured perpendicular to the walls of the full-scale holes, and the corresponding exponential regression functions.*

7.4.3　　Thickness of the disturbed zone

Two different definitions were used to determine the thickness of the excavation-disturbed zone after measurements with the ^{14}C-PMMA method, these are visualized in Figure 7.4-7. One definition was the thickness of the zone of increased porosity (h) as discussed in Section 7.4.2. The second definition was the thickness of the zone of increased fracturing (H) visible as porous tracelines or porous veins penetrating into the rock from the disturbed surface. In addition the thickness of the disturbed zone, h_{He} was determined using the He-gas method.

The thickness of the zone of increased fracturing (H) was determined by visual inspection and the measurement is therefore subjective. The accuracy of any estimate is also adversely affected by the fact that since the fracturing caused by disturbance during excavation merges gradually into the existing natural microfracturing or porosity of the rock, no exact point at which the boring-induced fracturing changes to natural fracturing can be established. Another source of inaccuracy in this determination is the exposure time used for the autoradiographs. In general, longer exposure times should give more distinct feature in the autoradiograph and enhance the low porosity zones (low activity levels). That might be the reason why the relative depth of the zone of increased microfracturing determined for wall samples B and D could be underestimated with respect to the corresponding zones in samples A and C. As the estimates for the depth of the zone of increased fracturing are subject to the limitations of visual assessment, minimum values are obtained. The uncertainty in the zone depth is given as a range in Table 7.4-2. The depth of the zone of excavation-disturbance in samples B and D was also evaluated by using the He-gas method, the results are shown in Table 7.4-2. The estimate was based on a two-layer model consisting of the excavation-disturbed zone and an undisturbed zone. Values for the undisturbed zone were measured and the properties and thickness of the excavation-disturbed zone were calculated on the basis of measurements made on samples of different thicknesses (Hartikainen et al. 1995).

The disturbed zone can be divided into three zones with different properties as shown in Figure 7.4-7. The first zone, from the excavation-disturbed rock surface inwards, is a zone of increased porosity and increased fracturing which exhibits higher helium permeability and coefficient of diffusion. This zone is followed by a zone which contains additional fracturing and which also exhibits higher helium permeability and coefficient of diffusion although within the accuracy of measurement, the actual porosity of the zone was the same as the porosity of undisturbed rock. The last zone was characterized only by increased fracturing.

The depth of the zone of increased porosity in the walls of the holes ranged from 8.5 mm in samples B to 11.0 mm in samples D and 11.5 mm in samples H. The depth of the zone of increased fracturing ranged from 12-18 mm in samples A to 15-31 mm in samples D and 25-32 mm in samples H (excluding samples K).

The thickness of the disturbed zone in samples B and D was calculated from the results of the measurements made using the He-gas method in terms of increased permeability and diffusitivity. The average thickness of the disturbed zone was found to be 18 mm in samples B and 19 mm in samples D.

The thickness of the disturbed zone was measured relative to the rock surface line in the measured profiles which was set manually as the line which passes along the lowest points in the profile so that the measuring window is totally within the rock. The roughness of the excavation-disturbed surface in the samples studied is estimated to cause inaccuracy which slightly decreases the measured thickness of the excavation-disturbed zone with respect to mean line of the real profile. In most cases, variations in the elevation of the excavation-disturbed surface under the measuring window were clearly less than 1 mm. Since every profile for sets of samples was average of many profiles it is estimated that the maximum inaccuracy caused by the determination of the surface line in the depth of the disturbed zone is clearly less than 1 mm.
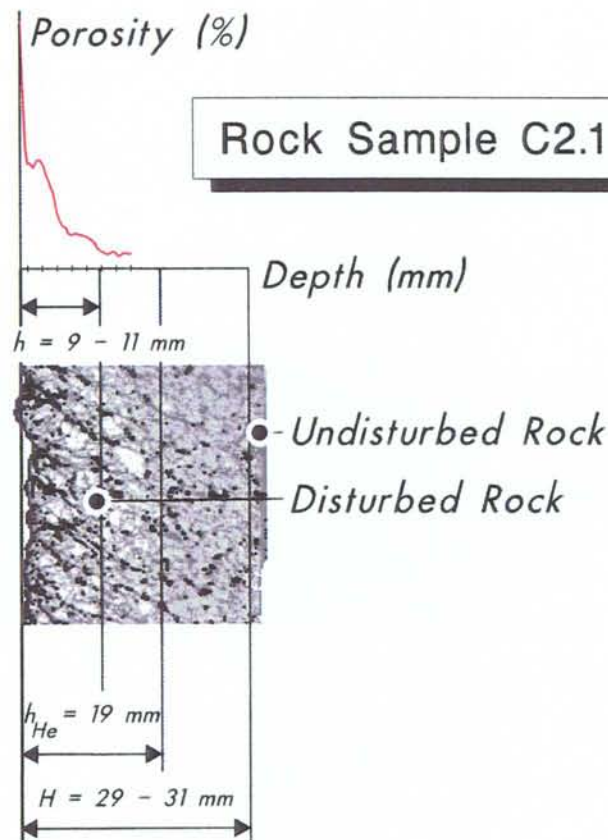
Figure 7.4-7. Cross-section of the excavation-disturbed zone showing the thickness of the zone of increased porosity (h), the thickness of the zone of extended microfractures (H) and the thickness of the zone of higher diffusion coefficient and permeability (h_{He}) determined with the He-gas method.

Table 7.4-2. Thickness of the zone of increased porosity (h), thickness of the zone of increased microfracturing (H), and thickness of the zone of increased permeability and diffusivity (h_{He}). The exposure times for the autoradiographs used to determine H are also shown.

Sample	h [mm]	H [mm]	h_{He} [mm]	t [days]
A- wall	9.25	12-18		21
B- wall	8.50	20-25	18.5	17
C- wall	10.00	20-25		21
D- wall	11.00	15-31	19.0	10
E- floor	6.00	10		21
G- floor	7.00	15		17
H- corner	11.50	25-32		17
K- corner	12.25	30-34		22

h, thickness of zone of increased porosity determined using the [14]CPMMA method

H, thickness of zone of increased fracturing determined visually using ^{14}C-PMMA method

h_{He}, thickness of disturbed zone determined using the He-gas method by Hartikainen et al. 1995

t, exposure time of the autoradioraphs

7.4.4   Structure of the disturbed zone

The structure of the disturbed zone was examined using autoradiographs produced with the ^{14}C-PMMA method, thin-section microscopy, fluorescent thin-section microscopy and scanning electron microscopy. All the methods used revealed distinct fracturing and the formation of fracture-like porous pathways.

The features which appear as darker fracture-like traces in the autoradiographs represent zones and traces of increased porosity. The structure and nature of these fractures was studied by comparing autoradiographs and the corresponding rock surfaces. A thin section was made from Sample B4 and the minerological structure of the sample as seen with the nicols crossed was compared with the corresponding autoradiograph. Furthermore the microstructure of some of the fractures in Sample B4 was studied in greater detail using a scanning electron microscope (Siitari-Kauppi 1995) to examine sections perpendicular and parallel to the disturbed surface.

It should be noted that the structure of the disturbed zone was studied in three directions since sample preparation was carried out so that three orthogonal surfaces of the samples were revealed, this is illustrated in Figure 7.4-8 and 7.4-9.

The state of fracturing in the undisturbed rock was studied for reference at a depth of 25 mm from the disturbed surface using electron microscopy and the ^{14}C-PMMA method. Using fluorescent microscopy, very few fractures were revealed below a depth of four millimetres and practically none in the undisturbed rock.
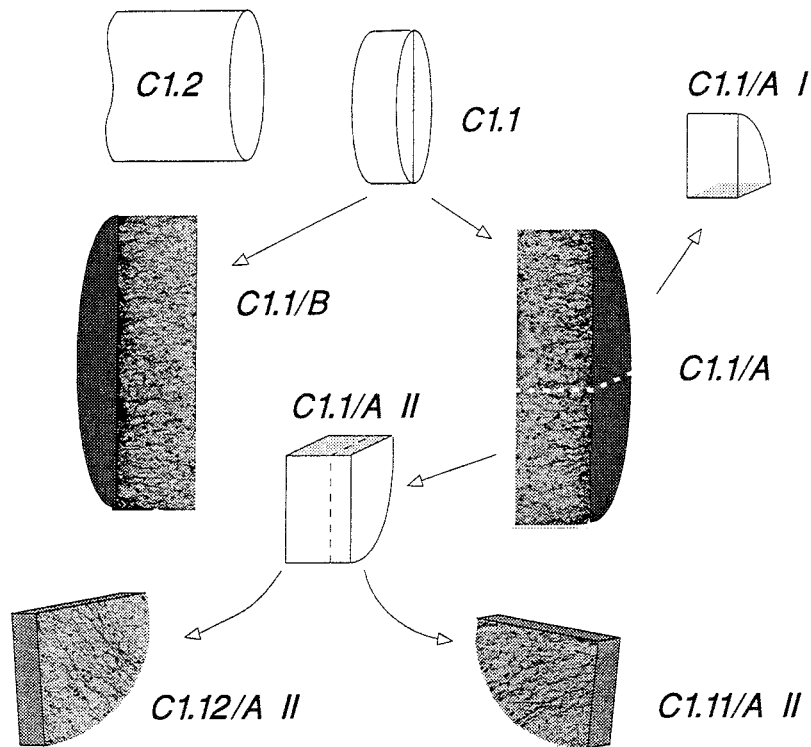
Figure 7.4-8. Preparation of Sample C1 and surfaces used for examination by autoradiography. Some of the same geometrical planes were also examined using microscopy and scanning electron microscopy.
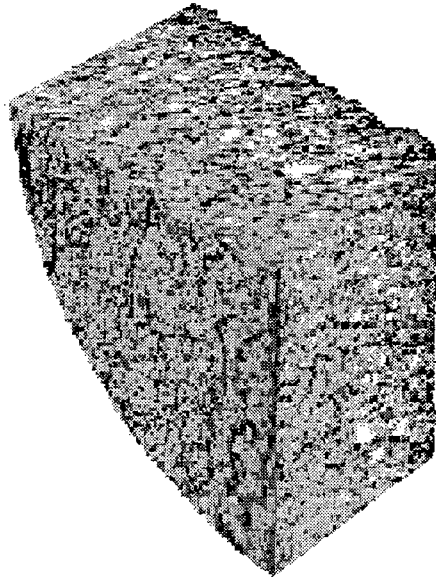
Figure 7.4-9. Block of rock reconstructed from autoradiographs of examined surfaces such as those shown in Figure 7.4-8.

The higher porosity zones in the undisturbed rock are seen in the autoradiographs primarily as dim rims which, in the main, follow the grain boundaries. Biotite grains are quite dark which indicates that they possess high intragranular porosity. Some distinct zones of plagioclase and quartz are very light which indicates low intragranular porosity, but these zones also exhibit more pronounced intergranular fracturing.

According to a SEM study of the undisturbed Sample B4.112/A at a depth of 25 mm from the disturbed surface, the felsic minerals showed almost no signs of fracturing. No fractures were visible in the quartz grains nor were the plagioclase grains transsected by fractures. The lamellae of the biotite grains in the undisturbed sample had not opened and only few intragranular fractures could be seen. The grain boundaries of the intact rock were tight and not visible at a magnification of 500x. Examples of autoradiographs obtained from undisturbed and disturbed rock are shown in Figure 7.4-10.

After studying the structure of undisturbed rock the state of fracturing in the disturbed zone was studied. The most prominent fracturing in the disturbed zone is located along the zones of mafic minerals, mainly biotite (29.6% of the total mineral composition) and hornblende (11.0% of the total mineral composition). This can be clearly seen from a section taken parallel to the disturbed surface at a depth of 5-6 mm from the surface and shown in Figure 7.4-11. The section represents rock with distinct disturbance which is seen in the autoradiograph as pathways of darker porosity (porosity zones) located in the mafic minerals, mainly biotite. The porous zones caused by fracturing in the felsic rocks are mainly in the plagioclase (37.2% of the total mineral composition). Fluorescent microscopy showed the inter- and intragranular fracturing to be intense from the disturbed surface to a depth of 3 mm in the hard and brittle minerals such as plagioclase. This can be seen later in Figures 7.4-16 and 7.4-17.

One prominent porous zone caused by fracturing similar to the ones shown in the autoradiograph in Figure 7.4-11 was further examined with SEM. Examination and comparison against the structure of mineral grains in undisturbed rock shows clearly that most of the mineral grains were fractured. Few micrometre-scale fractures were observed to transsect quartz grains although the degree of fracturing in the quartz grains was insignificant in comparison to that observed in plagioclase, biotite and hornblende, similar to that shown in the comparison in Figure 7.4-12. The plagioclase grains were observed to be transsected by large numbers of micrometre-scale fractures as well as by intragranular fissures of 500 nm or smaller aperture. Grains of biotite exhibited prominent intragranular fracturing with apertures ranging from 200 nm to 2 µm.

The geometry of fracturing was also studied in a section perpendicular to the disturbed surface. Fractures parallel to the disturbed surface were found to be a typical feature to a depth of about 2 mm from the disturbed surface. The aperture of one of these fractures which penetrated through hornblende, quartz

and plagioclase grains (shown in Figure 7.4-13) was studied closer using SEM and was found to vary between 10 and 25 μm (Figure 7.4-14).

B3.111/B

98 mm

B3.112/B

98 mm

B3.1112/A I
(9mm)

45 mm

B3.1121/A II
(23 mm)

45 mm
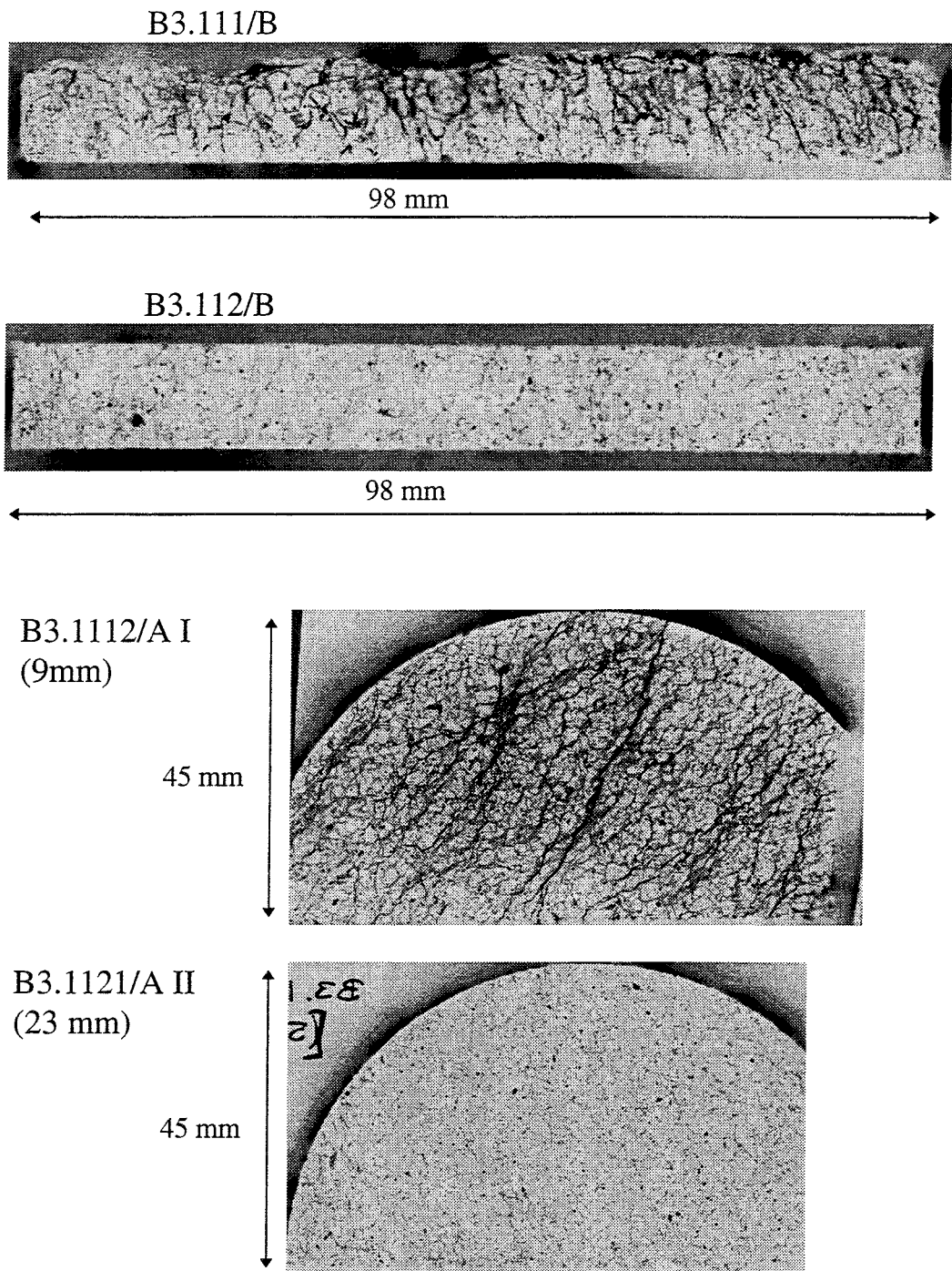
Figure 7.4-10. Autoradiographs from Sample B3 showing two sections taken perpendicular to the disturbed surface (top). The gap between the perpendicular sections is 1.5 mm. A section of disturbed rock at a depth of 9 mm and a section of undisturbed rock at a depth of 23 mm is also shown (bottom). These sections are taken parallel to the disturbed surface.
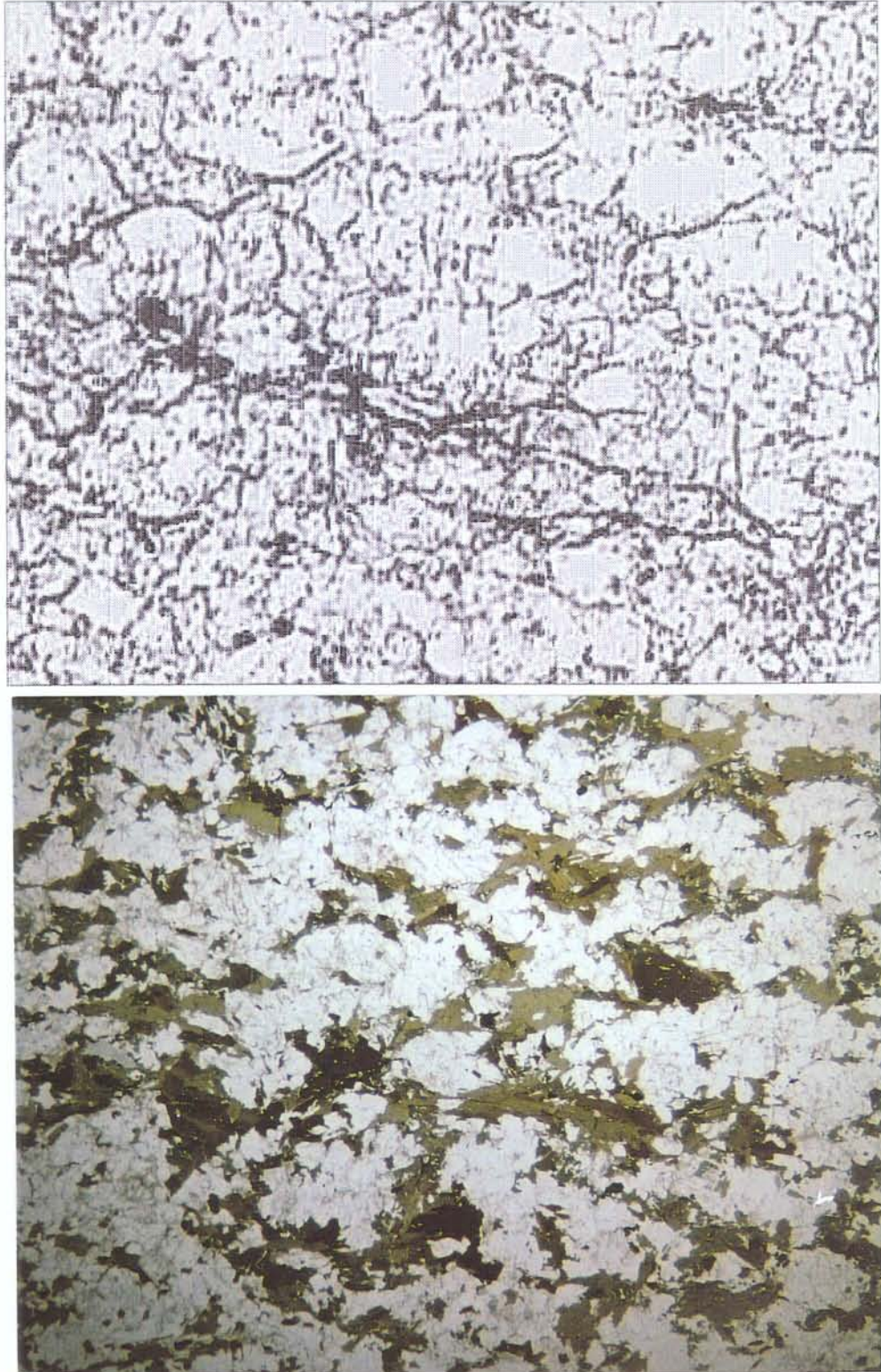
Figure 7.4-11. Autoradiograph of a section taken parallel to the disturbed surface at a depth of 5-6 mm from the surface (top) and the corresponding thin section of Sample B4.

Sample B4.1111/BI
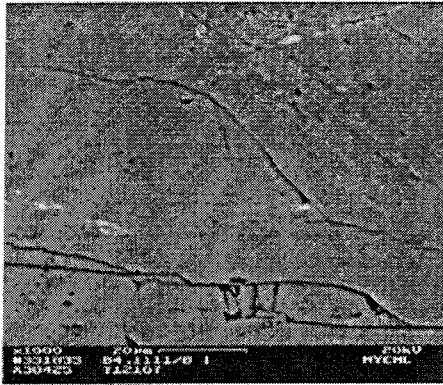
Sample B4.112/AII

Disturbed **Plagioclase**

Undisturbed **Plagioclase**
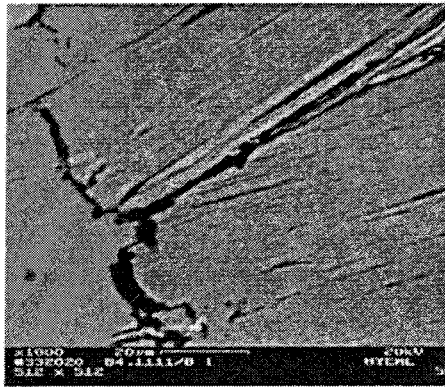
Disturbed **Biotite**
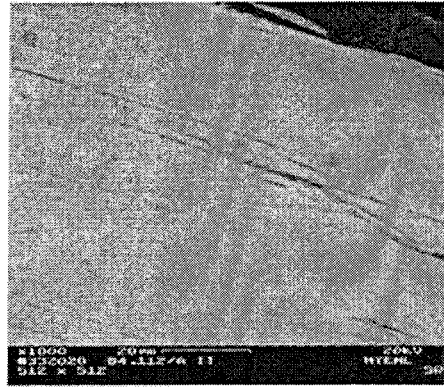
Undisturbed **Biotite**

Figure 7.4-12. BSE image of biotite grains (bottom) and plagioclase grains (top) in disturbed rock (left) at a depth of 5 mm and undisturbed rock (right) at a depth of 25 mm from the disturbed surface. The sections were taken parallel to the disturbed surface from Sample B4.

SEM section
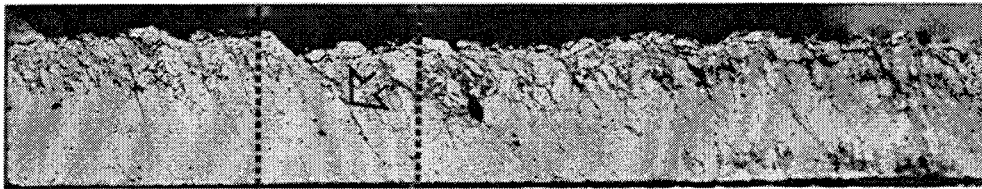
Figure 7.4-13. A porous zones caused by fractures penetrating through hornblende, quartz and plagioclase grains in autoradiograph of Sample B4 which was studied closer using SEM in the section shown.
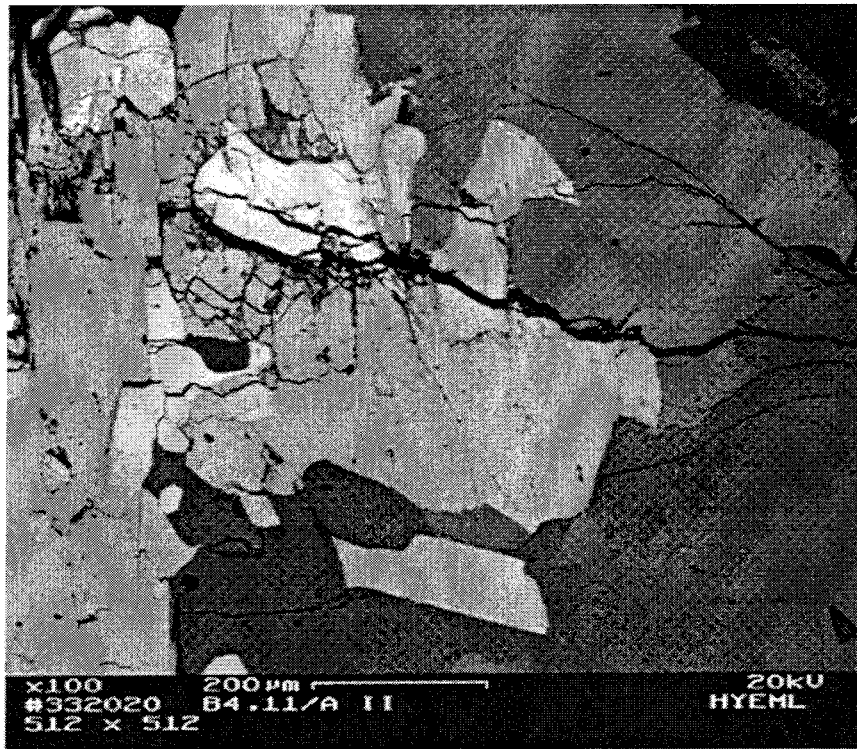
Figure 7.4-14. SEM image of the porous zone shown in Figure 7.4-13 at a depth of 0.5 mm. Magnification 100x.
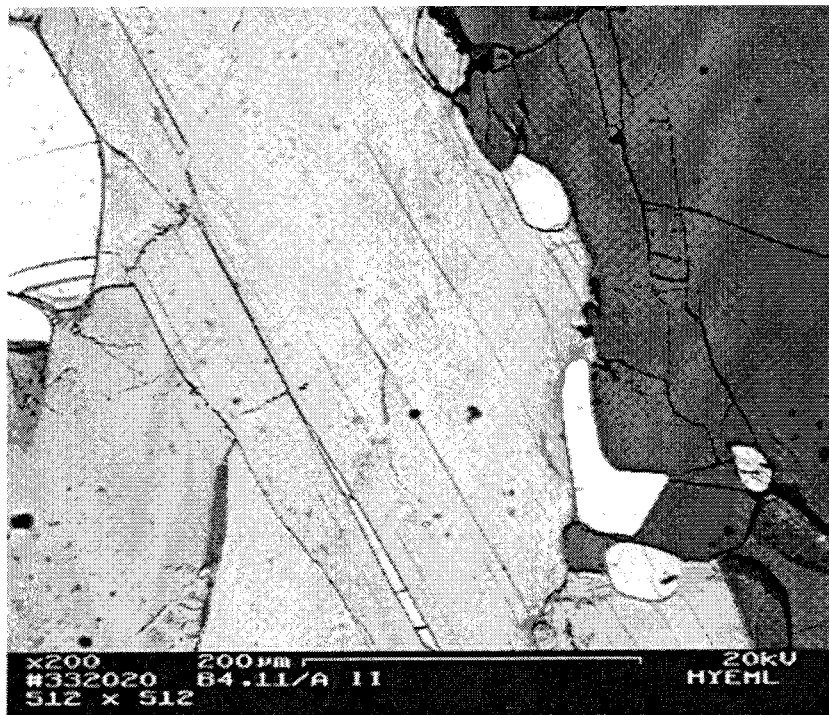
Figure 7.4-15. SEM image of the porous zone shown in Figure 7.4-13 at a depth of 5 mm. Magnification 200x.

At depths of 1 to 5 mm from the disturbed surface intense intra- and intergranular fracturing with apertures of about 1 μm was observed in all the main minerals. The grain boundaries were open.

Distinct porous zones caused by fracturing which penetrated from the disturbed surface straight or diagonally into the rock were more prominent at depths greater than 5 mm from the disturbed surface because other types of fractures became sparse and less perceptible. These fractures often follow the zones of mafic minerals. The fracture seen in Figure 7.4-13 (Sample B4.111/AII) is a set of open grain boundaries the majority of which are between hornblende and biotite. The biotite lamellae were also opened.

Fracturing in Sample C5 was studied using fluorescent microscopy. A typical example of a thin section made from the sample is shown in Figure 7.4-16. One detail of the section is shown in Figure 7.4-17 at a larger magnification. This examination showed that to a depth of about three millimetres there is fracturing with apertures of more than a few micrometres and that this is located in hard and brittle minerals, mainly plagioclase but also in quartz. The biotite flakes, which with the ^{14}C-PMMA method and SEM were both shown to be fractured, appear unfractured. This difference is most likely to be the result of the fact that the fracturing in the biotite is dense and interlamellar, with such small fracture apertures that the fluorescent epoxy used during impregnation was not able to penetrate into them.

The effect of the orientation of the rock samples was examined. No correlation was found between the orientation of schistosity and the structure and properties of the disturbed zone. This observation may partly be a result of the limited number of samples.

The characteristics of the disturbed zone differ in the floor, wall and corner sections. This study shows that the disturbed zone adjacent to the walls of the large holes can be divided according into the following sub-zones (Figure 7.4-18):

1. A crushed zone of thickness about 3 mm.

    In general, all the mineral grains in this zone are fractured. Both intra- and intergranular fracturing exists. The mafic minerals exhibit dense intragranular fracturing, whereas the harder quartz grains exhibit fewer intragranular fractures. Fracturing is perpendicular, diagonal and parallel to the surface of the hole.

2. A fractured zone extending from the crushed zone to depths of 6-10 mm from the surface of the hole. (It must be noted that the zones transform gradually and the depth shown is a very rough estimate.)

No intragranular fracturing is observed parallel to the surface of the hole. Quartz grains are undamaged. Intragranular fracturing is observed mainly in the mafic minerals. Intra- and intergranular fracturing form fracture planes which follow the orientation of schistosity. The porosity of the mafic minerals is increased. The fracturing observed has two main orientations. One is the orientation of the schistosity and the other is such that a line drawn to intersect the surface of the hole is horizontal, see Figure 7.4-19. The fractures form a honeycomb network of intersecting planes.

3. A fissured zone extending from the fractured zone in the walls to depths of 15-31 mm from the surface.

This zone contains fractures which follow the clusters of mafic minerals in the form of inter- and intragranular fracturing. The fractures start from the surface and penetrate as fracture planes into the rock following the schistosity plane. The fractures observed merge gradually into the existing intra- and intergranular fracturing and no exact point at which fracturing ends can be determined. The fractures are composed of sections in which there are more distinct fractures sandwiched between zones of smaller fracturing which are seen in the autoradiographs as zones of increased porosity. At the microscopic scale, fractures are sets of smaller fractures.
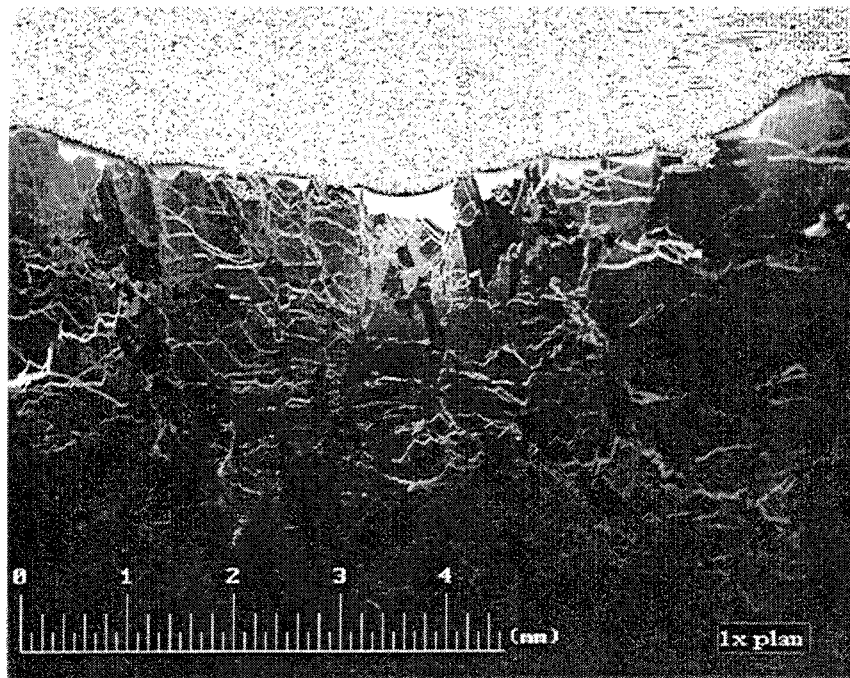
Figure 7.4-16. The disturbed surface in a thin section of Sample C5 as seen using the fluorescent microscope. The disturbed surface is at the top.
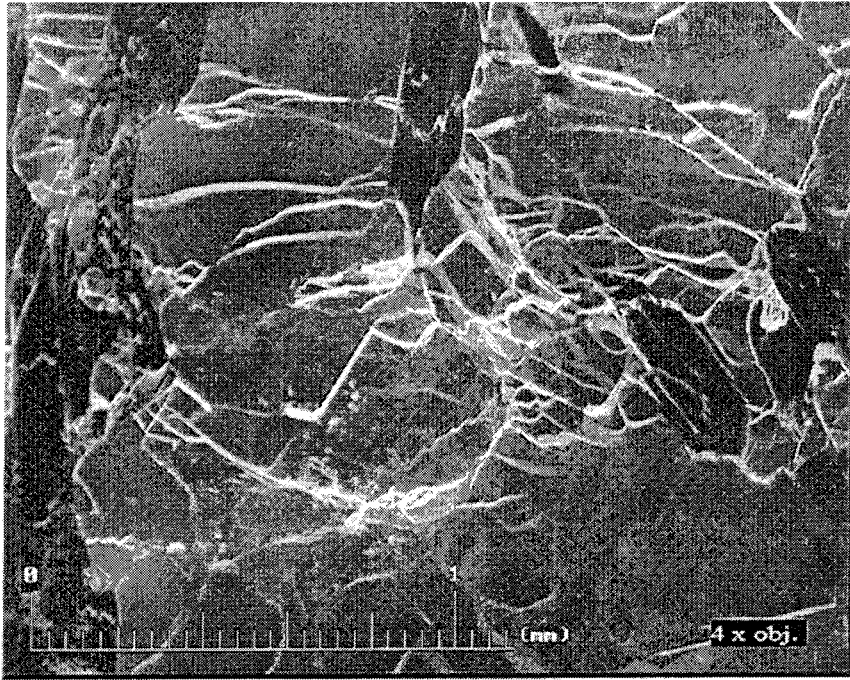
Figure 7.4-17. *The disturbed zone in a thin section of Sample C5 as seen using the fluorescent microscope. The section is a detail of Figure 7.4-17.*
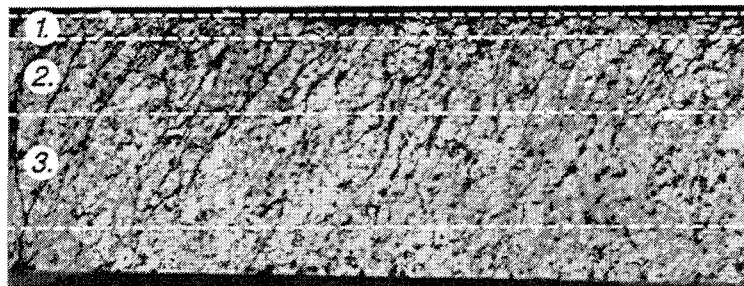
①   *Crushed zone, 3 mm*
②   *Fractured zone, 6-10 mm*
③   *Fissured zone, 15-35 mm*

Figure 7.4-18. *Structure of the disturbed zone in the wall of a large hole, vertical section from Sample C2. This sample presents the same set of samples C as the one shown partly in Figure 7.4-16. Note the difference in scale. The width of the autoradiograph is 98 mm.*

The structure of the disturbed zone was also studied at the bottom of the holes where fracturing is concentrated around the kerfs caused by the impact of the buttons on the roller cutters. All the minerals under the button impact surface is fractured to a depth of some 3 mm, see Figures 7.4-20 and 7.4-21. Fracturing is more intense under the kerfs and follows the orientation of the schistosity. Mafic minerals under the kerfs are fractured and exhibit higher porosity, presumably caused by dense intragranular fracturing.

The fracturing which starts from the kerfs follows the chistocity of the rock and penetrates below the surface between the kerfs to a depth of some 5-10 mm. Fracturing is oriented along the schistosity plane. The corner area is densely fractured and there would appear to be fractures under the corner area at depths ranging from 5-15 mm, see Figures 7.4-21 and 7.4-22.
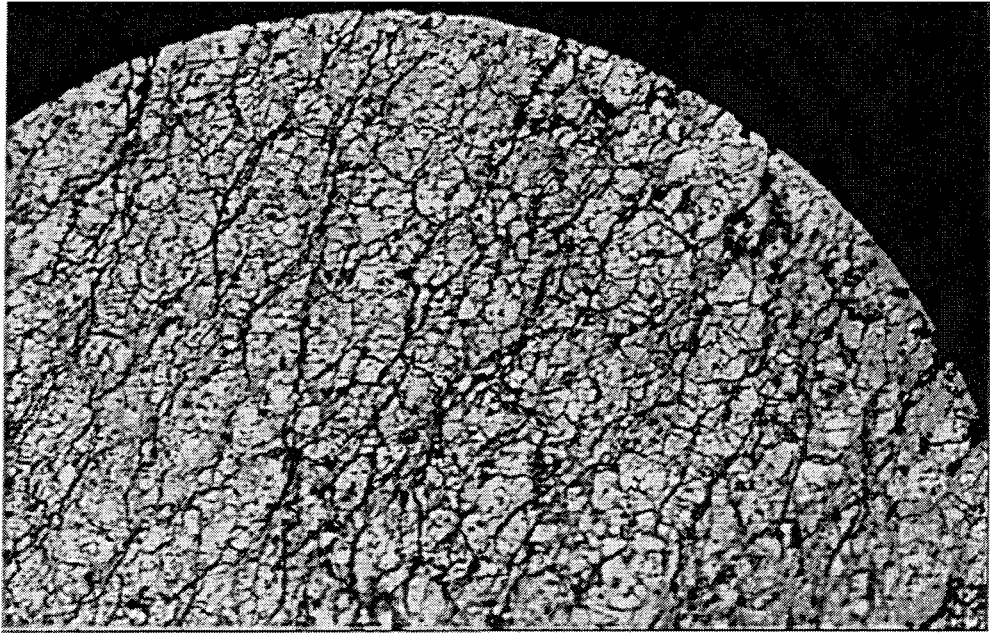
Figure 7.4-19. Direction of the fracture planes in a section parallel to the surface of the holes at depth of 7 mm (D2.1112/B).
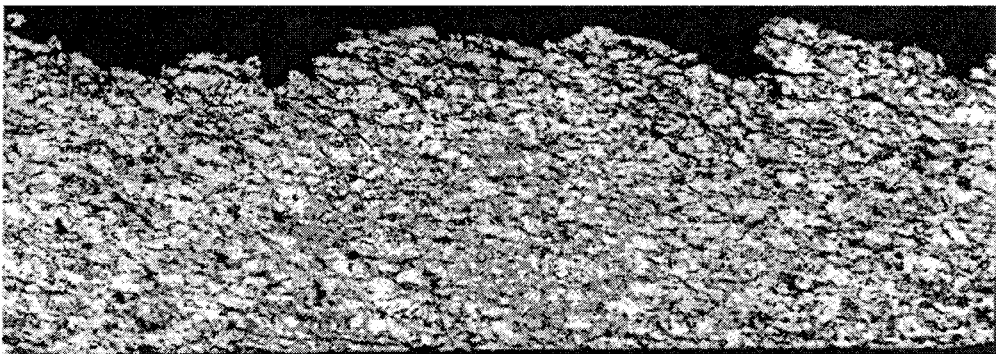
Figure 7.4-20. Structure of the disturbed zone in the floor of a large hole, vertical section from Sample E4.
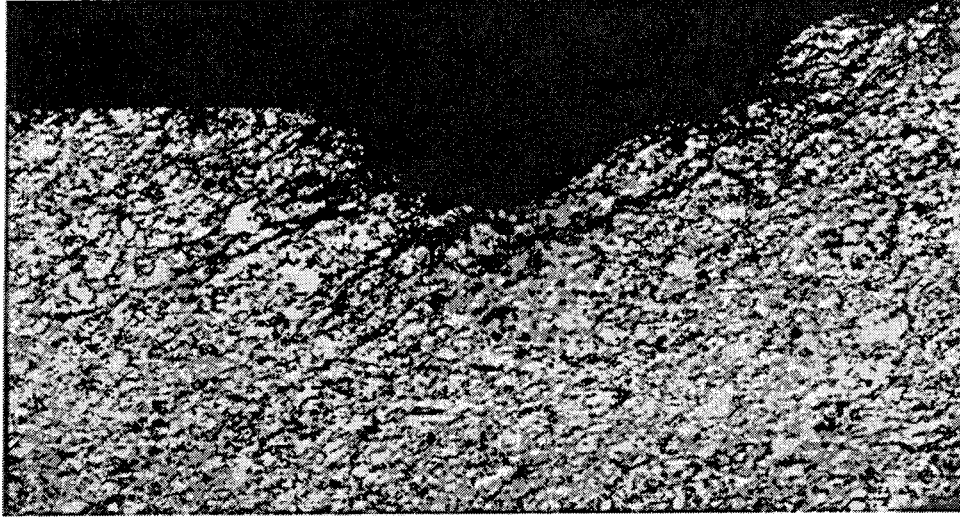
Figure 7.4-21. Structure of the disturbed zone in a corner of a large hole, vertical section from Sample K2.

737.4 kN
8.14 rpm

Sample K2.12

Sample E4.1/A
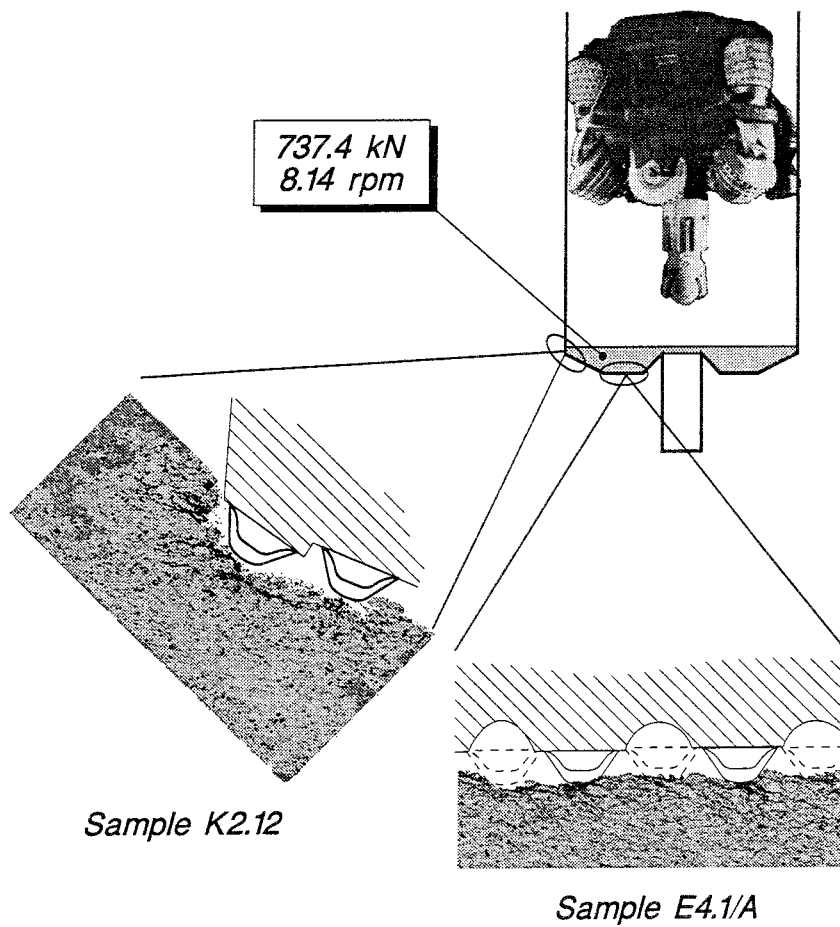
Figure 7.4-22. Structure of the disturbed zone and geometry of the hard metal buttons in the cutter head, Samples K2 and E4.

7.4.5   Permeability and diffusitivity of the disturbed zone

The permeability and effective diffusion coefficient in a direction perpendicular to the disturbed zone in the wall of the large holes was measured using the He-gas method as described in Section 7.3 (Hartikainen et al. 1995).

The measured values of permeability and effective diffusion coefficient for undisturbed rock samples from the different large holes are compatible. The average values for permeability and effective diffusion coefficient in undisturbed rock were 5.1×10^{-21} m^2 and 2.7×10^{-10} m^2/s respectively (B samples, large hole 2) and 5.2×10^{-21} m^2 and 2.6×10^{-10} m^2/s respectively (D samples, large hole 3). The hydraulic conductivity was calculated from the permeability values in accordance with d'Arcy's law and found to be an average of 5.6×10^{-14} m/s in the undisturbed samples and 3.2×10^{-12} m/s in disturbed zones of thickness from 15.5 to 17.4 mm.

The measured values of permeability and effective diffusion coefficient for samples of disturbed rock from the different holes are an order of magnitude larger than those for undisturbed rock. This can be seen in Tables 7.4.-4, 7.4-5 and Figure 7.4-23. The average values for permeability and effective diffusion coefficient in the disturbed zone were 6.8×10^{-20} m^2 and 1.6×10^{-9} m^2/s respectively (B samples, large hole 2) and 4.5×10^{-19} m^2 and 5.6×10^{-9} m^2/s respectively (D samples, large hole 3). The value of the effective diffusion coefficient for the disturbed zone in D samples is clearly larger than that for the B samples, see Figure 7.4-23. The difference in measured permeability values in the undisturbed zone was not as large.

The ratio between the permeabilities of disturbed and undisturbed rock ranged from 10 to 90, the average ratio over all samples (excluding Sample B3) being 56. Correspondingly, the ratio of effective diffusion coefficients ranged from 5 to 31 (excluding Sample B3), the average being 18.

Table 7.4-3. Results of the measurements with the He-gas method.

Samples	Undisturbed rock D_{e1} [m^2/s]	k_1 [m^2]	Disturbed zone D_{e2} [m^2/s]	k_2 [m^2]	Thickness h_{He} [mm]	Relative change D_{e2}/D_{e1}	k_2/k_1
B3	3.50E-10	5.57E-21	2.40E-08	1.13E-17	17	69	2029
B4	1.10E-10	3.60E-21	1.45E-09	7.40E-20	17	13	21
B8	3.50E-10	6.23E-21	1.70E-09	6.27E-20	20	5	10
D2	2.30E-10	4.65E-21	5.20E-09	4.00E-19	18	23	86
D4	4.00E-10	8.46E-21	7.20E-09	7.59E-19	19	18	90
D7	1.40E-10	2.47E-21	4.30E-09	1.84E-19	21	31	74
Average	2.63E-10	5.16E-21	3.97E-09	2.96E-19	19	18	56

The values for the disturbed zone in Sample B3 are are excluded from the average
D_{e1} and D_{e2}, effective diffusion coefficients of undisturbed and disturbed rock respectively
k_1 and k_2, permeability of undisturbed and disturbed rock respectively
h_{He}, thickness of the disturbed zone as determined by the He-gas method

Table 7.4-4. Summary of the results of the measurements using the He-gas and ^{14}C-PMMA method.

	Undisturbed rock	Disturbed rock	Ratio
k [m^2]	5.16E-21	2.96E-19	57
K$_H$ [m/s]	5.67E-14	3.25E-12	57
D [m^2/s]	2.63E-10	3.97E-09	18
h$_{He}$ [mm]	-	19	-
h$_{PMMA}$ [mm]	-	10	-
ε [vol. %]	0.14	0.34	2.43

k, permeability

K$_H$, hydraulic conductivity

D, effective diffusion coefficient of Helium in pore space filled by nitrogen

h$_{He}$, thickness of the disturbed zone as determined by the He-gas method

h$_{PMMA}$, thickness of the disturbed zone as determined by the ^{14}C-PMMAmethod

ε, average porosity of the disturbed zone as determined using ^{14}C-PMMA method
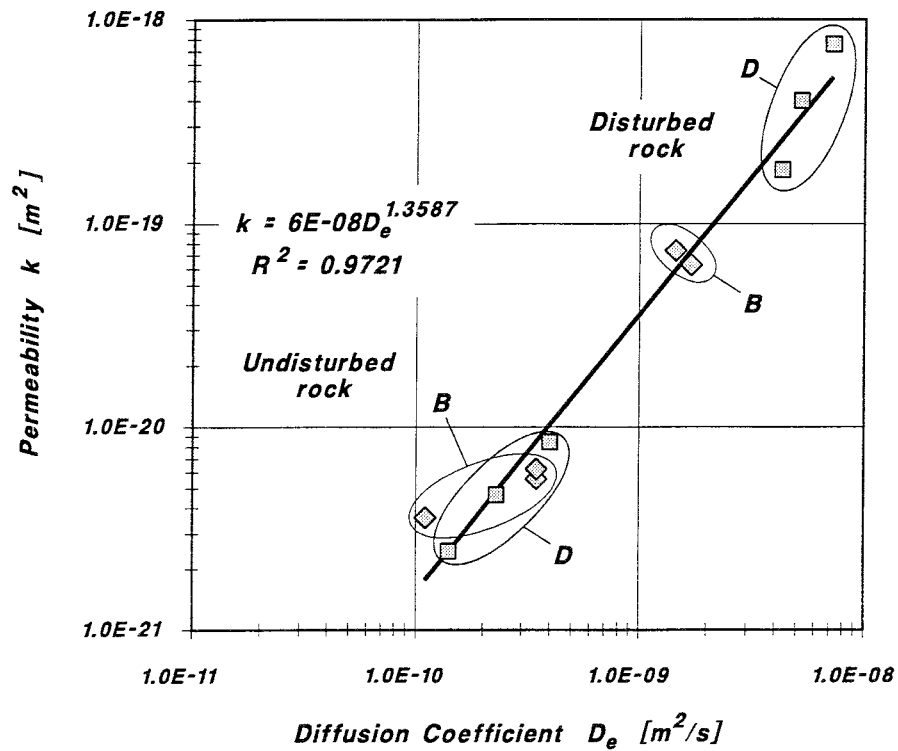
Figure 7.4-23. Measured values of permeability and effective diffusion coefficient for disturbed and undisturbed B and D samples and a regression function of exponential type.

The values obtained from Sample B3 have been excluded from the averages presented in Table 7.4-3. These results were not included when calculating the ratios shown in Tables 7.4-3 and 7.4-4 since a single fracture in the sample was judged to have a severe affect on the measurements. This is discussed in more detail in the next section.

A regression function of exponential type was fitted to the measured permeability and effective diffusion coefficients giving significant correlation with an R^2 of 0.97 (Figure 7.4-23).

The average measured value for the hydraulic conductivity of the undisturbed rock 5.5×10^{-14} m/s is at the upper margin of the results given by Domenico & Schwarts (1990). The values they present for the hydraulic conductivity of unfractured igneous and metamorphic rocks range from 3×10^{-14} to 2×10^{-10} m/s. The corresponding average value found in this work for disturbed rock (3.3×10^{-12} m/s) is in the same range.

Visual inspection of the samples showed that none of the samples contained actual fractures, with the exception of Sample B3 which exhibited a possible cleavage fracture. In general, the major contribution to porosity came from the mineral boundaries and the mafic minerals such as biotite. It can therefore be assumed that the conductive pathways in undisturbed rock samples were distributed quite evenly. This assumption is consistent with earlier characterisation of the rock around the full-scale deposition holes which indicated that all the samples of rock taken from the holes were presentative of the sparsely-fractured undisturbed rock mass between the relatively few cleavage fractures or distinct foliation planes.

The conductivity of the disturbed zone is evidently significantly higher in the first 3 mm of the zone. The result 3.3×10^{-12} m/s and 3.0×10^{-19} m^2 describes the average conductivity and permeability (respectively) of a disturbed zone of thickness 19 mm in a direction perpendicular to the disturbed surface. If it is assumed that the conductivity of the disturbed zone at depths greater than three millimetres does not differ significantly from that of undisturbed rock and that therefore the disturbed zone in the first three millimetres is dominant, a value of 1.9×10^{-18} m^2 is obtained for the permeability of the three millimetre thick disturbed zone.

The most open fracturing is found in the crushed zone and seems to be distributed evenly through the rock matrix with good connectivity between pores and fractures. The most open fractures are located in felsic minerals, mainly plagioclase. Examination showed that the connectivity between the zones of porosity in the disturbed zone beyond the crushed zone varied in different directions. The most prominent fracturing and porous zoning follows the orientation of mafic minerals and these form a diagonal network with fractures which follow the horizontal plane.

The connectivity of pores beyond the crushed zone depends on the orientation of the rock. The results obtained provide values for permeability

and diffusitivity in a direction perpendicular to the disturbed surface when rock stress and hydraulic pressure are low. According to this study, the flow paths in a perpendicular direction are quite straight and follow the orientation of the clusters of mafic minerals. The flow paths in a direction parallel to the surface beyond the crushed zone are evidently much more tortuous than those in the perpendicular direction.

The porosity and permeability of disturbed rock is affected by the level of stress in the rock and the hydraulic pressure of the groundwater, which at the planned depth of disposal holes for spent nuclear fuel will be significantly higher than that in the rock examined here. If it is assumed that the structure of the disturbed zone is the same but the state of stress is higher, both the porosity and permeability in a direction perpendicular to the disturbed surface should be reduced significantly since the relationship between stress and permeability (which is governed by the normal stiffness of the fractures) is non-linear, so that the largest reduction in aperture appears at smaller levels of stress. The structure of the disturbed zone may however be different at higher levels of stress because, for example, the disturbance induced by stress release may become pronounced with respect to the disturbance caused by the boring.

The result of measurements made on the B3 samples clearly demonstrates the effect of fractures on permeability and effective diffusion coefficient. The fracture in Sample B3 was limited in size (as described later) and did not represent a clear plane of structural weakness. The increase in effective diffusion coefficient by a factor of between 15 and 69 compared to undisturbed rock is not as dramatic as the rise in permeability (which increased by 57 to 2029 times). According to Hoek&Bray (1981) the hydraulic conductivity of rock increases by a decade, for example from 10^{-9} m/s to 10^{-8} m/s, when the number of fractures with constant aperture per metre increases from one per metre to 10 per metre. The effect of fractures opening is more pronounced since it follows a cubic law. In that respect, the measured 36-fold rise in permeability caused by single fracture is not very large.

7.4.6 The structure of samples measured with the He-gas method

The structure of samples measured with the He-gas method were examined using the ^{14}C-PMMA-method in order to characterise the connectivity and distribution of porous tracelines. The thinnest B samples which included the disturbed zone studied with both the ^{14}C-PMMA- and He-method included Sample B3.111 (thickness 12.1 mm) and Sample B4.111 (15.5 mm). The corresponding D samples included Sample D2.111 (16.9 mm) and Sample D4.111 (17.4 mm). The corresponding samples B3.112, B4.112, D2.112 and D4.112 were also studied with ^{14}C-PMMA method to characterize the structure of undisturbed rock.

The fracturing in both above mentioned sets of B and D samples was studied using the ^{14}C-PMMA method and it was observed that porous zones caused by distinct fracturing in the form of tracelines of porosity penetrated the sample mainly along the schistosity planes. The fracturing eventually merges into the natural microfracturing of the rock and it is therefore not possible to accurately determine its exact depth of penetration. In these descriptions, the term "fracture" and "'porous zone" means one or many fractures which at a natural scale appear visually as a single traceline in the autoradiograph. At microscopic scale such a line is usually composed of a set of inter- and intragranular fractures.

In the thinnest samples measured with the He-gas method the fracturing caused by boring results in a zone of dense inter- and intragranular fracturing with higher porosity from the surface of the rock to a maximum depth of about 4.5 mm and a network of fracture planes which penetrate beyond the zone of increased porosity. Fractures follow the zones of mafic minerals and there are two main fracture directions.

The most prominent orientation of the fracture planes is the same as that along which the zones of mafic minerals are oriented. The other orientation direction is such that the intersection line between the fracture and the surface of the hole is horizontal. This type of fracturing appeared to cut through sections of felsic minerals which connected zones of mafic minerals. Such fractures penetrated to a depth of over 10 mm. The distance between fractures on a plane section in a direction perpendicular to the most prominent orientation is of the order of 5 to 10 mm.

Anomalous effective diffusion and permeability values for the disturbed zone were measured from the 12.1 mm thick Sample B3.111, this indicated the existence of a faster flow path than in other samples. Use of the ^{14}C-PMMA method revealed a single, distinct, 45 mm long fracture (Figure 7.4-24) and several other less distinct fractures or zones of porosity partially intersecting the sample. It was judged that the presence of these features resulted in the anomalous values for permeability and effective diffusion coefficient. The distinct microfracture penetrates to a depth of about 10 mm towards the centre of the sample. It is probable that it penetrates further than 10 mm around the periphery of the sample. No trace of the microcrack was observed at a depth of 23 mm. The microfracture follows the orientation of the schistosity of the rock and the zonation of mafic minerals, mainly biotite and hornblende. There are several such zonation features in Sample B3.111 which penetrate to depths greater than 12 mm. It is possible that the opening of these zones was influenced by the partitioning of Sample B3.11 when it was sawn to produce Samples B3.111 and B3.112.

It was observed that in all the samples from the disturbed zone which were measured using the He-gas method there are distinct fractures, tracelines or zones of porosity which penetrate the samples partially or totally. In the cross-sections of Sample B4 shown in Figure 7.4-25 there are several fractures which appear to penetrate right through the 15.5 mm thick sample. There are

also many fractures and wider zones of porosity which penetrate to depths of about 10 mm.
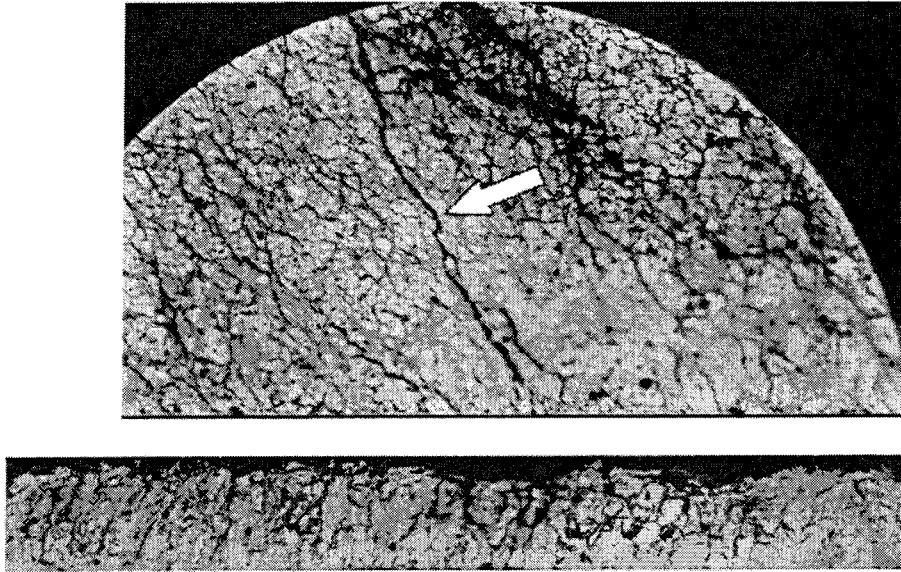
Figure 7.4-24. Autoradiograph B3.111/A (bottom) showing a cross-section perpendicular to the disturbed surface and autoradiograph B3.1112/A (top) showing a plane section at a depth of 7 mm in Sample B3.111. The microfracture which intersects the sample is shown with an arrow.
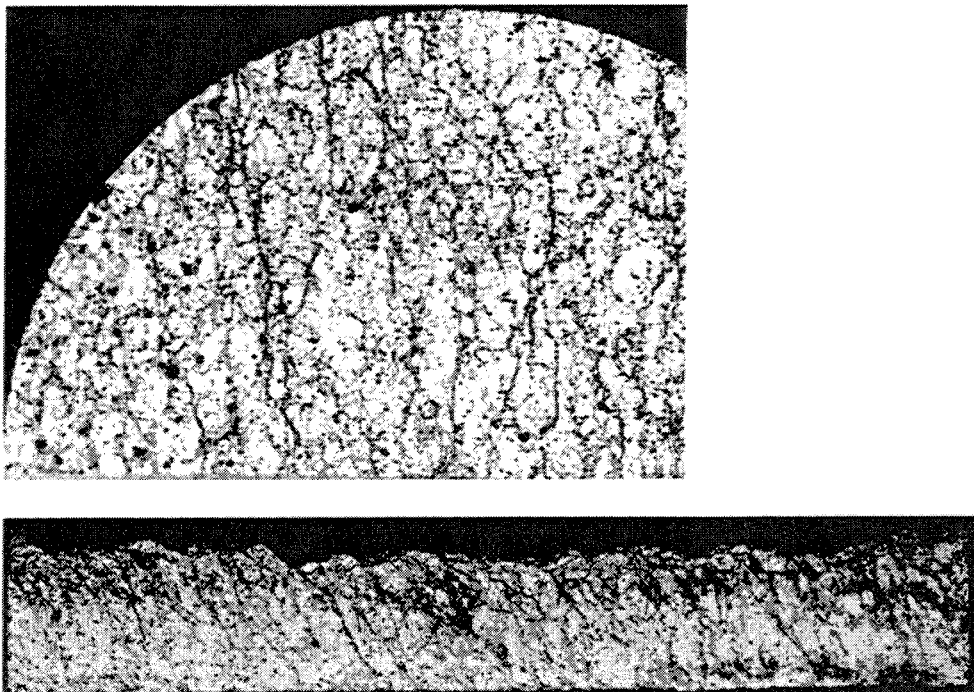
Figure 7.4-25. Autoradiograph B4.111/A showing a cross-section (bottom) perpendicular to the disturbed surface and autoradiograph B4.1112/B (top) showing a plane section of Sample B4.111 at a depth of about 7 mm.

In the cross-sections of Sample D2 shown in Figure 7.4-26 there are several fractures which appear to penetrate right through the 16.9 mm thick sample. There are also many fractures and wider zones of porosity which penetrate to depths of about 12 mm. One distinct fracture which followed a biotite zonation was seen to intersect the sample.

The cross-sections of Sample D4 shown in Figure 7.4-27 shows several fractures which appear to penetrate right through the 17.4 mm thick sample. There are also many fractures and wider zones of porosity which penetrate to depths of about 12 mm.

Figure 7.4-26. Autoradiograph D2.111/A (bottom) showing a cross-section of sample D2.111, autoradiograph D2.1112/BII showing a plane section from the same sample at a depth of about 7 mm (top) and autoradiograph D2.1121/BII (middle) showing a plane section of the undisturbed part of the sample (for reference) at a depth of about 27 mm.

Average porosity profiles for the disturbed zone in B and D samples are shown in Figure 7.4-1. In both samples there is a step at depths from 1 to 4.5 mm where the porosity remains at higher level before suddenly falling. These porosity profiles indicate that there is a zone of higher porosity in the B and D samples to a depth of about 5 mm and that the average total depth of the zone of increased porosity is about 9 mm for the B samples and 11 mm for the D samples. This could explain why the measured values for both permeability and effective diffusion coefficient were higher in the D samples than in the B samples.
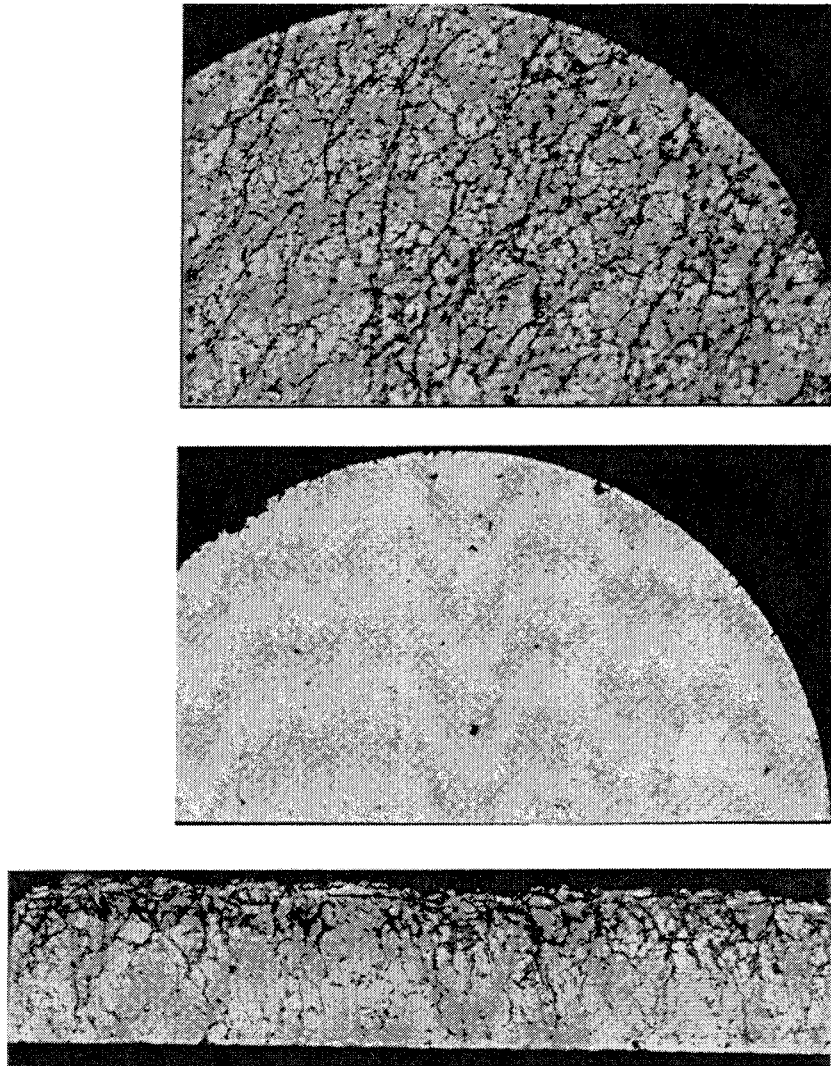

Figure 7.4-27. Autoradiograph D4.111/B (bottom) showing a cross-section of Sample D4.111 perpendicular to the disturbed surface and autoradiograph D4.1112/A (top) showing a plane section from the same sample at a depth of about 6 mm.
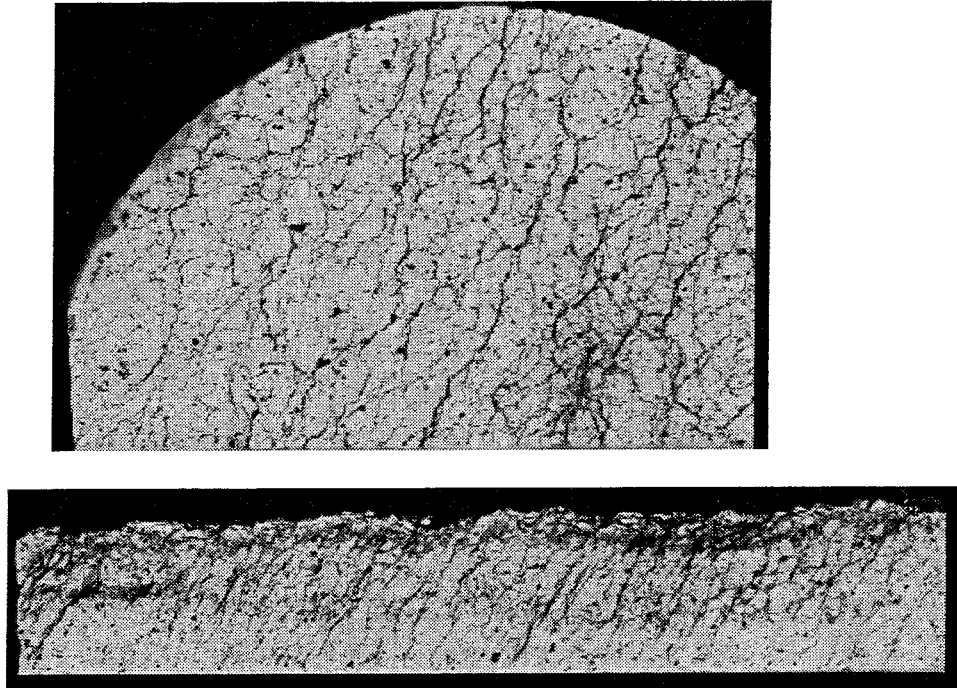
7.5 OTHER OBSERVATIONS AND EVALUATION OF THE METHODS

7.5.1 Sample preparation

The ^{14}C-PMMA method and fluorescent microscopy did not reveal any noticeable disturbance caused by the activities of coring or sawing during sample preparation. It is possible that the fracture observed in the 12 mm thick Sample B3.111 was activated by the process of sample preparation. It is however assumed that the primary cause of the fracture was not sample preparation since the permeability value of Sample 3.11 had already been measured to be higher than average before the sample was sawn to its final thickness.

The autoradiograph of a core sample taken from investigation core hole KR7 (located along the centreline of large hole 3) showed some lamella-type fracturing along grain boundaries which could have been caused by the core sampling process since a similar type of microfracturing was not observed in other larger diameter samples of the same rock except in a few sections situated close to sawn surfaces.

7.5.2 He-gas method

The He-gas method proved to be quite fast and useful when determining the effective diffusion coefficient and permeability of large samples of rock. The diameter of the 98 mm samples was about one hundred time greater than the size of the mineral grains and the sample included a large number of structural features which might have hampered measurement and caused significant variation in results if a smaller sample size had been employed. The initial thickness of the samples ranged from 56 to 59 mm. The longest period required for through-effective diffusion measurement (which occupies more time than the measurement of permeability), was less than two days and included measurement of the tail section of the breakthrough pulse of helium. There is no other method currently available which could be used to determine the properties of this size of sample in the same time period.

One of the major issues related to the exploitation of the method is the accuracy which can be achieved when the results are converted to hydraulic conductivities and effective diffusion coefficients of helium in pore space filled with water.

The conductivity of helium gas conductivity measured by using He-gas method, in principle according to d'Arcy's law, was first converted to permeability, which is a material property of the medium and does not depend on the properties of the fluid. The permeability can then be converted to hydraulic conductivity, K_h, using the following expression

$$K_h = k\,(\rho_w g/\mu) \hspace{4cm} 7\text{-}1$$

, where K_h is the hydraulic conductivity (m/s)

           k is the permeability (m^2)

           ρ_w is the density of water (kg/m^3)

           μ is the viscosity of water ($kg/(m{\cdot}s)$)

           g is the acceleration due to gravity (m/s^2)

The expression can be derived from d'Arcy's constant of proportionality by making the d'Arcy's law equivalent to Hagen-Poiseuille equation (Domenico & Schwartz 1990, p. 62), which is of common recognition in the field of physics and hydrology.

It is assumed in derivation of the expression 7-1 that the flow can be conceptualised to take place in a porous media along a bundle of parallel capillary channels and the flow process is laminar and governed by viscous forces only. The dimensionless characteristic parameter, Reynold's number, describes the ratio of inertial forces (acceleration of water particles) to frictional forces (friction with boundaries, viscous forces) in the flow. The viscous forces depend on the viscosity of the fluid and velocity and inertia forces depend on the density and the square of the velocity of the fluid.

It is assumed in the conversion from helium conductivity to hydraulic conductivity that the flow rates in the He-gas measurements have been low enough and therefore the Reynold's numbers are low, in the regime of laminar flow. Therefore, it is assumed that the hydraulic conductivity can be calculated in the manner described without a significant error.

The properties of flow depend on the structure and fluid paths in the medium and, strictly speaking, the expression 7-1 is valid if the flow pattern in the rock is the same for both fluids, helium and water. The flow velocities and flow patterns were not studied in a quantitative manner and the estimates may be somewhat inaccurate. It is suggested that the accuracy of the estimates should be studied more in detail in the future.

The effective diffusion coefficient of helium in water filled pore space was calculated by scaling the values from the measured effective diffusion coefficient of helium in nitrogen gas filled pore space by the ratio of the effective diffusion coefficients of helium diffusing in nitrogen gas to the diffusion coefficient of helium diffusing in water. It was assumed that the porosity pattern in the rock was the same for both conditions (as filled with water or nitrogen gas) and that the Brownian movement of the particles was the same. As long as the free path length of the helium atoms is clearly smaller than the size of the pores in the medium the scaling should be valid.

Since both the flow of water and effective diffusion through a rock sample are complicated processes it would be beneficial to carry out measurements on the same samples with both water and Helium. Samples with higher conductivity such as the sections from the crushed zone should be used

since the time required to measure the diffusion of water through larger permeable samples is very long, especially if the tail section of the breakthrough curve is measured in the same manner as that used in the He-gas method.

The He-gas method was not found to be accurate when determining the porosity of the samples as described by Hartikainen et al. 1995. The method gave the same porosity for both the disturbed zone and intact rock zone of Sample B4. In the case of Sample B8 the porosity of disturbed zone, which evidently is higher then the porosity of intact rock, was found to be lower than the porosity of the intact sample. One reason for the modest accuracy is probably that the interpretation of measured data is quite insensitive to porosity. Average porosities measured for both the disturbed (0.09%) and undisturbed zone (0.06%) measured by using the He-gas method were significantly lower than corresponding values (0.31-0.38% and 0.14%) determined by using the ^{14}C-PMMA method.

The structure of the rock is composed of three different zones and interpretation of the results with a three-zone material model would most likely correspond better to the real structure since the properties of the most fractured surface zone are obviously significantly different from those of rock in the deeper sections of the disturbed zone.

Through-flushing of the samples with nitrogen was used for drying since earlier experimental data had indicated that it would give sufficiently good results. As experience has showed that nitrogen flushing is a practical way to dry the samples it is suggested that the drying effect should be studied in a profound way.

It is possible that the sawing of thin samples changes the properties of the samples. This could be caused by the force exerted by the saw blade, by the release of residual stresses in the rock sample, or by a combination of these effects. It is recommended that the use of thin samples be avoided until the effect of sample preparation has been studied using thicker reference samples.

7.5.3 ^{14}C-PMMA method

The ^{14}C-PMMA method was found to be a feasible and efficient tool for the study of rock structure. It effectively fills the gap between macroscopic and microscopic investigation methods. In addition to this it gives quantitative information about nanometer range porosity which is beyond the scope of most standard methods of microscopic investigation.

The ^{14}C-PMMA method had not been previously been used to study rock samples exhibiting a large porosity range and the following problems were encountered. To achieve a similar level of accuracy when determining porosity, the exposure time for the autoradiograph has to be chosen

according to whether interest is focused on a low porosity section, such as when investigating the depth of disturbance, or on a high porosity zone such as the crushed zone adjacent to the disturbed surface. The grey intensity/porosity scale is non-linear and therefore the accuracy of porosity information at higher levels of porosity is reduced if longer exposure times are used to get more accurate information about low porosity. The use of two different exposure times is therefore recommended.

In some of the autoradiographs anomalous zones of porosity were found. Because of the small number of measurements it is recommended that repetitive measurements are made. This will allow such an observation to be verified and to eliminate any possible artefacts, factors of great importance if the anomalous zones should prove to be a true structural feature.

Autoradiographs are sensitive to the surface smoothness of the profiles being examined and this caused some inaccuracies in the case of some samples. It is recommended that the sample preparation technique be developed further.

The rectangular sections including the disturbed surface used to determine the porosity profile were determined by hand and visual inspection. Sections of large surface roughness were divided into separate smaller sections. It would be beneficial to automate the sectioning procedure although this would not solve the problem of which plane should be used as an unambiguous reference. The inaccuracy in the elevation of the disturbed surface causes an inaccuracy of less than one millimetre in the depts estimates of the disturbed zone.

The combination of the ^{14}C-PMMA method and scanning electron microscopy (SEM) was found to be a powerful tool which covered the scale from macroscopic to microscopic and included good mineral separation properties. Since SEM is a elaborate and slow method of investigation, the use of fluorescent microscopy is recommended when characterising larger scale fractures.

Determination of the depth to which porous zones penetrated into the undisturbed rock was carried out by visual inspection. This procedure was compromised both by the subjectivity of visual determination and the differences in autoradiographs caused by the use of different exposure times. It is recommended that new autoradiographs are produced using constant exposure times when determining zone depths. To avoid the subjectivity caused by visual assessment, image analysis techniques could also be exploited when determining the depth of different zones.

8 RELATIONSHIP BETWEEN BORING TECHNIQUE AND THE PROPERTIES OF ROCK IN THE DISTURBED ZONE

Disturbance in the rock was examined in relation to cutter type and thrust on the cutter head by considering the average additional porosities ε_d, and $\varepsilon_{d,1.5\text{-}h}$, the depth of the zone of increased porosity h, and the additional pore volume per surface area V_d and $V_{d,1.5\text{-}h}$, as described in Section 7.4.2. Figures for these values are given in Table 7.4-1. Values for thrust on the cutter head, thrust per button row and the corresponding penetration rate of the cutter head are given in Table 8-1 for all the sample sets (A, B, C and D) taken from the walls of the large holes. Thrust per button row was calculated in order to allow comparison with the disturbance caused by other types of cutters and cutter interlacings (Autio & Kirkkomäki 1996a and b). Since, as shown in Figure 8-3, the total thrust on the cutter head and the cutter head penetration rate are well correlated (Autio & Kirkkomäki 1996a and b), in principle these define the same variable.

The formation of a disturbed zone is only one of the rock-breaking processes which take place during boring. Most of the energy used to crush rock during the boring process is spent below the cutter head and depends on the geometry of the hard metal buttons in the roller cutters, the spacing of rows in the cutters and the cutter interlacing.

Gauge rollers

Outermost button row
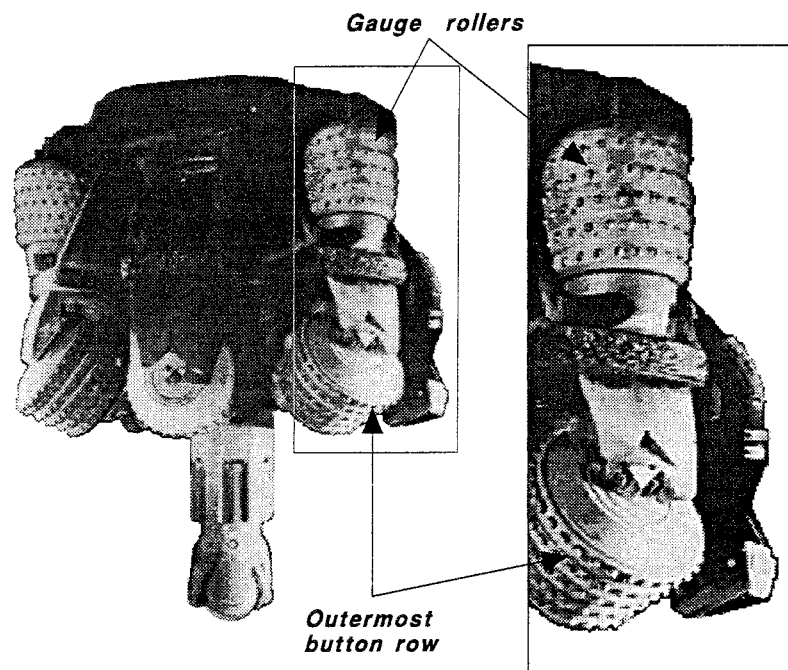
Figure 8-1. The cutter head. The insert shows the cutting tools, gauge rollers and outermost button row of roller cutters which contact the rock surface and affect the properties of the disturbed zone.

The disturbance which appears as fracturing in the rock is caused by a series of indentations caused by the impact of the hard metal buttons in the rolling cutters. The cutter buttons which are in contact with the rock and which affect the disturbance are the outermost row of buttons in the cutter head and the gauge rollers (Figure 8-1). The fractures are caused in the disturbed zone adjacent to the wall of the hole by a large number of closely placed button indentations exerted on the prefractured corner section of the hole, Figure 8-2. The number of indentations per unit of surface area depends on the penetration rate of the cutter head and the cutter interlacing. The number of outermost cutter rows in each series was four. The minimum vertical distance between succeeding indentations at a penetration rate of one millimetre per rotation was therefore 0.25 mm.

The gauge cutters shown in Figure 8-1. were adjusted so that they contacted the rock in a sporadic fashion. The contact areas could be distinguished on the basis of surface roughness. When taking samples to characterise the extent of disturbance in the rock, sections where the gauge cutters had contacted the rock were avoided.
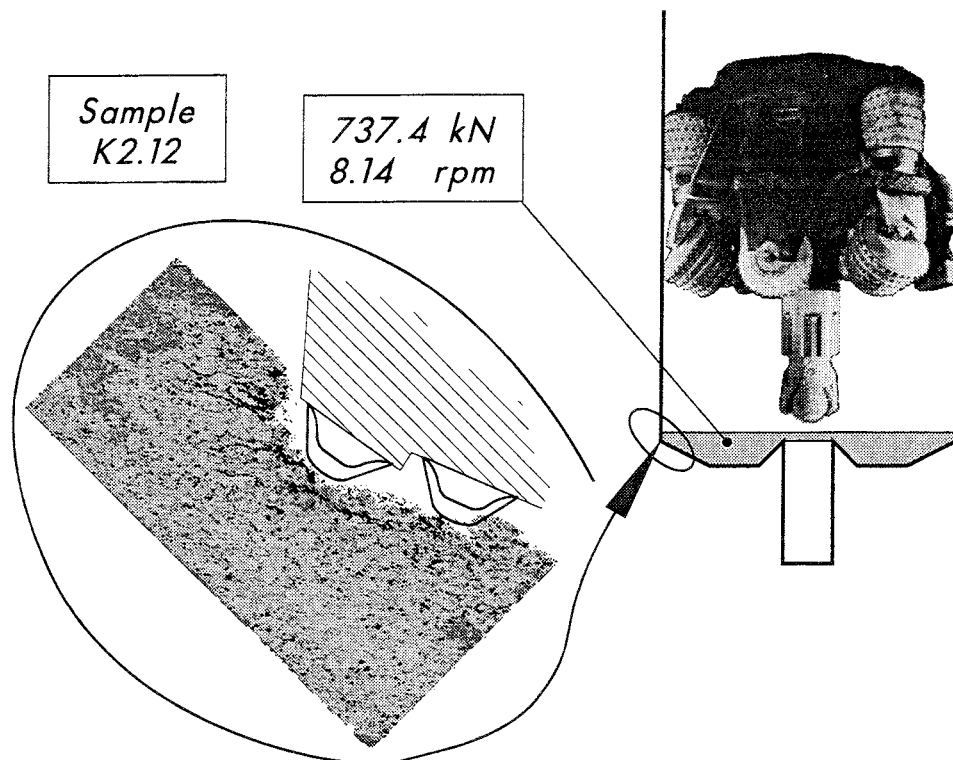
Figure 8-2. Indentations resulting from the impact of the outermost button rows and the resultant crushing force affects the extent of disturbance caused in the rock.

Samples A and B from large hole 2 are representative of the same rock-cutting technique using cylindrical diameter 19 mm buttons (see Chapter 2, Figure 2.3-4). Samples C and D from large hole 3 are representative of rock cutting with cylindrical diameter 21 mm buttons (also shown in Figure 2.3-4). The samples A are representative of boring at a lower level of thrust than the samples B (large hole 2) and the same applies to samples C and D (large hole 3) correspondingly.

Disturbance in the rock was examined in relation to cutter type and thrust by considering average additional porosities ε_d and $\varepsilon_{d,1.5\text{-}h}$, depth of the zone of increased porosity h and additional pore spaces per surface area V_d and $V_{d,1.5\text{-}h}$ as described in Section 7.4.2 and given in Table 7.4-1. The thrust, thrust per button row and the corresponding penetration rate of the cutter head is given in Table 8-1 for all sets of samples A, B, C and D taken from the walls of the large holes. The thrust per button row was calculated in order to make comparisons with the disturbance caused by other types of cutters and cutter interlacing (Autio & Kirkkomäki 1996a and b). Since the total thrust on the cutter head and the cutter head penetration rate are correlated (Autio & Kirkkomäki 1996a and b) as shown in Figure 8-3, in principle these describe the same phenomena.

Figure 8-4 shows values for the additional pore volume in the disturbed zone (V_d) with respect to total thrust on the cutter head. The degree of disturbance is clearly greater at higher levels of thrust. The level of disturbance in the C and D samples (bored with a 4- and 5-row cutter arrangement) is also greater than in the A and B samples (bored with a 5- and 6-row cutter arrangement). The degree of disturbance with respect to thrust per button row indicates a similar trend (see Figure 8-5).

Both higher levels of thrust and the 4- and 5-row cutter arrangement appear to increase the level to which the rock is disturbed, but the difference in degree of disturbance between the two types of cutters is not as clear when considered in relation to thrust per button row as when considered in relation to total thrust on the cutter head.

Table 8-1. Total thrust, the corresponding thrust per button row, and cutter head penetration rate for sample sets A, B, C and D.

Samples	F_b [kN/row]	F_T [kN]	i[mm/rev.]
A- wall	7.33	547	1.27
B- wall	8.17	610	1.43
C- wall	7.35	413	0.82
D- wall	13.1	737	1.67

F_b, thrust per button row
F_T, total thrust of the cutter head
i, penetration rate of the cutter head
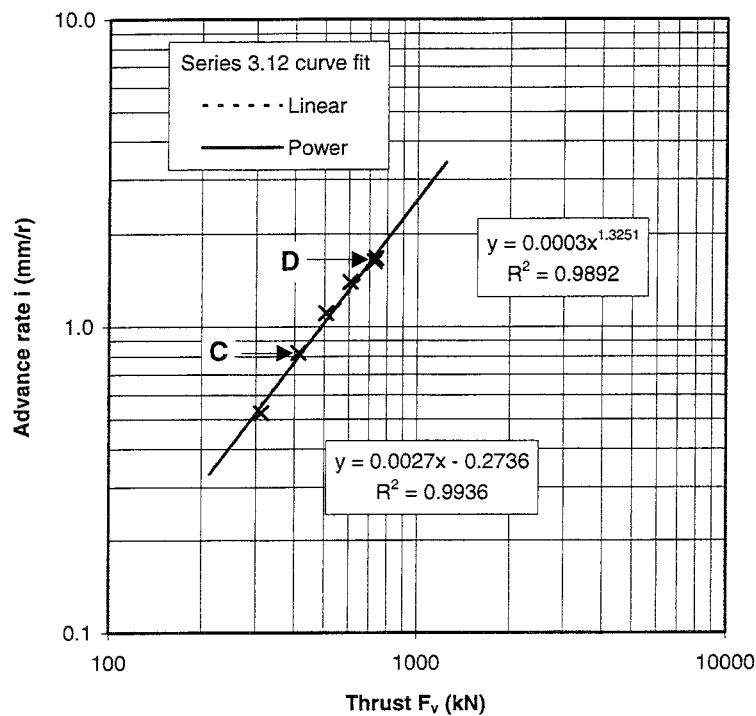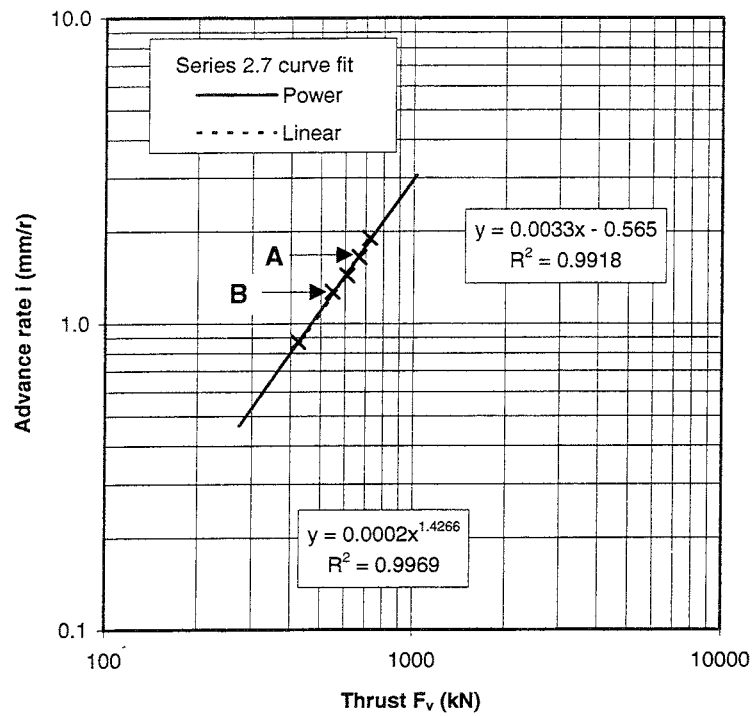
Figure 8-3. Advance rate as a function of thrust for sample sets A, B C and D. Test 2.7 is representative of the boring of samples A and B (rotation speed 8 rpm, 5- & 6-row cutters). Test 3.12 is representative of the boring of samples C and D (rotation speed 8 rpm, 4- & 5-row cutters).
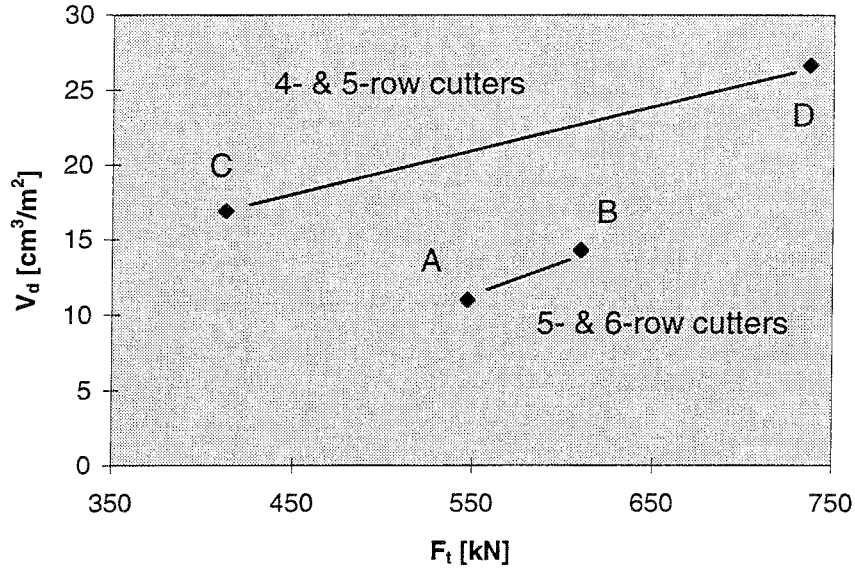
Figure 8-4. Total additional pore space from the disturbed surface to a depth where the porosity falls to the level of that of undisturbed rock (see Section 7.4.2 for an explanation) plotted against the total thrust on the cutter head. Note that the values A and B represent different type of cutters to the values for C and D.
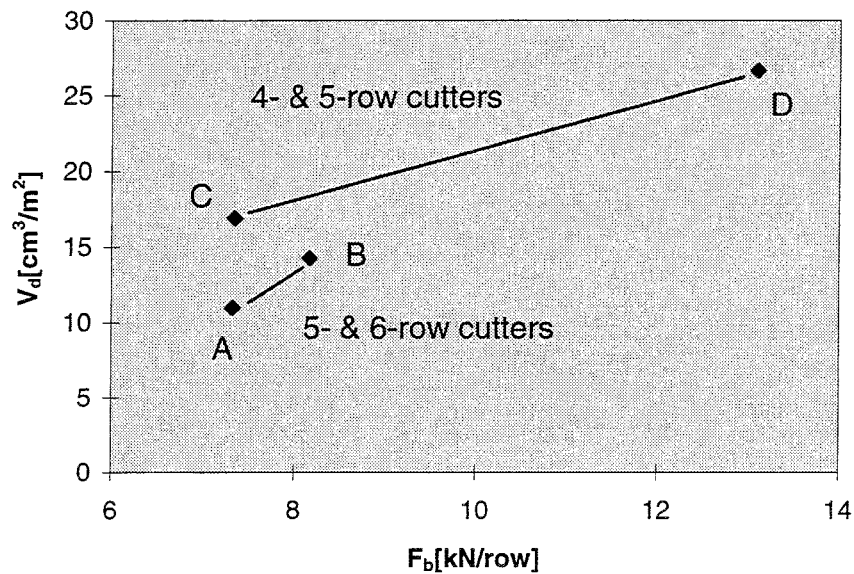
Figure 8-5. Total additional pore volume from the disturbed surface to a depth where the porosity falls to the level of that of undisturbed rock (see Section 7.4.2 for an explanation) plotted against thrust per cutter button row. Note that the values for A and B represent a different type of cutter to the values for C and D.

The additional total pore volume in the disturbed zone $V_{d,1.5-h}$ (from a depth of 1.5 mm from the disturbed surface to a depth where the porosity reaches the level of undisturbed rock) when related to the thrust employed during boring reveals clear differences between both the different cutter arrangements and the different thrust values employed (see Figure 8-6). Similar features can be seen in Figure 8-7 in relation to the calculated thrust per button row.

The degree of disturbance caused is clearly greater at higher levels of thrust. The results obtained also suggest that the disturbance caused by the 4- and 5-row cutters used in the boring of large hole 3 is more pronounced than the disturbance caused by the 5- and 6-row cutters used in the boring of large hole 2.

In general, all the parameters shown in Tables 7.4-1 and 7.4-2 are indicative of greater disturbance in sample sets B and D (which represent higher levels of thrust) than in the corresponding sample sets A and C (which represent lower levels of thrust) and this observation is supported by Figures 8-4, 8-5, 8-6, 8-7 and 8-8. The difference in the degree of disturbance caused by the different type of cutters and the associated differences in button row positioning is also clear, even though the degree of disturbance caused by the 4- and 5-row cutter arrangement is not significantly higher than that caused by the 5- and 6-row cutter arrangement. It should be noted that differences in the degree of disturbance not only result from the differences in the actual size of the cutters, but are also caused by the positioning of the cutter rows, which results in a different distribution of thrust between the individual button rows.

The differences resulting from the use of different cutter arrangements and levels of thrust on the cutter head can also seen in the measurements of permeability and diffusion coefficient. Values obtained (see Section 7.4.5) for the B samples, which represent lower levels of thrust and use of the smaller 5- and 6-row buttons, were lower than corresponding values obtained for the D samples, which represent the use of larger 4- and 5-row buttons at higher levels of thrust.

The results of this work show that the extent of the disturbed zone can be influenced by redesign of the cutter head and, in particular, by modification of the outermost button rows in the cutter head since these are the ones which primarily affect the characteristics of the disturbed zone. According to these results, the larger the thrust per button in the outermost button row and the higher the penetration rate of the cutter head, the greater the degree of disturbance caused. The same applies to the size of the buttons themselves. The larger the button diameter, the greater the degree of disturbance caused.
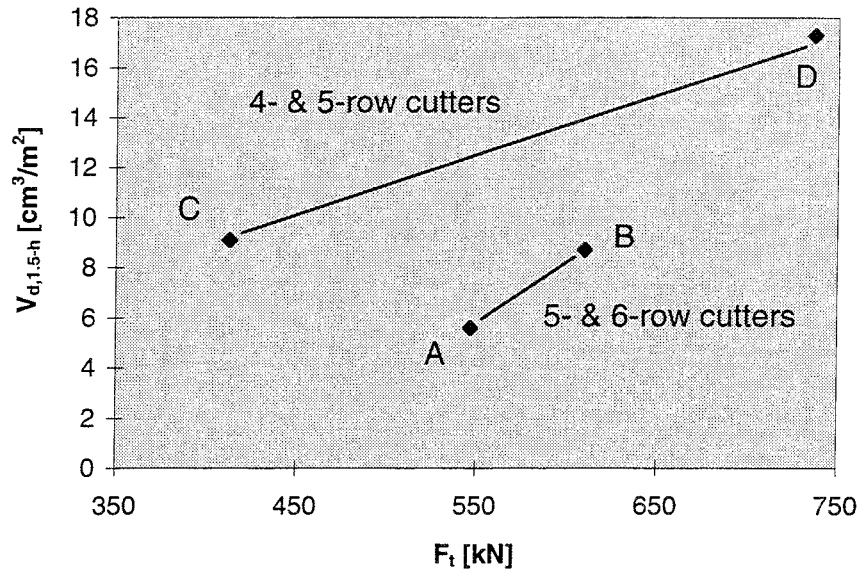
Figure 8-6. Total additional scaled pore volume *from a depth of 1.5 mm from the disturbed surface to the depth at which porosity falls to the level of that of undisturbed rock (see Section 7.4.2 for an explanation) plotted against total thrust on the cutter head. Note that the values for A and B represent a different type of cutter to the values for C and D.*
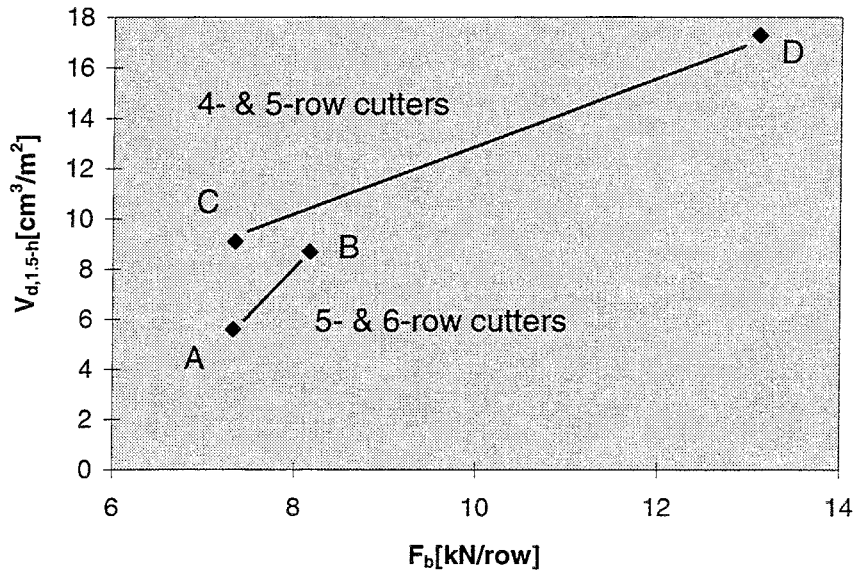
Figure 8-7. Total additional pore space from a depth of 1.5 mm from the disturbed surface to a depth where the porosity reaches the level of undisturbed rock (see Section 7.4.2 for an explanation) plotted against the calculated thrust per button row. Note that the values for A and B represent a different type of cutters to the values for C and D.
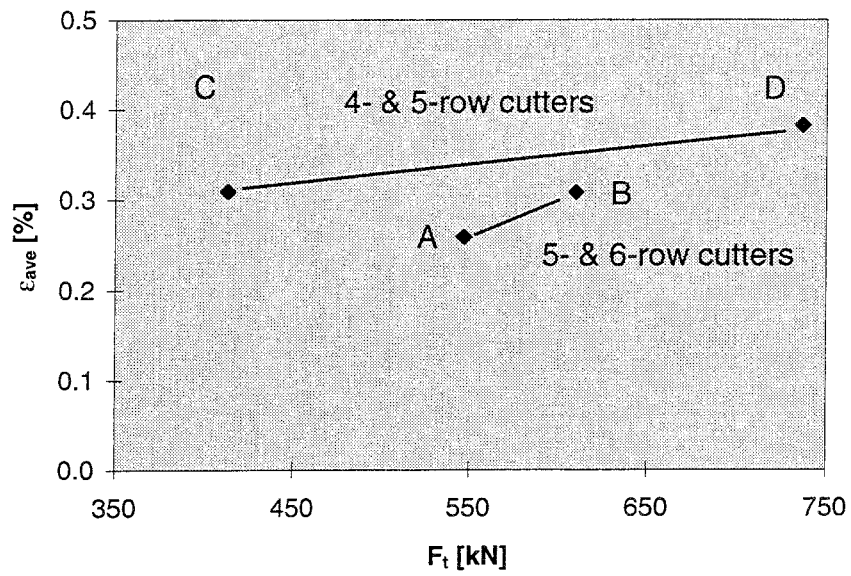
Figure 8-8. *The average porosity of the disturbed zone of thickness h (see Section 7.4.2 for an explanation) plotted against the total thrust on the cutter head. Note that the values for A and B represent a different type of cutters than the values for C and D.*

9   SUMMARY AND CONCLUSIONS

Characterization of the excavation disturbance caused by boring of the experimental full-scale deposition holes in the Research Tunnel at Olkiluoto was carried out successfully. New methods were employed and new information was obtained about the properties of the disturbed zone caused as a result of boring.

The ^{14}C-PMMA and He-gas methods were modified and applied for the first time in this type of study and were found to be useful. Some areas for future development work were identified.

The measured values of permeability and effective diffusion coefficient for disturbed rock samples from the different large holes were an order of magnitude larger than those for the undisturbed rock. The average values for permeability and effective diffusion coefficient in the disturbed zone were 6.8×10^{-20} m^2 and 1.6×10^{-9} m^2/s in B samples (large hole 2) and 4.5×10^{-19} m^2 and 5.6×10^{-9} m^2/s in D samples (large hole 3) respectively. The effective diffusion coefficient for the disturbed zone in D samples was clearly larger than that for the B samples.

The ratio between the permeabilities of disturbed and undisturbed rock was in the range 10 to 90 the average value being 56. The corresponding ratio of effective diffusion coefficients was in the range 5 to 31 with the average value being 18. A regression function of exponential type was found to give a good correlation between the measurements of permeability and effective diffusion coefficient.

Using the He-gas method the depth of the disturbed zone was determined to be 19 mm. Using the ^{14}C-PMMA method the depth of the zone of clearly-increased porosity adjacent to the walls was found to be 10 mm. The average porosity of the disturbed zone in the samples taken from the walls was 2.25 times higher than the porosity of undisturbed rock. The maximum depth of the disturbed zone in the vertical walls of the full scale holes was found to be 25-31 mm.

The structure of the disturbed zone was found to be different in the floor, wall and corner sections. The disturbed zone in the walls, the focus of this study, can be divided into the following sub-zones.

1.   A crushed zone of thickness from 1 to 3 mm. In general, all the mineral grains in this zone are fractured.

2.   A fractured zone extending beyond the crushed zone to a depth of 6-10 mm from the surface. The transformation from zone to zone is gradual and the depth quoted is a very rough estimate. In this zone there is no intragranular fracturing parallel to the surface of the hole. Quartz grains are undamaged. Intragranular fracturing is primarily in mafic

minerals. Fractures form a honeycomb-type network of intersecting planes.

3. A fissured zone extending beyond the fractured zone to depths of 12-31 mm from the wall surface. This zone contains fractures which follow clusters of mafic minerals in the form of inter- and intragranular fracturing. Fractures begin at the surface, penetrate as fracture planes into the rock following the schistocity plane of the rock and then merge gradually into the existing intra- and intergranular fracturing. It is not possible to determine a precise point where the fracturing ends.

Disturbance caused by the boring of the full-scale deposition holes is influenced by tool, machine and rock factors. Since the rock type was practically the same in the large holes and the boring machine was one and the same, the factors which varied during the boring process were the geometry and number of the hard metal buttons and the operating thrust.

Disturbance to the rock was clearly larger at higher levels of thrust. The results also suggest that the disturbance caused by use of the 4- and 5-row cutters used when boring large hole 3 was more pronounced than the disturbance caused by the 5- and 6-row cutters used used when boring large hole 2.

The differences between the alternative cutter arrangements and thrust forces was also seen in the measured values for permeability and effective diffusion coefficient. The disturbance caused by using lower levels of thrust and 5- and 6-row cutters (smaller hard metal buttons) was less than the disturbance caused by using 4- and 5-row cutters (larger hard metal buttons) at higher levels of thrust.

The results of this study show that the extent of the disturbed zone can be modified by redesign of the cutter head. The outermost button rows in the cutter head are the ones that affect the disturbed zone and the higher the thrust per button in the outermost button row, or the higher the penetration rate of the cutter head, the greater the consequent disturbance. The same considerations apply to the geometry and positioning of the hard metal buttons. The degree of disturbance is greater with larger diameter buttons and smaller numbers of buttons.

On the basis of the results obtained in this study, the following suggestions for future development work are given in addition to the work developing the investigation technique discussed in Section 7.5. The results obtained imply that there is a distinct zone of higher porosity and conductivity close to the surface of the hole and parallel to this surface. It is recommended that the effective diffusion coefficient and permeability of this zone be measured in a direction parallel to the surface using the He-gas method. The properties of the zone are directional and it is recommended that two orientations are employed: one perpendicular to the schistosity and one parallel to it.

Since the data for the disturbed zone was obtained using two different thrust forces it is suggested that the degree of disturbance be examined together with the other thrust values employed in order to improve the statistical accuracy of the properties determined, as well as to obtain more data about the values used.

The effect of the gauge rollers is suggested as a matter for study in selected sections of the large holes where the rollers have been in contact with the surface of the hole and where other reference information which is not affected by the rollers exists.

It is recommended that the porosity of samples extracted from the disturbed surface should be determined with different methods for reference.

Since the data obtained relates to gneissic tonalite it is recommended that disturbance in pegmatite and homogeneous tonalite should also be a subject for study since these represent unmetamorphosed igneous rocks.

The orientation of the schistocity planes in the rock was not found to have an effect on the degree of disturbance caused but because of the limited number of samples it is recommended that additional samples be examined.

The data from photographs, autoradiograms, fluorescent microscopy and scanning electron microscopy should be combined and handled in an image analysis system in order to study the distribution of fractures and porous zones in different minerals. Image analysis coud also be used to study the changes in the texture and morphology of the disturbed zone. Such analyses could also be used both to determine the possible disturbance caused by sample preparation and, more importantly, to determine the extent to which the disturbance extends into the rock.

REFERENCES

Autio, J., Äikäs, T. & Kirkkomäki T. 1995. Coring and description of samples from the full scale experimental deposition holes at TVO/Research Tunnel. Helsinki. Teollisuuden Voima Oy. Work Report TEKA-95-02 and similar report AR D-95-003 in SKB's (Svensk Kärnbränslehantering AB) report series.

Autio, J. & Kirkkomäki, T. 1996a. Boring of full scale deposition holes using a novel dry blind boring method. Report POSIVA-96-07, Posiva Oy, Helsinki and similar report in SKB's (Svensk Kärnbränslehantering AB) report series.

Autio, J. & Kirkkomäki, T. 1996b. Boring of full scale deposition holes using a novel dry blind boring method. Boring procedure and operational experiences Work report TEKA-96-04e, Posiva Oy, Helsinki and similar report PR D-96-030 in SKB's (Svensk Kärnbränslehantering AB) report series.

CERCHAR 1986. The Cerchar Abrasiveness Index. Report 86-538. Charbonnages de France.

Daniels, F. & Alberty, R.A. 1967. Physical Chemistry, Third Edition, John Wiley & Sons, Inc. New York.

Darot, M., Gueguen, Y. & Baratin, M-L. 1992. Permeability of thermally crackes granite. Geophysical Research Letters, Vol. 19, NO. 9, may 4, 1992.

Domenico, P.A. and Schwartz, F.W. 1990. Physical and Chemical Hydrogeology, John Wiley & Sons, New York, 824 pp.

Halttunen, K. 1995. Linear surface profile measurements with laser profilometer of experimental full scale deposition holes in TVO Research Tunnel. Work Report TEKA-95-09, Teollisuuden Voima Oy (TVO), Helsinki.

Hartikainen, J., Timonen, J., Väätäinen, H., Pietarila, H. & Hautojärvi, A. 1994. Studies of matrix diffusion in gas phase. Report YJT-94-07, Voimayhtiöiden ydinjätetoimikunta, Helsinki. (in Finnish).

Hartikainen, J., Hartikainen, K., Pietarila, H. & Timonen, J. 1995. Permeability and diffusitivity measurments with the He-gas method of excavation disturbed zone in rock samples cored from the full-scale experimental deposition holes in the TVO Research Tunnel. Report YJT-95-16, Nuclear Waste Commission of Finnish Power Companies, Helsinki.

Hautojärvi, A., Ingman, M. & Öhberg, A. 1993. Hydraulic characterization of the near-field of the boreholes in TVO's research tunnel. Work Report TEKA-93-10, Teollisuuden Voima Oy (TVO), Helsinki.

Hautojärvi, A. 1994. Evaluation of the tracer test in Olkiluoto research tunnel. Work Report TEKA-94-09, Teollisuuden Voima Oy (TVO), Helsinki.

Hautojärvi, A., Vieno, T., Autio, J., Johansson, E., Öhberg, A. & Salo, J.-P. 1994. Characterization and tracer tests in the full-scale deposition holes in the TVO Research Tunnel. Geoval'94, Paris, 11-14 October 1994.

Hautojärvi, A., Ilvonen, M., Vieno, T. & Viitanen, P. 1995. Hydraulic and Tracer Experiments in the TVO Research Tunnel 1993-1994. Report YJT-95-04, Nuclear Waste Commission of Finnish Power Companies, Helsinki.

Hellmuth, K.H., Siitari-Kauppi, M. & Lindberg, A. 1993. Study of Porosity and Migration Pathways in Crystalline Rock by Impregnation with ^{14}C-polymethylmethacrylate. Journal of Contaminant Hydrology, 13.

Hellmuth, K.H., Lukkarinen, S. & Siitari-Kauppi, M. 1994. Rock Matrix Studies with Carbon-14-Polymethylmethacrylate (PMMA); Method Development and Applications. Isotopenpraxis Environ. Health Stud., 30.

Johansson, E. & Autio, J. 1993. Rock Mechanical Properties of Intact Rock in TVO's Research Tunnel. Helsinki. Teollisuuden Voima Oy. Work Report TEKA-93-05.

Johansson, E. 1994. Rock Mechanical Properties of Intact Rock in TVO's Test Boring Site in Boliden, Sweden. Helsinki. Teollisuuden Voima Oy. Work Report TEKA-94-15.

Johansson, E. & Autio, J. 1995. Properties of rock in TVO research tunnel and investigation sites. Work Report TEKA-95-10, Teollisuuden Voima Oy (TVO), Helsinki.

Kukkonen, I. & Lindberg, A. 1995. Thermal conductivity of rocks at the TVO investigation sites. Report YJT-95-08. Nuclear Waste Commission of Finnish Power Companies, Helsinki.

Kuula, H. & Johansson, E. 1991. Rock mechanical stability of the VLJ-repository. Helsinki, Nuclear Waste Commission of Finnish Power Companies, Report YJT-91-03. (In Finnish).

Landolt & Börnstein. 1982. Numerical Data and Functional Relationships in Science and Technology, Vol. V/1a, Physical properties of rock, Springer Verlag 1982.

Salminen, P. & Viitala, R. 1985. Rock Drillability Study. Technical Report 1985/1. Helsinki University of Technology, Laboratory of Mining Engineering, Espoo.

Siitari-Kauppi, M. 1995. Investigation of porosity and microfracturing in a disturbed zone with ^{14}C-PMMA method based on samples from full-scale experimental deposition holes of the TVO Research Tunnel. Report YJT-95-13. Nuclear Waste Commission of Finnish Power Companies, Helsinki.

Siitari-Kauppi, M., Lukkarinen, S. & Lindberg, A. 1995. Study of Rock Porosity by Impregnation with Carbon-14-Methylmethacrylate. Report YJT-95-09, Nuclear Waste Commission of Finnish Power Companies, Helsinki.

Skinner, B. J. 1966. Thermal expansion. In: Handbook of Physical Constants (edited by Clark S. P.), Mem. geol. Soc. Am. 97.

Teollisuuden Voima Oy. 1992. Final disposal of spent nuclear fuel in the Finnish bedrock. Helsinki, Nuclear Waste Commission of Finnish Power Companies, Report YJT-92-31E.

Zalesski, B. V. 1964. Physical and mechanical properties of Rocks. Academy of Sciences of the USSR, Institute of geology and Ore Deposits, Petrography, Mineralogy and Geochemistry. Moskau. Translated from Russian by Israel program for Scientific Translations, IPTS Cat. No. 1858.

Äikäs, K. & Sacklén, N. 1993. Fracture mapping in the Research Tunnel. Work Report 93-01, Teollisuuden Voima Oy, TVO/Research Tunnel, Helsinki.

Äikäs, K. 1995. Measurement of the geometry of the full-scale deposition holes in the TVO Research Tunnel. Work Report TEKA-95-07, Teollisuuden Voima Oy (TVO), Helsinki. (in Finnish).

Äikäs, K. & Sacklén, N. 1995. Fracture mapping of experimental full-scale deposition holes in the TVO Research Tunnel. Work Report TEKA-95-05, Teollisuuden Voima Oy (TVO), Helsinki.

List of SKB reports

Annual Reports

1977-78
TR 121
KBS Technical Reports 1 – 120
Summaries
Stockholm, May 1979

1979
TR 79-28
The KBS Annual Report 1979
KBS Technical Reports 79-01 – 79-27
Summaries
Stockholm, March 1980

1980
TR 80-26
The KBS Annual Report 1980
KBS Technical Reports 80-01 – 80-25
Summaries
Stockholm, March 1981

1981
TR 81-17
The KBS Annual Report 1981
KBS Technical Reports 81-01 – 81-16
Summaries
Stockholm, April 1982

1982
TR 82-28
The KBS Annual Report 1982
KBS Technical Reports 82-01 – 82-27
Summaries
Stockholm, July 1983

1983
TR 83-77
The KBS Annual Report 1983
KBS Technical Reports 83-01 – 83-76
Summaries
Stockholm, June 1984

1984
TR 85-01
Annual Research and Development Report 1984
Including Summaries of Technical Reports Issued
during 1984. (Technical Reports 84-01 – 84-19)
Stockholm, June 1985

1985
TR 85-20
Annual Research and Development Report 1985
Including Summaries of Technical Reports Issued
during 1985. (Technical Reports 85-01 – 85-19)
Stockholm, May 1986

1986
TR 86-31
SKB Annual Report 1986
Including Summaries of Technical Reports Issued
during 1986
Stockholm, May 1987

1987
TR 87-33
SKB Annual Report 1987
Including Summaries of Technical Reports Issued
during 1987
Stockholm, May 1988

1988
TR 88-32
SKB Annual Report 1988
Including Summaries of Technical Reports Issued
during 1988
Stockholm, May 1989

1989
TR 89-40
SKB Annual Report 1989
Including Summaries of Technical Reports Issued
during 1989
Stockholm, May 1990

1990
TR 90-46
SKB Annual Report 1990
Including Summaries of Technical Reports Issued
during 1990
Stockholm, May 1991

1991
TR 91-64
SKB Annual Report 1991
Including Summaries of Technical Reports Issued
during 1991
Stockholm, April 1992

1992
TR 92-46
SKB Annual Report 1992
Including Summaries of Technical Reports Issued
during 1992
Stockholm, May 1993

1993
TR 93-34
SKB Annual Report 1993
Including Summaries of Technical Reports Issued
during 1993
Stockholm, May 1994

1994

TR 94-33
SKB Annual Report 1994
Including Summaries of Technical Reports Issued
during 1994
Stockholm, May 1995

1995

TR 95-37
SKB Annual Report 1995
Including Summaries of Technical Reports Issued
during 1995
Stockholm, May 1996

1996

TR 96-25
SKB Annual Report 1996
Including Summaries of Technical Reports Issued
during 1996
Stockholm, May 1997

List of SKB Technical Reports 1997

TR 97-01
**Retention mechanisms and the flow
wetted surface – implications for safety
analysis**
Mark Elert
Kemakta Konsult AB
February 1997

TR 97-02
**Äspö HRL – Geoscientific evaluation
1997/1. Overview of site characterization
1986–1995**
Roy Stanfors[1], Mikael Erlström[2],
Ingemar Markström[3]
[1] RS Consulting, Lund
[2] SGU, Lund
[3] Sydkraft Konsult, Malmö
March 1997

TR 97-03
**Äspö HRL – Geoscientific evaluation
1997/2. Results from pre-investigations
and detailed site characterization.
Summary report**
Ingvar Rhén (ed.)[1], Göran Bäckblom (ed.)[2],
Gunnar Gustafson[3], Roy Stanfors[4], Peter Wikberg[2]
[1] VBB Viak, Göteborg
[2] SKB, Stockholm
[3] VBB Viak/CTH, Göteborg
[4] RS Consulting, Lund
May 1997

TR 97-04
**Äspö HRL – Geoscientific evaluation
1997/3. Results from pre-investigations
and detailed site characterization.
Comparison of predictions and
observations. Geology and
mechanical stability**
Roy Stanfors[1], Pär Olsson[2], Håkan Stille[3]
[1] RS Consulting, Lund
[2] Skanska, Stockholm
[3] KTH, Stockholm
May 1997

TR 97-05
**Äspö HRL – Geoscientific evaluation
1997/4. Results from pre-investigations
and detailed site characterization.
Comparison of predictions and observa-
tions. Hydrogeology, groundwater
chemistry and transport of solutes**
Ingvar Rhén[1], Gunnar Gustafson[2], Peter Wikberg[3]
[1] VBB Viak, Göteborg
[2] VBB Viak/CTH, Göteborg
[3] SKB, Stockholm
June 1997

TR 97-06
**Äspö HRL – Geoscientific evaluation
1997/5. Models based on site character-
ization 1986–1995**
Ingvar Rhén (ed.)[1], Gunnar Gustafson[2],
Roy Stanfors[3], Peter Wikberg[4]
[1] VBB Viak, Göteborg
[2] VBB Viak/CTH, Göteborg
[3] RS Consulting, Lund
[4] SKB, Stockholm
October 1997

TR 97-07
**A methodology to estimate earthquake
effects on fractures intersecting canister
holes**
Paul La Pointe, Peter Wallmann, Andrew Thomas,
Sven Follin
Golder Associates Inc.
March 1997

TR 97-08
**Äspö Hard Rock Laboratory
Annual Report 1996**
SKB
April 1997

TR 97-09
**A regional analysis of groundwater flow
and salinity distribution in the Äspö area**
Urban Svensson
Computer-aided Fluid Engineering AB
May 1997

TR 97-10
On the flow of groundwater in closed tunnels. Generic hydrogeological modelling of nuclear waste repository, SFL 3–5
Johan G Holmén
Uppsala University/Golder Associates AB
June 1997

TR 97-11
Analysis of radioactive corrosion test specimens by means of ICP-MS. Comparison with earlier methods
R S Forsyth
Forsyth Consulting
July 1997

TR 97-12
Diffusion and sorption properties of radionuclides in compacted bentonite
Ji-Wei Yu, Ivars Neretnieks
Dept. of Chemical Engineering and Technology, Chemical Engineering, Royal Institute of Technology, Stockholm, Sweden
July 1997

TR 97-13
Spent nuclear fuel – how dangerous is it? A report from the project "Description of risk"
Allan Hedin
Swedish Nuclear Fuel and Waste Management Co,
Stockholm, Sweden
March 1997

TR 97-14
Water exchange estimates derived from forcing for the hydraulically coupled basins surrounding Äspö island and adjacent coastal water
Anders Engqvist
A & I Engqvist Konsult HB, Vaxholm, Sweden
August 1997

TR 97-15
Dissolution studies of synthetic soddyite and uranophane
Ignasi Casas[1], Isabel Pérez[1], Elena Torrero[1], Jordi Bruno[2], Esther Cera[2], Lara Duro[2]
[1] Dept. of Chemical Engineering, UPC
[2] QuantiSci SL
September 1997

TR 97-16
Groundwater flow through a natural fracture. Flow experiments and numerical modelling
Erik Larsson
Dept. of Geology, Chalmers University of Technology, Göteborg, Sweden
September 1997

TR 97-17
A site scale analysis of groundwater flow and salinity distribution in the Äspö area
Urban Svensson
Computer-aided Fluid Engineering AB
October 1997

TR 97-18
Release of segregated nuclides from spent fuel
L H Johnson, J C Tait
AECL, Whiteshell Laboratories, Pinawa, Manitoba, Canada
October 1997

TR 97-19
Assessment of a spent fuel disposal canister. Assessment studies for a copper canister with cast steel inner component
Alex E Bond, Andrew R Hoch, Gareth D Jones, Aleks J Tomczyk, Richard M Wiggin, William J Worraker
AEA Technology, Harwell, UK
May 1997

TR 97-20
Diffusion data in granite Recommended values
Yvonne Ohlsson, Ivars Neretnieks
Department of Chemical Engineering and Technology, Chemical Engineering, Royal Institute of Technology, Stockholm, Sweden
October 1997

TR 97-21
Investigation of the large scale regional hydrogeological situation at Ceberg
Anders Boghammar[1], Bertil Grundfelt[1], Lee Hartley[2]
[1] Kemakta Konsult AB, Sweden
[2] AEA Technology, UK
November 1997

TR 97-22
**Investigations of subterranean
microorganisms and their importance
for performance assessment of
radioactive waste disposal. Results
and conclusions achieved during the
period 1995 to 1997**
Karsten Pedersen
Göteborg University, Institute of Cell and
Molecular Biology, Dept. of General and Marine
Microbiology, Göteborg, Sweden
November 1997

TR 97-23
**Summary of hydrogeologic
conditions at Aberg, Beberg
and Ceberg**
Douglas Walker[1], Ingvar Rhén[2], Ioana Gurban[1]
[1] INTERA KB
[2] VBB Viak
October 1997